Analysis of Fatigue Damage in Unidirectional Carbon Fibre Reinforced Polymer Material

Zur Erlangung des akademischen Grades eines
Doktors der Ingenieurwissenschaften (Dr.-Ing.)

von der KIT-Fakultät für Maschinenbau des
Karlsruher Instituts für Technologie (KIT)

angenommene
DISSERTATION
von

M.Eng. Zalikha Murni Abdul Hamid

Tag der mündlichen Prüfung:	25.03.2022
Hauptreferent:	Prof. Dr. rer. nat. Peter Gumbsch
Korreferenten:	PD Dr.-Ing. habil. Jörg Hohe
	Prof. Dr.-Ing. Kay André Weidenmann

To Mama, Papa and my husband, the love of my life

Acknowledgements

The research presented in this thesis was conducted at Fraunhofer Institute for Mechanics of Materials IWM, Freiburg with the support from the Institute for Applied Materials - Computational Materials Science at the Karlsruhe Institute of Technology (KIT).

First and foremost, I would like to express my sincere gratitude to both of my advisors Prof. Dr. rer. nat. Peter Gumbsch and PD Dr.-Ing. habil. Jörg Hohe for their invaluable advice, continuous support, patience and dedication during my PhD study. Their immense knowledge and plentiful experience have encouraged me in every step throughout the process of this research and writing of this thesis. I could not have imagined having a better advisors and mentors for my PhD study.

Besides both of my advisors, I would like to thank the rest of my thesis committee: Prof. Dr.-Ing. Kay André Weidenmann and Prof. Dr.-Ing. Alexander Fidlin, for their insightful comments and encouragement, but also for all of the questions which inspire me to widen my research from various perspectives. My gratitude extends to Hector Fellow Academy (HFA) for the funding opportunity during my PhD, making this a possibility.

I would like to take this opportunity to acknowledge the project 'RTM CAE/CAx – Aufbau einer durchgängigen CAE/CAx-Kette' for providing the raw material for the microspecimens. Project HyMod is greatly acknowledged for all of the macrospecimen experimental and numerical results that serve as the reference to this research. The new idea of fatigue damage model presented in this thesis was also inspired by the project titled 'Ermüdung kurzfaserverstärkter thermoplastischer Polymerwerkstoffe'.

Getting through my PhD required more than academic support, and I have many, many people to thank for listening to and, at times, having to tolerate me over the years. For this, I would like to thank my friends, lab mates, colleagues and research team - Lucas Paul Mayer, Claudio Findeisen, Michael Schober, Benedikt Rohrmüller, Michael Deissenbeck, Gerhard Stöhr, Karin Hintz and Uwe Strohmeier for all of the hours working together in the institute, stimulating discussions and countless feedback sessions to help me throughout my time there. It is their kind help, support and friendship that have made my research and life in Germany a wonderful time.

Most importantly, none of this could have happened without my family (both, in Malaysia and Poland). Their unconditional love and belief in me has kept my spirits and motivation high, remind me of what is important in life, and are always supportive of my adventures. To my husband, Bartosz Błasiak - it would be an understatement to say that we have experienced some ups and downs in the past years. Every time I was ready to quit, you did not let me and I am forever grateful. Thank you from the bottom of my heart.

Freiburg im Breisgau, 2022
Zalikha Murni Abdul Hamid

Abstract

Carbon fibre reinforced polymer (CFRP) is widely used across different industries, mainly aviation, marine, automotive, sports equipment, and many more. This is attributed to its outstanding high strength-to-weight ratio compared to other materials such as metals. In addition, this material also features design customizability to fit various applications, which makes it one of the most versatile materials today. In real-life applications, CFRP structures are subjected to fatigue loading. The material response towards this loading is very complex. This is due to the evolution of damage within the material that occur through various failure mechanisms. The intricacy of fatigue damage in CFRP material is also contributed by the individual failure mechanisms and the synergy effects by these failure modes that occur concurrently at the microscopic level. Due to this complexity, macroscopic and microscopic material level response knowledge is required to comprehensively understand fatigue damage in CFRP. However, this crucial knowledge is not easily obtainable from standard testing alone.

This thesis discusses the analysis of damage methods for unidirectional (UD) CFRP under fatigue loading through experimental and modelling work. A new experimental method to study fatigue on micro-level material response was introduced. The fatigue test requires a unique sample preparation process that involves micro-specimens of different fibre orientations (0°, 30°, 45°, 60° and 90°). The test was done under room temperature and $R = 0.1$ stress ratio. The results obtained from the test are presented as an S-N curve, and in-situ observations of the micro-specimens are analysed. The fracture surface of selected broken micro-specimens is also presented and discussed here. Based on the comparison with standard macro-specimens testing, it can be deduced that the micro-fatigue test is of comparable quality to the macro-specimens standard testing. It also offers additional advantages in supplying a direct possibility to observe several critical phenomena under loading.

A new continuum damage mechanics model (CDM) for fatigue and degradation of CFRP has also been proposed. The model is formulated based on anisotropic linear elastic Hooke's law brittle model. The model includes three damage variables, each representing

damage effect oriented with respect to the three coordinate axes. The formulation concept based on the dissipation of microplastic work within the material gives a physical sense of how the damage evolves in CFRP under fatigue. It is found to be numerically efficient due to the possible estimation of microplastic work from the elastic components of stress and strain. The model has been implemented in Abaqus user-subroutine and validated against two different types of fatigue specimens (macro-specimens and micro-specimens). In the case of macro-specimens, the model has been validated against filament wound carbon fibre epoxy matrix for the case of UD and multidirectional (MD) composite under tension, compression and alternating cyclic loading [1–3]. On micro-specimens, a UD composite was analysed under tension fatigue load. The model proves a good prediction which indicates the model capability to accurately predict the fatigue lifetime of CFRP material at both macro and micro-level response. The thesis also discusses a new formulation to improve the current fatigue damage model further. The combination of experimental and modelling methods presented here provides high potential tools in the analysis of fatigue damage on CFRP material.

Kurzfassung

Carbonfaserverstärkte Kunststoffe (CFK) zeichnen sich in erster Linie durch ihre geringe Dichte bei gleichzeitig hoher massenspezifischer Festigkeit aus. Hinzu kommt, dass sich die Eigenschaften von CFK durch Materialaufbau und Zusammensetzung in weiten Bereichen an die verschiedensten Anwendungen anpassen lässt, wodurch CFK in vielen Industriezweigen wie Luft- und Seefahrt sowie der Automobil- und Sportbranche zum Einsatz kommen. Für die zuverlässige praktische Anwendung von CFK ist unter anderem ein tiefgreifendes Verständnis der Ermüdungsschädigung und des Ermüdungsversagens notwendig. Das Ermüdungsverhalten von CFK ist geprägt von verschiedenen Schädigungsmechanismen die auf unterschiedlichen Größenskalen ablaufen. Dies, sowie die Interaktion der der einzelnen Schädigungsmechanismen untereinander, macht die Ermüdungsanalyse sowie Modellierung zu einer herausfordernden Aufgabe, die mit den derzeit etablierten Prüfmethoden alleine nicht hinreichend zu bewerkstelligen ist.

Um zum Verständnis der, der Ermüdungsschädigung zugrundeliegenden, Mechanismen beizutragen, wird in dieser Arbeit ein neuer experimenteller Ansatz zur Ermüdungscharakterisierung von unidirektional verstärkten Werkstoffen (UD CFK) vorgeschlagen und untersucht. Zum Einsatz kommen hierbei speziell gefertigte Mikroproben (Länge 3mm, Breite 2.5mm und Dicke 100µm) mit unterschiedlichen Faserorientierungen von (0°, 30°, 45°, 60°, und 90°). Die Last wird, bei Raumtemperatur, als Zugschwellbelastung mit einem Spannungsverhältnis von $R = 0.1$ aufgebracht. Neben der Erstellung der üblichen Wöhlerkurven, erfolgt eine tiefgreifende Analyse der Schädigungs- und Bruchmechanismen durch in-situ Aufnahmen sowie einer weitreichenden Bruchflächenanlyse der gebrochenen Proben. Ein Vergleich mit etablierten, an Makroproben durchgeführten, Ermüdungsversuchen, zeigt, dass die hier vorgeschlagene Mikroprüftechnik zu vergleichbaren Ergebnissen führt, darüber hinaus aber weitreichende Möglichkeiten zur Analyse des Versagensverhalten ermöglicht.

Ergänzend zu den experimentellen Arbeiten wird ein Kontinuums-Schädigungsmodell zur Modellierung des Ermüdungsverhalten von CFK entwickelt und validiert. Das Modell basiert auf dem anisotropen linearen Elastizitätsgesetz in dem die Steifigkeitsdegradation

durch Mikroschädigung über drei Schädigungsvariablen abgebildet wird. Die Schädigungsevolution selbst wird, unter Berücksichtigung der mikroplastischen Energiedissipation, hergeleitet, wodurch das Modell eine solide physikalische Basis erhält. Die mikroplastische Dissipation hingegen kann aus den elastischen Komponenten der Dehnung und Spannung abgeschätzt werden, wodurch eine numerisch effiziente Implementierung möglich ist. Die Implementierung erfolgte im Rahmen dieser Arbeit als Userroutine in dem kommerziellen Finite-Elemente Programm Abaqus. Für eine weitreichende Validierung wurde das Modell mit unidirektionalen und mehrdirektionalen makroskopischen Ermüdungsversuchen unter Zug-, Druck- und Wechselbelastung, sowie mit mikroskopischen Zugversuchen an unidirektionalen Werkstoffen verglichen. Hierdurch konnte die gute Vorhersagequalität der Lebensdauer, sowohl für Makro-, als auch für Makroproben, nachgewiesen werden. Schlussendlich werden mögliche Modellerweiterungen vorgeschlagen und diskutiert, die, unter Verwendung der gewonnen experimentellen Daten, eine weitere Verbesserung der Vorhersagequalität ermöglichen.

Publications and Presentations

Publications

- J. Hohe, M. Gall, S. Fliegener, and Z.M. Abdul Hamid. A continuum damage mechanics model for fatigue and degradation of fiber reinforced materials. Journal of Composite Materials, 54:2837–2852, 2020.

- Z.M. Abdul Hamid, M. Florea, S. Fliegener, M. Schober, J. Hohe, and J. Rühe. Chemical modification of fiber-matrix interfaces of glass fiber reinforced thermoplastics and methods for interface characterization. Advanced Engineering Materials, 21:1800590, 2019.

- J. Hohe, M. Gall, H. Gauch, S. Fliegener, and Z.M. Abdul Hamid. A material model for prediction of fatigue damage and degradation of CFRP materials. In 21st Symposium on Composites, Bremen, Germany, Key Engineering Materials, pages 740–744. Trans Tech Publications Ltd., Stafa-Zurich, Switzerland, 2017.

- Z.M. Abdul Hamid, J. Hohe, M. Gall, S. Fliegener, and P. Gumbsch. Fatigue damage and degradation model for carbon fibre reinforced polymer materials. PAMM, 17:259–260, 2017.

Presentations

- Z.M. Abdul Hamid and J. Hohe. Micromechanical experimental characterization of fatigue in unidirectional CFRP materials. In CU-Arbeitsgruppensitzung AG Strukturelle Integrität und UAG Composite Fatigue, Online, 2020.

- Z.M. Abdul Hamid, M. Gall, S. Fliegener, and J. Hohe. Fatigue Damage and Degradation Model for Carbon Fibre Reinforced Polymer Materials. In 7th International Conference on Fatigue of Composites, Vicenza, Italy, 2018.

- Z.M. Abdul Hamid, M. Gall and J. Hohe. A Continuum Damage Mechanics Model for Fatigue Assessment of FRP Materials. In Automative CAE Grand Challenge, Hanau, Germany, 2018.
- Z.M. Abdul Hamid, J. Hohe, M. Gall, S. Fliegener, and P. Gumbsch. Fatigue Damage and Degradation Model for Carbon Fibre Reinforced Polymer Materials. In 88th Annual Meeting of GAMM, Weimar, Germany, 2017.
- Z.M. Abdul Hamid, L.P. Mayer, M. Schober, J. Hohe, S. Fliegener, M. Florea, J. Rühe. Chemical Modification of Fiber-Matrix Interfaces for Enhancing the Strength and Durability of Materials, Part II: Mechanical Characterization. In European Congress and Exhibition on Advanced Materials and Process - EUROMAT, Thessaloniki, Greece, 2017.
- M. Schober, Z.M. Abdul Hamid, J. Hohe, S. Fliegener, and T. Kennerknecht. Numerical-Experimental Characterization of Fiber Matrix Interfaces in Fiber Reinforced Plastics. In CCeV Seminar on Fibers and Matrices, Carbon Composites e.V., Augsburg, Germany, 2017.

Contents

Chapter 1

Introduction

1.1 Motivation

Carbon fibre reinforced polymer (CFRP) materials are used widely in advanced structural applications. The material has been gaining popularity across several industries mainly aviation, marine, automotive, sports equipment and many more. Articles published by Airbus and Reinforced Plastic magazine in their November/December 2010 issues [4] reported that as much as 52% of the Airbus model of A350XWB aircraft is built of CFRP materials (see Figure 1.1), demonstrating the relevance of this material for further aircraft development. The high stiffness carbon fibres paired with thermoset/thermoplastic resin offer many advantages over traditional material. The advantage includes their outstanding high strength-to-weight ratio compared to other materials such as metals. Besides that, CFRP features design customizability to fit various applications suggesting the material to be one of the most versatile choices in the industries. The loading during operating conditions often involves fatigue loading.

Although the material is subjected to loading below its elastic yield limit over a period of time, the material response towards this loading is very complex. Under fatigue loading, CFRP develops a damage zone comprising stress concentrations regions, including

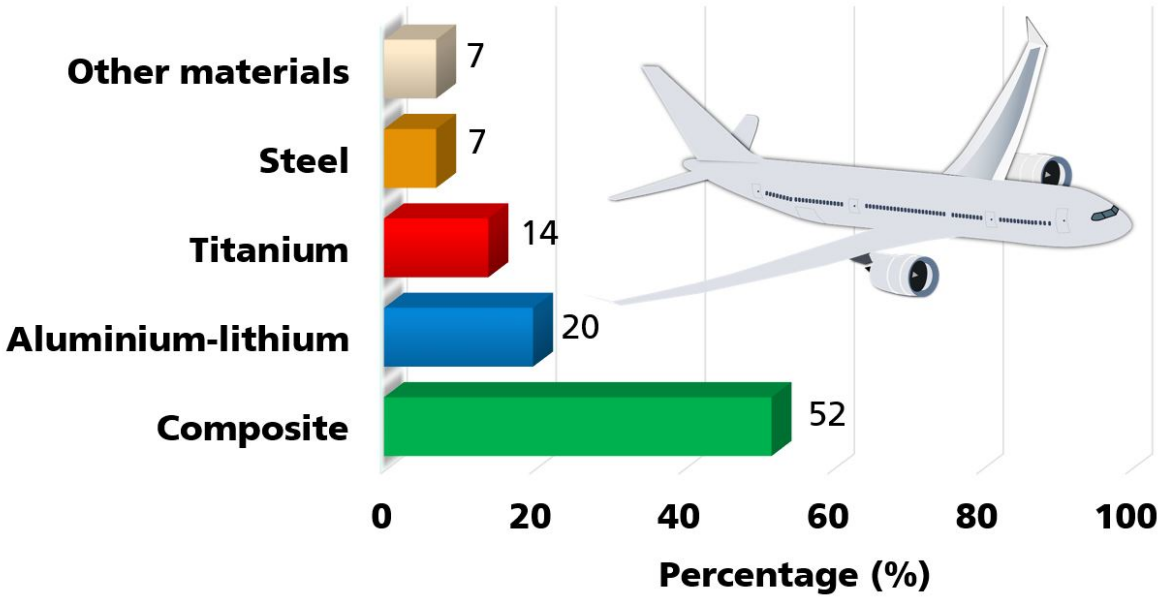

Figure 1.1: Composition of material used in Airbus A350XWB as taken from Ref. [4].

gradual energy dissipation, resulting in progressive damage throughout its fatigue lifetime. The evolution of damage within the material is manifested through various failure mechanisms such as matrix cracking, fibre/matrix interface debonding, fibre fracture, fibre pull-out, and interface delamination. The intricacy of fatigue damage in CFRP material is also contributed by the individual failure mechanisms and the synergy effects by these failure modes that occur concurrently at the microscopic level. Due to this reason, reliability assessment of this material highly depends on the continual process from the initiation of damage through its propagation up until total material failure. Hence, it is crucial to consider all of the complexity revolving around damage evolution failure mechanisms along with material load history from the macroscopic and the microscopic perspective of the material.

1.2 Scope

This thesis aims to discuss an analysis of fatigue damage on unidirectional (UD) CFRP polymer material from two different aspects, experimental and modelling. To allow this, a thorough understanding of the material composition is presented in Chapter 2. Introduction to CFRP response under fatigue loading, including factors affecting the response, will provide ideas on the general problems concerning the complexity of the material that warrants the need for a systematic analysis of this material. The commonly available standard guidelines for testing CFRP are discussed further to present the importance of new micro-level testing as a supporting technique to the existing standard testing, introduced later in

Chapter 4. The final part of Chapter 2 presents the outlook into the available approach for fatigue damage models and the main criteria required to be addressed for a practical and accurate fatigue damage model.

A new fatigue damage modelling approach that satisfies all of the requirements for a material-level model is presented in Chapter 3. This fatigue damage model applies to all load histories and is derived based on microplastic dissipation energy in CFRP under fatigue loading. The dissipative concept here can be approximated from the elastic deformation, and therefore, it is numerically efficient even for a large system. The proposed model is implemented in Abaqus user-subroutine and validated against filament wound carbon fibre/epoxy matrix composite. In general, this chapter discusses the fatigue modelling aspect of CFRP material with the analysis of the proposed damage models.

The complexity of fatigue fracture behaviour of CFRP requires outcomes from systematic standard testing guidelines. It can be complemented by a micro-level test that enables looking into the fracture response up-close at the same level as the failure mechanisms. Chapter 4 introduces a new micro-fatigue test method that has been used on UD CFRP material with different fibre orientation angles. Such a method has been proven to work on metallic materials. However, micro-fatigue test on composite material has never been done before due to the complexity of CFRP materials. Therefore, a step-by-step micro-specimen preparation involving CFRP material is developed, combining the micro-fatigue experiment. The results via this new method (S-N diagram, in-situ observation and fracture surface analysis) are further discussed to understand fracture behaviour under fatigue better. The fatigue damage model introduced earlier in Chapter 3 has also been applied on micro-fatigue specimens results and discussed further to show the importance of studying the material closer to its material-level response. Additionally, a newly improved fatigue damage model concept is also proposed. Chapter 4 as a whole provides various micro-level insight that bridges the gap between the structure level response and material-level response. An overall summary, including the prospect for future development in the characterisation of fatigue in CFRP material, is then discussed in Chapter 5.

Chapter 2

Fundamentals and Related Work

2.1 Composite Materials

A composite material comprises two or more different constituents with defined interfaces. Those components are typically very different in terms of their properties resulting in highly heterogeneous material [5]. When combined, these individual constituents create a whole new material with different properties than the individual constituents. Fibre reinforced polymer (FRP) is usually made of high-strength fibres held together by the matrix. The primary function of the fibre is to carry the load applied to the material [6]. At the same time, the matrix binds the fibres together while transferring the load uniformly throughout the whole material. The matrix also protects the fibres from exposure to the external environment.

Due to the outstanding high ratio of strength to weight offered, composite materials are gaining popularity over traditional 'homogeneous' materials. The flexibility and versatility of composite materials that can be manufactured in various configurations allow them to be customised to fit the required application needs [7, 8]. The output properties of a composite highly depend on several factors, including the individual constituents' properties and the manufacturing process involved. This study will focus mainly on the carbon fibre

reinforced polymer (CFRP) with epoxy matrix.

Fibre. One of the main components in a CFRP composite material is carbon fibre. CFRP can be constructed into a one, two and three-dimensional manner [8]. One-dimensional fibre construction consists of continuous and discontinuous fibre. Although these types belong to the same construction category, their properties differ. The advantage of working with continuous fibres is the ability to control the fibre orientation, making the composite's overall properties easily manipulated. The ability to control the fibre orientation is critical given that fibre is the main component that supports the load [6] and composite performance rely highly on its fibre orientation [9]. Unlike continuous fibre, the fibre orientation of CFRP made of discontinuous fibres is more difficult to control [8].

The two and three-dimensional construction types of fibres are usually presented in the form of laminated structures [10]. There are two significant advantages of using two and three-dimensional fibre construction. Firstly, the ability to control the overall fibre orientation produces a custom-made material to fit the application. Secondly, this construction can be used in complex structure manufacturing [11]. This capability offered by two and three-dimensional fibre construction makes them superior in terms of application when compared to unidirectional (UD) continuous fibres. An added advantage of the quality of three-dimensional fibre construction is its ability to improve delamination from one ply to another. This is due to the existence of fibre through the thickness direction that enhances the CFRP interlaminar fracture toughness [12]. Aside from CFRP's customizable features as a well-known advantage, another bonus of using carbon fibres is that they can be manufactured from different raw material sources. Alam et al. in their review [13], show that carbon fibres can be further categorised based on their mechanical properties as presented in Figure 2.1.

Matrix. Another main component of CFRP is the matrix medium. There are two types of polymer materials used as the matrix: thermoplastics and thermoset. Both of these polymer groups provide characteristic differences [13]. For example, thermoplastics are known to melt (soften) under elevated temperature and harden when it cools down. This allows the shape of the material to be altered to fit the application requirement. Examples of the common thermoplastics polymer are polyamide 66 (PA66), poly-ether-ether-ketone (PEEK) and Polyethylene terephthalate (PET). Thermoplastic polymer offers high toughness and can be easily manufactured in significant volume at a lower manufacturing and processing cost.

Another polymer matrix group is thermoset polymers that cannot be reshaped after curing. The condition provided by the curing process induces a chemical reaction that

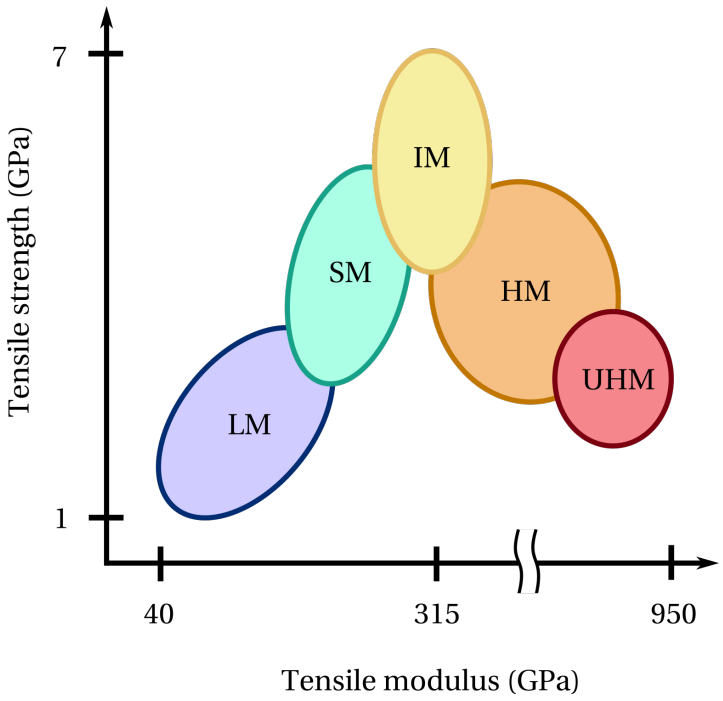

Figure 2.1: Category of carbon fibres based on their mechanical properties (LM: low modulus, SM: standard modulus, IM: intermediate modulus, HM: high modulus and UHM: ultra high modulus) adapted from Alam et al. [13].

causes cross-linking of polymer chains within the material. As an effect, thermosets become mechanically and chemically stable after the curing process, making them insensitive to further heat exposure [14]. The most common example of thermoset polymer is epoxy, silicone, phenolics and polyurethane (PUR and PU). Throughout this study, a focus will be given mainly on CFRP with epoxy matrix composite. Epoxy material, although more expensive when compared to thermoplastics, has better moisture and corrosion resistance. Epoxy also undergoes limited constriction under the curing process and has a much lower fracture toughness than thermoplastics giving epoxy its brittleness characteristics. Epoxy has also been found to be more immune to the effect of fatigue loading compared to thermoplastic [15].

As mentioned earlier, choosing a matrix is crucial in contributing to overall CFRP properties. Depending on the type of loading applied to the composite, the role of a matrix with respect to the loading properties varies [15]. Matrix contribution in UD composite under longitudinal tensile (tensile load in the direction of fibre) loading is insignificant compared to other loading configurations. This is mainly because the fibres carry most of the load applied under longitudinal tensile loading. This is in contrast to the events when either (i) tensile load is applied transverse to the fibre, (ii) compression load acts in transverse or (iii) longitudinal direction, and lastly (iv) shear loading is present [16].

Unidirectional carbon fibre reinforced polymer. In an attempt to thoroughly understand the CFRP material, UD CFRP is chosen for the micro-mechanical level material study presented in the later stage of the thesis. UD composite consists of several plies of fibre that are oriented in the same direction [17]. UD CFRP is said to have orthotropic properties due to the significant variance of strength and stiffness in the fibre and transverse directions.

2.2 Fatigue of CFRP

CFRP material response under fatigue loading is very complex. This is because the material experiences gradual deterioration under such loading, leading to total material failure [5, 8, 13, 18]. Although the applied cyclic load remains below the material elastic limit, the material develops stress concentration regions within which gradual energy dissipation contributes to progressive damage development within the material. Individual microscopic cracks develop as the material is exposed under continuous cyclic load. With time, these regions containing microcracks grow and begin to accumulate in the material. The micro-damages later develop into macro-scale damage and steer the material towards failure [5, 8, 13, 18].

Such microcracks evolve according to several stages. Firstly, the material under fatigue loading experiences the formation of microcracks. Microcrack openings develop with added fatigue cycles, leading to crack nucleation and early sign of material damage in the second stage. As the material is loaded further, the tendency of crack nucleation increases while some of the microcracks begin to propagate. Here, the rate for the crack propagation, including crack nucleation, highly depends on various factors such as the existence of void or defects, inclusion or even the material profile affecting the stress concentrations within the material [5, 13]. The microcracks that propagate and nucleate later merge into a macrocrack. This crack then continues to grow steadily until it reaches its critical size. At the final stage of CFRP fatigue damage, the sudden growth of the macrocracks occurs, resulting in complete material failure.

CFRP material response under fatigue is very different from metallic materials. Unlike composite under fatigue, no substantial deterioration in stiffness can be seen in metallic materials throughout fatigue lifetime. In addition to that, metallic material fails under fatigue loading mainly due to the initiation, growth and coalescence of macroscopic cracks [8]. In contrast to metallic materials, fatigue failure of CFRP materials can be divided into three distinct stages [19] as presented in Figure 2.2. The first stage is due to the formation of microcracks that commence immediately after just a few hundred cycles of loading. The damage at this stage appears as fibre-matrix interface failure or fibre pull-out,

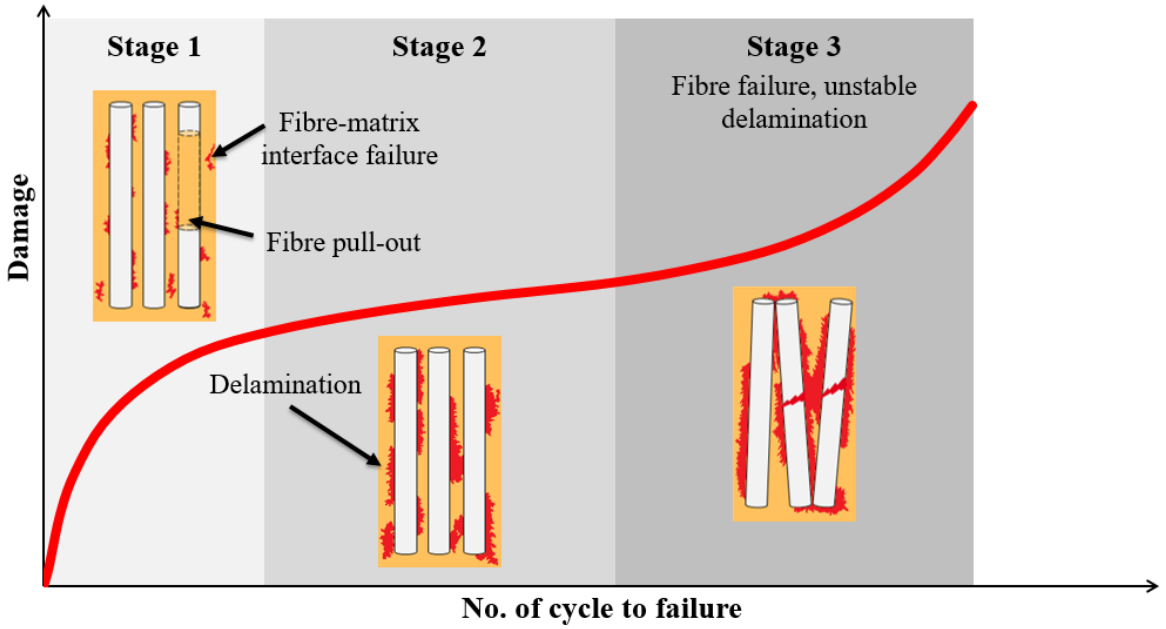

Figure 2.2: Damage evolution stages

.

which translates into rapid degradation within the material at the initial stage of the loading. After the material undergoes rapid degradation in the first stage, the material stiffness remains almost constant with minimal degradation throughout the second stage. The failure mechanism associated with this fatigue failure stage is the interlaminar shear stress or delamination. As the material progresses into the third stage, accelerated stiffness degradation can be seen within the material until the material reaches its final failure. Here, the failure mechanisms associated with the third stage of material degradation manifested as fibre failure and unstable delamination growth [1–3].

The complexity in the fatigue response of CFRP material is primarily due to the material fatigue lifetime that highly depends on the development of individual damage mechanisms and their synergy. Moreover, the heterogeneity of the material composition and several factors such as the material operational environment, mechanical loading, and many more greatly impact CFRP fatigue lifetime [13, 20–22].

Due to the synergistic nature of failure mechanisms in CFRP material, the complexity is magnified when specific failure mechanisms could also exist in mixed-mode conditions. An excellent example of this is delamination. The occurrence of delamination in CFRP is very complex, whereby it usually starts at the beginning of the loading. However, as the material undergoes further loading, delamination in the material progresses in the form of mixed-mode throughout the material fatigue lifetime [23]. Elaborate studies suggesting various methods to characterise CFRP delamination has been done, yet this particular

failure mechanism phenomenon is still a subject of ongoing research among composite researchers today [23-25]. Carbon fibre/epoxy composite has exhibited good resistance towards fatigue loading in numerous studies compared to other composites [13, 16, 26]. Despite that, the fatigue response of carbon fibre/epoxy composite produces the highest scatter when presented in terms of S-N curves. Most studies suggest that the high scatter in the CFRP S-N curves is mainly due to the microcrack development-based failure mechanisms that the material sustains under fatigue loading and the adhesion bonding between the fibre-matrix interface [13, 16].

2.3 Factors Affecting Fatigue Performance

Several factors play an essential role in the fatigue performance of CFRP material. These factors include the choice of fibres and matrix, the fibre/matrix interface, fibre orientations, CFRP manufacturing process, the CFRP laminate stacking sequence, fibre volume fraction and other factors. However, not all of them will be covered here, but only the most critical factors relevant to this study. Information on other factors can be found elsewhere [27, 28].

Fibres. One of the most critical failure mechanisms concerning the choice of fibres in CFRP is fibre fracture. This failure mechanism highly depends on fibre strength and its properties. Due to the primary function of the fibre that is to carry the load applied on the composite structure [6], the higher the fibre strength, the higher the load that the fibre can carry during fatigue loading [3]. The fibre ability to carry a higher load indirectly will result in the lower load required for the matrix to be distributed. Since the fibre is stiffer than the matrix, the fibre will act as a natural constraint to the matrix locally. Consequently, it inhibits straining of the matrix and thus, reduces the matrix plastic deformation.

Also, it is well known that the fibre fracture requires a more significant amount of fracture energy to be initiated compared to the matrix failure. Since the fibres play primary roles in carrying the load, stiff fibres are crucial in decreasing the rate of fatigue crack growth in the matrix. Hence, the fatigue lifetime of the material can be extended [13, 18]. Jones et al. [29] showed that the types of fibre fracture are related to the type of carbon fibre used. In general, carbon fibres can be divided into five categories based on their mechanical properties (see Figure 2.1) [13, 29]. These categories are low, standard, intermediate, high and ultra high modulus carbon fibres. A more specific description for each category of these carbon fibres is presented in Table 2.1.

Previous studies have shown how carbon fibres fail under fatigue loading can be related to the amount of energy dissipated during failure [13, 18, 29]. They found that carbon fibres

Table 2.1: Categories of carbon fibres according to their mechanical properties adapted from Ref. [13, 29].

Category	Tensile Modulus (GPa)	Tensile Strength (GPa)
Low modulus	40 - 200	1.0 - 3.5
Standard modulus	200 - 300	2.5 - 5.0
Intermediate modulus	280 - 350	3.5 - 7.0
High modulus	350 - 600	2.0 - 5.5
Ultra high modulus	600 - 950	2.0 - 4.0

with relatively high tensile modulus can carry more load and thus, store a more significant amount of energy at the same strain. However, when the matrix fails, all of the stored energy accumulated within the fibres are released almost instantaneously, resulting in a sudden, catastrophic and explosive fracture. On the other hand, damage that occurs within a low modulus carbon fibre build up and grow gradually with time. As a result, fibre is more likely to fail due to stress localisations that develop within the material and the steady dissipation of energy. Therefore, low modulus carbon fibres are said to fail progressively. With ultra high modulus and low modulus carbon fibres being the two extreme cases (see the first and last row of Table 2.1), all the other carbon fibres failure behaviour falls between abrupt and progressive failure. The two most crucial failure mechanisms involving fibre properties within CFRP materials are fibre fracture and fibre pull-out [30].

Matrix. The choice of a matrix is another factor that may affect fatigue performance. Fatigue performance has been shown to improve with brittle matrix and high strength and stiffness fibres [31]. High stiffness and strength fibres have a higher capability to carry a more significant load applied to the structure. By doing this, a lesser load is distributed to the matrix. With a minimal load on the matrix, high matrix straining can be avoided resulting in a reduction of matrix plastic deformation and enhancement of fatigue life on the CFRP structure.

Apart from that, matrix failure by fatigue loading can also be affected by the number of fibres in the region where the matrix fails differently depending on the stage of loading. A study by Watanabe et al. [32] describes the difference between matrix failure in two regions showcasing the different amounts of fibres available at the beginning and the end of loading. They found that in a dense fibre region where fibres are closely positioned next to each other, microcracking is initiated between the fibres (the region where fibres are in contact). The crack later propagates into the fibre/matrix interface in the form of a sharp crack without any sign of matrix deformation. It is a brittle failure. However, in the less dense fibre region, microcracking starts to initiate in the fibre/matrix interface instead,

propagates along the interfaces and further expands into the matrix. Significant matrix plastic deformation can be observed, appearing as a blunt crack. Interestingly from their findings [32], the interaction between several failure mechanisms can be noted at the final stage of the loading in these two different regions. In the dense fibre region, microcracks in the fibre/matrix interface start to grow and later coalesce, forming a single crack with lots of other local microcracks initiated in the region with high-stress concentration. On the contrary, macrocrack is formed from several microcracks in different positions, merging for a less dense fibre region. This additionally speeds up the stress singularity locally while initiating new sharp microcracks around the crack tip area. Significant matrix plastic deformation can be observed around the crack tip region with the formation of a void in front of the crack tip. The matrix failure, in this case, is observed to be more ductile than in the fibre-dense region [32].

There are, in general, several failure mechanisms that can be closely associated with the matrix in CFRP material. Matrix failure, fibre pull-out and especially delamination [29, 33–35] are among the most discussed phenomena under fatigue loading. As mentioned before, the complexity of studying fatigue response is significantly due to the unique failure mechanisms that could be the initiating factor for another and the interaction between these failure mechanisms when they exist simultaneously. An example of this could also occur in matrix dominated conditions whereby matrix failure causes the interlaminar stresses between plies to increase. The increase further leads to delamination of the structure [36]. In the case of compressive fatigue, fibre buckling is one of the central failure mechanisms that cause the material to fail. However, with the use of stiffer matrix material, this failure can be suppressed [31]. In addition, matrix failure has been closely linked to the fibre/matrix interface. Most microcracks begin initially at the fibre/matrix interface before moving into the matrix region and causing matrix failure.

Fibre/matrix interface. Fibre/matrix interface plays a vital role in the fatigue lifetime of CFRP material. When the fibres carry most of the load, the matrix is responsible for distributing the load evenly throughout the material to ensure stability under fatigue loading. The stress transfer medium between the fibres and the matrix needs to be at the optimum to achieve such stability. This dramatically relies on the quality of the fibre/matrix interface. A weak fibre/matrix interface hinders the propagation of cracks into the matrix. For this reason, microcracks will continue to propagate along the weak fibre/matrix interface and, therefore, reduce the effectiveness of the stress transfer between fibre and matrix, thereby lowering the fatigue lifetime of the whole structure [37–39]. Furthermore, weak adhesion between the fibre and the matrix instigates debonding or delamination in the CFRP

structure. The capability of the matrix to adhere to fibre is a function of the matrix coating quality on fibres and fibres profile and can be improved through fibre surface treatment [40, 41]. This clearly illustrates the connection between the fibre/matrix interface quality to each component of the constituents that build up the composite structure. Delamination or debonding in CFRP material that originates from the fibre/matrix interfaces has also been found to cause fibre pull-out failure due to the bond shear strength between the fibre and matrix [37]. Delamination in CFRP requires the least energy to be initiated under fatigue loading. Therefore, it is one of the most common failure mechanisms found in the initial state of the loading [42].

Fibre orientations. Apart from the type of fibre used in CFRP material, different orientations of the same fibres significantly affect CFRP composite's fatigue performance [9]. Significant effects introduced by the fibre orientation on fatigue of CFRP can be observed from the S-N curves representation of the results [43]. In the case of longitudinal fibre orientation (0° fibre orientation), the loading is applied parallel to the fibre orientation. In this instance, the stiff fibres can carry most of the loading. Therefore, the material will have to undergo higher tensile fatigue strength to reach fibre fracture failure mode for the fibre to break, resulting in a higher tensile fatigue strength with a high intercept value of the S-N curves. However, when the fibre orientation varies at a higher angle, another distinct failure mode variation applies. As the angle of the fibre orientation increases, the failure mode of CFRP gradually changes from fibre failure mode into shear failure mode. It is followed by purely matrix failure mode. The latter needs a lesser amount of energy when compared to the fibre fracture mode since the matrix is much weaker than the fibres. Hence, lower tensile fatigue strength is measured for fibre orientations with higher angles and a smaller S-N curves gradient [43].

The temperature effect on overall material behaviour is crucial in the case of CFRP material and for all different types of material that exists. Due to the difference in the thermal coefficients between different composite constituents, the effect is further accentuated by variation in fibre orientations. Barron et al. [44] and later Gornet et al. [45] presented the influence of shearing by variation in the fibre orientation towards the self-heating ability of the CFRP material. Their work found that the material shows a more pronounced capability to self-heat as shearing increases. This is due to the kinetic energy that forms through shearing between fibre and matrix, which later dissipates in the form of heat energy. The release rate of this energy (visco-plastic energy release rate) is the highest in the case of CFRP specimens having 45° fibre orientation, given that the maximum shear stress occurs at this angle. Moreover, the increase in temperature occurring in a shear-dominated mode

specimen of CFRP material can also be explained through the increase in vibration of polymeric chain networks within the CFRP material, which causes matrix softening. This later affects the stress transferability between fibre and matrix and consequently matrix straining. Substantial damage and reduction in fatigue lifetime is therefore expected in this event and could be further intensified by inhomogeneous self-heating throughout the specimen, making failure mechanisms interaction even more complex [46].

Manufacturing process. Several manufacturing processes are involved in every preparation of CFRP specimen. Unfortunately, CFRP material could be adversely affected during the manufacturing process as the production of defect-free specimens is unattainable even in the modern world today [13, 47]. CFRP material undergoing the cutting process has been shown to develop residual stresses [48]. The development of these residual stresses is mainly due to the thermal and chemical effect in the material introduced through the cutting process. This is due to the considerable variation in the thermal expansion coefficient from one constituent to another, including chemical shrinkage. A combination of these factors also prompts unwanted temperature variation across the material, forming tensile residual stress within the material. Residual stress within the material often becomes the inducing factor for delamination for CFRP material [49]. The material reaction towards the curing process could also contribute to the increase in internal residual stresses or strains. This often builds up during the contraction of resin while solidifying [50], which leads to increased overall internal residual stresses, thus limiting the fatigue life of CFRP material [51, 52].

The curing process is often associated with void formation within the material. These undesirable effects are motivated by the air bubbles trapped in the matrix during curing. Poor wetting between fibre and matrix is not the only accidental outcome of this issue but also severely affects the material's intra- and inter-laminar properties, damaging results towards fatigue performance [13, 53, 54]. Voids within the material are one of the most detrimental defects under fatigue loading as it also acts as a stress concentrator that leads towards material delamination [55, 56]. Stiffness degradation has also been enhanced by voids availability within the CFRP material under cyclic loading [57]. There are a lot of other related defects introduced during the manufacturing process, making it one of the essential aspects when discussing CFRP fatigue performance.

Other factors. Several other factors greatly influence CFRP materials' fatigue performance, including fibre volume fraction. As fibre stiffness and strength considerably affect the overall mechanical properties of CFRP material, higher fibre volume fractions also clearly affect the fatigue performance [32]. Fibre volume fraction can be defined as the

ratio between the amount of fibre compared to the matrix of the composite material. At a higher value of fibre volume fraction, more stiff fibres are available to carry the load effectively within the area. Therefore, a lower load is carried by the matrix. This hampered the matrix straining and reduced the damage accumulating within the matrix [58]. Apart from that, the fibre volume fraction is also responsible for the effect of the dominant damage mechanism depending on the fatigue stress level applied to CFRP material [30, 59]. High amount of fibres in the material also mean lesser matrix material to bind the whole thing together. Unfortunately, this also means that the medium to transfer the stress are reduced, causing inefficient stress distribution within the material. This indirectly reduces the strength of the composite material. The stacking sequence of a laminate composite affects the fatigue performance [60]; it is also found that this individual factor when combined with other existing macro-defects, could reduce up to 50% of the material's ultimate strength [61]. As presented earlier, three different types of carbon fibre construction are commonly used in CFRP composite. Each of these types brings different characteristics to the overall material. For example, the fatigue performance of CFRP made out of textile carbon fibres have improved fatigue response over delamination compared to UD CFRP [62]. The fatigue response of CFRP material is undoubtedly a complex area of study as there have been numerous reported factors that directly influence the fatigue lifetime. Many factors are not discussed here, such as the stress ratio effect [27, 28] and many more. However, this complex behaviour indicates demand for the material to be further studied and tested systematically, which could be accomplished through standard testing guidelines.

2.4 Standard Macroscopic Testing and its Limitations

Owing to the complexity of CFRP material response under various loading conditions (especially under fatigue loading), several standards in the attempt to offer guidelines for systematic analysis of the material are commonly available [63–65]. Despite all of the available standards, there are still several limitations and problems that researchers face when attempting to understand and characterise a given CFRP material.

Due to the substantial difference between the material strength of a CFRP in the longitudinal direction (parallel to fibre direction) and in the transverse direction, standard specimens often require geometry adaptation to capture the effective load, especially when different fibre orientations need to be tested [3, 9]. This often involves reducing the thickness or even width of the specimen, which indirectly introduces the specimen geometry effect as a natural consequence of this adaptation. Apart from this, the specimens tab on both ends of the specimen for load application is sometimes necessary, especially in the

case of CFRP material, which is high strength and highly orthotropic. Using a tab in such testing is crucial to safeguard the specimen from damage induced by the applied load or increase the effective loading area. Unfortunately, such installation becomes challenging when combined with geometry adaption established earlier [9]. Ineffective installation of tab in geometry adapted specimens might even cause the unwanted failure of the specimen during testing whereby the material could fail within the tab area itself rather than the gauge designated section of the specimen. This unfavourable specimen damage does not represent the intended actual material behaviour and certainly severely affects the validity of the test.

Such difficulties could arise due to the gap between the operating scale suggested by the standard testing guidelines and CFRP materials' actual damage mechanism. This is because standardised testing has been used as guidelines on material testing of macro-level specimens to seek an understanding of CFRP fracture behaviour. However, the primary damage mechanism within CFRP material under fatigue loading is microcracks formation - a damage mechanism on a micro-scale level, unlike in metallic materials [66]. Due to this scale disparity, fracture response between standard testing specimens slightly differs from the actual response of the material. Standard specimens of CFRP material usually contains a large number of fibres resulting in a brittle fracture response and sudden rupture of the specimen when loaded. This is due to the large amount of energy stored within the specimen released almost immediately when the material reaches its fracture limit, resulting in a catastrophic abrupt failure. Such response indicates that the standard specimen testing offers a fracture response that is much closer to the simple structure level response and not material level response.

Indeed, a material level response means that the evolution of damage within the specimen will be nearly progressive. Owing to the brittle response in the fracture manner of the standard specimens, fragmentation of these specimens is commonly seen. This dramatically reduces the possibility for in-depth fracture surface analysis studies on standard specimens, which necessitates understanding the failure mechanisms behind the applied condition. Severe delamination commonly seen on longitudinal specimens during standard testing [67] (even without specimen fragmentation) results in broken specimen with fracture surface that is highly uneven [9]. It reiterates the challenge to study the fracture mechanisms involved within the CFRP material. Moreover, standard testing does not offer an in-situ observation of fatigue fracture. All of these issues justify the importance of a supporting test presented in Chapter 4 that offers a micro-level response of CFRP material to understand the actual fracture mechanism further. The knowledge that is close to the ma-

terial level response through testing and modelling will yield new and precise insights into better understanding, managing and designing CFRP structures for the optimum mechanical performance of fatigue [13]. Furthermore, this will provide insight into building a more accurate material model to allow better material response prediction and minimise the CFRP fatigue performance dependency on various levels.

2.5 Damage Modelling Approaches

As extensively discussed in previous sections, the response of CFRP under fatigue loading is very complex and different from metals. Metallic material that undergoes fatigue loading shows no significant stiffness degradation [8], making it advantageous for modelling since a linear relationship between stress and strain is applicable. Unlike metals, composites develop a damage zone within the material under fatigue and fail due to various failure mechanisms that occur individually or as an effect of interactions between them [32]. Several earlier microcracks that form at the beginning of fatigue loading could also merge to form a macrocrack and cause further damage to the material through delamination [19]. The complexity of composite fracture behaviour lies mainly in stiffness degradation that starts from the early stage of loading through the whole fatigue duration of the material. This causes stress redistribution to the undamaged part of the material, and, as a result, applying a classical approach through fracture mechanics is a challenge [8, 68]. Considering that the failure behaviour of CFRP highly depends on the interaction of failure mechanisms throughout fatigue, fatigue load history is an important aspect that needs to be accounted for to predict damage evolution within the material. Many attempts to account for the fatigue load history have been made to model fatigue of FRP [13, 62, 69, 70].

General problems to model fatigue of CFRP material. There are several complications in the fatigue damage model of CFRP material [8]. One of the most apparent problems in modelling is the knowledge gap that involves different scales of information being put together. For instance, the damage mechanisms involved in CFRP are on a micro-level scale affecting fibres and matrix; individual lamina provides meso-scale information while components and standard testing provide simple structure level response at macro-scale [66]. Not only that the knowledge scale differs, but it is also challenging to model stiffness degradation of a material under fatigue. This is usually done based on reference data obtained through the standard testing. Unfortunately, material stiffness degradation measurements are very challenging due to the specimen surface damage and undesirable signal noise [3]. Most of the available fatigue models are built on the assumption that the model is applicable throughout the entire fatigue lifetime. However, the prediction on a particular

region is not necessarily accurate [71]. The fatigue model usually requires a set of material parameters. Naturally, the more accurate the material model is, the more material parameters are required. An accurate material model usually results in many material parameters that often involve particular parameters that are challenging to determine through standard testing [72]. Hence, making the model impractical to apply. To compensate for the unfeasibility of the model, simplification to the curve fitting of experimental data has to be considered. Unfortunately, in most cases, this simplification underestimated the actual fracture response of CFRP material under fatigue loading and affected the accuracy of the overall model [73].

The intricacy of fracture behaviour in CFRP can be associated with the number of cycles the material is exposed under cyclic loading [71, 73]. Due to this reason, accurate prediction on damage evolution within the material can only be made with a thorough consideration of the entire load history that the material is subjected to [74]. Taking into account the entire load history is especially the case when variation in repeated blockwise loading occurs. The loading is one factor that accelerates the material's degradation from the early stage of loading [75]. All of these issues, including other factors affecting the fatigue performance of CFRP discussed previously, certainly contribute toward a challenging task to model fatigue damage in CFRP material. As a general rule, all available fatigue damage models can be categorised into three main groups. These categories are fatigue life models, phenomenological models, and progressive models. A more detailed account of all fatigue damage model categorisations presented here can be found in Refs. [6, 8, 13].

Fatigue life model. The fatigue damage model that falls within this category shares the same characteristics. The model is based on diagrams (S-N curve or other diagrams) combined with several fatigue failure criteria without any features of actual damage degradation mechanisms. One of the earliest fatigue damage models was introduced by using S-N curves or the Wöhler-Miner approach model [76, 77]. Hashin and Rotem later developed a plane stress damage model based on S-N curves applicable for UD FRP material [78]. In their model, two different failure mechanisms based on fibre failure and matrix failure have been considered. However, this model is directly applicable only in the case of laminate based on UD ply when these two distinct failure mechanisms can be separated. Sendeckyj in his model [79], associated the concept of equivalent static strength based on statistical analysis on constant amplitude fatigue strength data.

Several other damage models under this category present different ideas in their definition of fatigue failure criterion based on two scales. The first one is based on average stress, which considers the material properties and adhesive bonding between fibre and matrix

at the micro-scale level [80], and Tsai-Hill failure criterion at the macro-scale level [81]. An often employed strategy is to calibrate multiaxial models with carefully selected reference. This allows to reduce the amount of fitting parameters in the damage model and was shown to provide quite accurate results [82]. The generalised concept of damage accumulation introduced in Miner's rule is widely employed in other damage models for fatigue life predictions [83, 84]. This shared concept has also been modified and combined with other fatigue analysis algorithms such as rainflow counting for glass fibre reinforced polymer (GFRP) materials [85] or with fatigue failure criterion (Puck's criterion) that highly depends on the number of cycles that the material is exposed to [59, 86].

Apart from fatigue damage models based on S-N curves, a constant fatigue life (CFL) or Goodman diagram has also been widely used. This diagram helps to illustrate the effect of mean stress in fatigue loading [87–91]. The widely used diagram relates alternating stress versus the number of cycles to failure to the mean stress of the tested material. This plot produces a direct relationship to quantify the effect of mean stress towards fatigue lifetime of the material. Based on this diagram, two publications by Beheshty et al. [92, 93] showed the effect of impact damage on fatigue response. The effect of impact damage was incorporated by assuming a reduction in the material's compressive strength.

Overall, the high numerical efficiency presented by the fatigue life model is a great advantage as this model could be utilised in the post-processing stage of structural analysis. However, this approach often requires many experiments for each material configuration [94]. Moreover, the model does not constitute viable stress redistribution and degradation during the entire fatigue lifetime. The absence of specific actual fatigue failure effects results in difficulties applying these models to the case involving load histories with substantial variation in non-harmonic loading [3].

Phenomenological models. Phenomenological models are different from fatigue life models because this group is designed to capture the degradation (stiffness or strength) within CFRP material. This group of models associates the damage evolution equation with the chosen material properties that are often measurable through standard testing (macro-scale level). However, no actual damage mechanism is included in the damage evolution equation. According to Paepegem [8], the damage model in this group can be further divided into two classifications: residual strength models and residual stiffness models. In residual strength models, the approach focuses on the degradation of the initial static strength of the material. One of the earliest models in this category is presented by Halpin et al. [95]. Their model assumes that when a material is loaded under fatigue, it will undergo continuous degradation in strength. The model is based on crack propagation sim-

ilarly as seen in metallic material. Unlike this model, a model proposed by Daniel and Charewicz [71] only considers residual strength as the sole factor causing fatigue damage. Based on their model, it is assumed that two specimens under two different cycles will have the same amount of damage, provided that they have the same residual strength at the end of their cycles. The definition of damage evolution presented in this group sometimes relates directly to the applied stress [96] while others introduce another limit such as imaginary strength S_0 [97] to indicate failure accumulation. An attempt to model the cycle mix effect similarly as discussed by Farrow [75] has also been made by Schaff and Davidson [94, 98] based on a fighter aircraft actual load history.

Another classification of the phenomenological model is based on the residual stiffness of the material. In this type of model, it is assumed that the material under fatigue experiences degradation of its elastic properties. Failure accumulation within the material is often assumed from the comparison of fatigue properties against static mechanical properties such as static failure secant modulus [99] or static ultimate strain [100] which has also been used by Kam et al. [101]. The effect of different types of loading, tension and compression loading, towards damage evolution has also been addressed by Sidoroff and Subagio [102], whereby the model assumed that only tension loading contributed towards fatigue damage evolution. The model has been later modified in terms of stress amplitude from the original strain amplitude [103]. Kawai [104] has also made further adaptations by proposing the concept of effective stress to replace maximum fatigue stress in the case of off-axis fatigue in UD CFRP materials. Interestingly, some of the derived models based on metallic materials have also been applied to FRP materials [105].

Despite an elaborate effort to model degradation in CFRP under fatigue loading, some models still face problems representing degradation accurately across the entire fatigue life as observed in the actual experiment. The difficulty is possibly due to the model inadequacy to predict material deformation throughout the entire loading cycle caused by various interacting elements [106]. However, most of the models show an excellent capability to predict the fatigue life of the material [13].

Progressive models. The final category of fatigue damage models is progressive models. The damage evolution equation is associated with the actual failure mechanism observed experimentally in CFRP material in these models. A model by Shokrieh and Lessard [107, 108] can fuse three elements, stress analysis, failure analysis and material degradation, into one and delivers relatively good prediction. Although the model requires quite a considerable number of parameters [13], a similar idea that adopts delamination as the dominant failure mechanism was later proposed by Papanikos et al. [109] and Tserpes et al. [110]. The

cycle-jump technique was used to reduce computational efforts significantly. The concept was further applied by Kennedy et al. [72], using modified Puck's criterion [111, 112] and cumulative damage Miner's rule. In contrast, the work by Mohammadi et al. [113] is presented in a more simplified manner. The only setback of these models is that the model application is somewhat restricted to a set of repeated cyclic fatigue loadings [3].

Since delamination is one of the central failure mechanisms in CFRP material, close attention has been given to this area. Some of the models feature this failure mechanism employing cohesive interface elements [114, 115]. In contrast, others use local material information associated with virtual damage variables to identify the crack tip [116]. With the rapid development in continuum damage mechanics (CDM), progressive models based on CDM seems to be the best approach [8, 117–119]. Examples of CDM based models include Talreja's work [120–122] and Haojie et al. [123], which features interacting failure mechanisms as damage driving mechanisms. The model introduced by Talreja [120] earlier and Matzenmiller et al. [124] in two-dimensional anisotropic composites were subsequently expanded into three dimensional by Böhm et al. [125]. To be efficiently applied on larger scale computations, the failure criteria and damage models proposed by Dávila et al. [126], Pinho et al. [127–129] and Maimí et al. [130, 131] provide a reliable framework to predict damage evolution based on the physical concept of material fracture by also including crack closure effect from load reversal.

Despite being a static damage model that is restricted to failure under static overloading, this thesis will place a special focus on the latter approach due to its physical-based concept of material fracture in the damage model. This approach is mainly based on a constitutive model that relates failure mechanisms with a set of internal variables. It uses three scalar damage variables d_1, d_2 and d_6 to represent longitudinal fibre failure, transverse matrix failure and combination of both failures, respectively. The constitutive equation for this approach is given by:

$$\begin{pmatrix} \varepsilon_{11} \\ \varepsilon_{22} \\ 2\varepsilon_{12} \end{pmatrix} = \begin{pmatrix} \frac{1}{(1-d_1)E_1} & -\frac{\nu_{21}}{E_2} & 0 \\ -\frac{\nu_{12}}{E_2} & \frac{1}{(1-d_2)E_2} & 0 \\ 0 & 0 & \frac{1}{(1-d_6)E_6} \end{pmatrix} \begin{pmatrix} \sigma_{11} \\ \sigma_{22} \\ \sigma_{12} \end{pmatrix} \tag{2.1}$$

Both damage variables d_1 and d_2 present two separate damage modes that are based on types of loading applied, precisely tension or compression loading. The distinction based on loading mode is vital due to the resulting difference in the type of failure, and it is made based on the sign of the corresponding normal stress. By doing this, the crack closure effect can be taken into account effectively.

In order to describe the complex stress-strain state, the Langley criteria (LaRC03/04) [126–129], are employed in the model. The elastic region comprises of four failure envelopes are defined as follows,

$$F_{1+} = \Phi_{1+} - r_{1+} \leq 0 \tag{2.2a}$$

$$F_{1-} = \Phi_{1-} - r_{1-} \leq 0 \tag{2.2b}$$

$$F_{2+} = \Phi_{2+} - r_{2+} \leq 0 \tag{2.2c}$$

$$F_{2-} = \Phi_{2-} - r_{2-} \leq 0 \tag{2.2d}$$

where F_i, $\Phi_i(\tilde{\sigma}_{ij}, R_i)$ and $r_i = 1$ are the damage activation functions, loading functions and elastic damage thresholds, respectively, whereas $\tilde{\sigma}_{ij}$ are the nominal stresses. The sign on the four failure envelopes corresponds to the different fracture modes, a transverse or longitudinal failure, similarly to the loading functions.

Four loading functions conform to four different types of failure are considered in this approach (longitudinal and transverse failure under tension and compressive mode). The first one is the longitudinal tensile failure. This failure mode involves fibre fracture that occurs in the material's weakest region, which later increases the normal and fibre/matrix interfacial shear stresses in the neighbouring fibres. The increase in the local stress concentration subsequently promotes other failure mechanisms such as matrix cracking and fibre-matrix debonding. Failure for the internal loads to redistribute effectively leads to a complete material failure in the form of a microcrack perpendicular to the fibre direction. This specific failure criterion is described based on maximum stress allowable in the longitudinal direction as presented in Eq. (2.3).

$$\Phi_{1+} = \frac{\tilde{\sigma}_{11} - \nu_{12}\tilde{\sigma}_{22}}{R_{11}^{t}} \tag{2.3}$$

with σ_{11} and σ_{22} are the nominal stresses in the direction of x_1 and x_2 respectively, and R_{11}^{t} is the tensile strength in fibre direction.

In the case of compressive longitudinal failure, the material fails under the event of shear kinking and neighbouring matrix damage by which fibre started to misalign locally, inducing the increase in shear stresses between fibres which rotate the fibres further. The fibre rotation increases shear stresses even more and results in the loss of load-carrying capacity of the fibres. The criteria defining the longitudinal compressive failure is

$$\Phi_{1-} = \frac{\langle |\tilde{\sigma}_{12}^{\mathrm{m}}| + \eta^{\mathrm{L}}\tilde{\sigma}_{22}^{\mathrm{m}} \rangle}{R_{12}^{s}} \tag{2.4}$$

where R_{12}^s is the shear strength in the fibre plane and the approximation for the longitudinal friction coefficient [126]

$$\eta^L \approx -\frac{R_{12}^s \cos(2\alpha_0)}{R_{22}^c \cos^2 \alpha_0} \tag{2.5}$$

with the stresses in the misaligned coordinate σ_{ij}^{m} as

$$\tilde{\sigma}_{22}^{\mathrm{m}} = \tilde{\sigma}_{11} \sin^2 \varphi^C + \tilde{\sigma}_{22} \cos^2 \varphi^C - 2|\tilde{\sigma}_{12}| \sin \varphi^C \cos \varphi^C \tag{2.6a}$$

$$\tilde{\sigma}_{12}^{\mathrm{m}} = (\tilde{\sigma}_{22} - \tilde{\sigma}_{11}) \sin \varphi^C \cos \varphi^C + |\tilde{\sigma}_{12}| (\cos^2 \varphi^C - \sin^2 \varphi^C) \tag{2.6b}$$

herewith the misaligned angle φ^C

$$\varphi^C = \arctan\left(\frac{1 - \sqrt{1 - 4\left(\frac{R_{12}^s}{R_{11}^c} + \eta^L\right)\frac{R_{12}^s}{R_{11}^c}}}{2\left(\frac{R_{12}^s}{R_{11}^c} + \eta^L\right)} \right) \tag{2.7}$$

R_{22}^c and R_{11}^c are the compressive strength perpendicular to the fibre direction and compressive strength in the fibre direction, respectively.

There are two individual types of transverse fracture considered in this approach. These fractures include matrix cracking and fibre-matrix interface debonding that emerge only within the matrix and the fibre-matrix interface. The first type is transverse fracture perpendicular to the fibre direction with fracture angle $\alpha_0 = 0^\circ$. This fracture is induced by a combination of σ_{12} with either one of the following stresses, σ_{22}^t or a small value of σ_{22}^c. The failure criteria are given as

$$\Phi_{2+} = \begin{cases} \sqrt{(1-g)\frac{\tilde{\sigma}_{22}}{R_{22}^t} + g\left(\frac{\tilde{\sigma}_{22}}{R_{22}^t}\right)^2 + \left(\frac{\tilde{\sigma}_{12}}{R_{12}^s}\right)^2} & \text{for} \quad \tilde{\sigma}_{22} \geq 0 \\ \frac{1}{R_{12}^s}\left\langle |\tilde{\sigma}_{12}| + \eta^{\mathrm{L}} \tilde{\sigma}_{22} \right\rangle & \text{for} \quad \tilde{\sigma}_{22} < 0 \end{cases} \tag{2.8}$$

Fracture toughness ratio $g = \frac{G_{Ic}}{G_{IIc}}$ is the ratio between mode I and mode II interlaminar fracture toughness while R_{22}^t is the tensile strength perpendicular to the fibre direction.

In the case where the material undergoes high transverse compressive stresses $\tilde{\sigma}_{22} < 0$ compared to the in-plane shear stress, where the loading closely resembles pure transverse compression, the fracture angle $\alpha_0 = 53^\circ$. The failure criterion for this case is

$$\Phi_{2-} = \sqrt{\left(\frac{\tilde{\tau}_{\mathrm{eff}}^{\mathrm{T}}}{R_{22}^s}\right)^2 + \left(\frac{\tilde{\tau}_{\mathrm{eff}}^{\mathrm{L}}}{R_{12}^s}\right)^2} \tag{2.9}$$

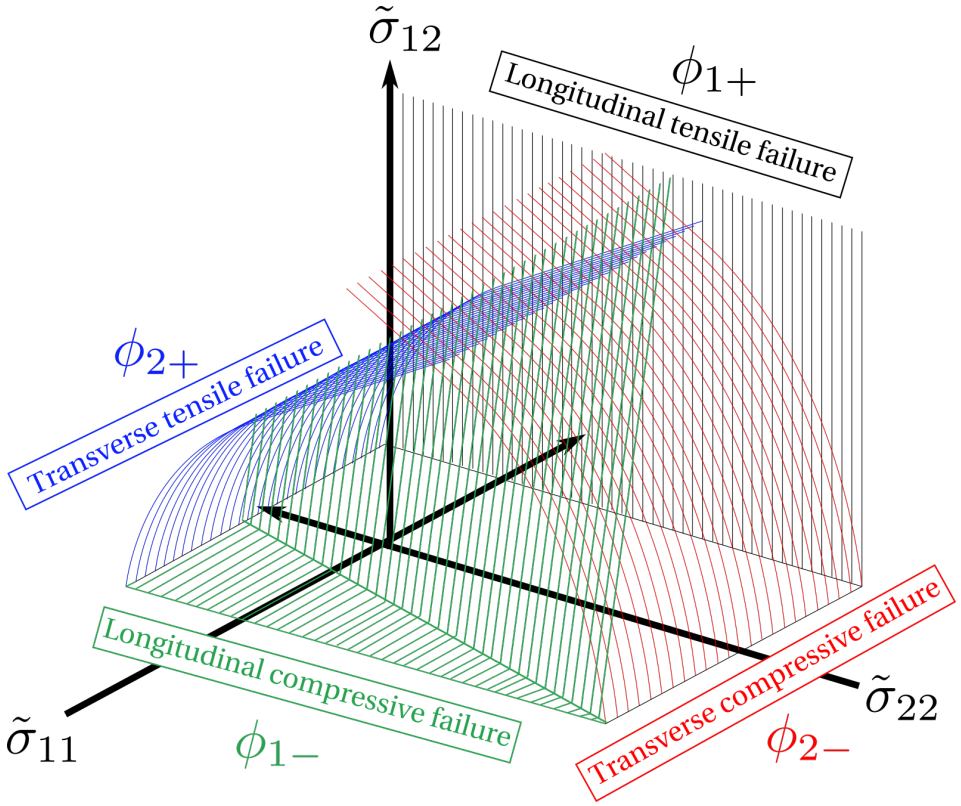

Figure 2.3: Four surfaces that bounded the elastic domain adapted from Miami et al. [130, 131]

with the effective stress components $\tilde{\tau}^{\mathrm{T}}_{\mathrm{eff}}$ and $\tilde{\tau}^{\mathrm{L}}_{\mathrm{eff}}$ is determined as Pinho et al. [127]

$$\tilde{\tau}^{\mathrm{T}}_{\mathrm{eff}} = \left\langle -\tilde{\sigma}_{22}\cos(\alpha_0)\left[\sin(\alpha_0) - \eta^{T}\cos(\alpha_0)\cos(\theta)\right]\right\rangle \tag{2.10a}$$

$$\tilde{\tau}^{\mathrm{L}}_{\mathrm{eff}} = \left\langle \cos(\alpha_0)\left[|\tilde{\sigma}_{12}| + \eta^{L}\tilde{\sigma}_{22}\cos(\alpha_0)\sin(\theta)\right]\right\rangle \tag{2.10b}$$

including the sliding angle θ

$$\theta = \arctan\left(\frac{-|\tilde{\sigma}_{12}|}{\tilde{\sigma}_{22}\sin(\alpha_0)}\right) \tag{2.11}$$

The transverse friction coefficient is computed by

$$\eta^{T} = \frac{-1}{\tan(2\alpha_0)} \tag{2.12}$$

The elastic domain in the $\tilde{\sigma}_{11}$, $\tilde{\sigma}_{22}$ and $\tilde{\sigma}_{12}$ can be presented in the Figure 2.3. In the actual case, the transverse failure criteria can be maximised to find the actual fracture angle involving an increase in the in-plane shear stress. However, a simplified approach with only two possible values of fracture angle 0° or 53° is shown to be sufficient [130, 131].

There are several essential features for the damage evolution model of this approach.

These features are, (i) the elastic domain thresholds r_N are directly related to the damage variables, (ii) the loading functions are determined based on the strain tensor, and (iii) the damage activation function correlates both (i) and (ii) to ensure a smooth link between CFRP failure mechanisms with the damage evolution concept. Initially, when the material is undamaged, the elastic domain threshold starts at one and continues to increase with the increase of damage. The damage activation function will remain negative for as long as the material behaves elastically. However, when $F_N = 0$ and $\dot{\phi_N}$ are positive, damage in the material is activated. A direct relationship between failure mechanisms with the damage evolution concept provided in this approach sets a good example of how a complex stress-strain state in the fracture of material can be addressed for a more accurate fatigue damage model.

The undeniably great effort to introduce various approaches to model fatigue failure in CFRP material reflects the complexity of the failure behaviour. In general, fatigue life models are limited due to incomplete treatment of stiffness degradation, stress redistribution and difficulties in their application towards non-harmonic cyclic loads with complex variations. On the other hand, phenomenological models describe fracture response that is much closer to simple structure level response due to the relation of its damage variables to measurable macroscopic properties. Although most of the progressive or mechanistic models are case-specific, the CDM approach seems to be a promising technique due to its material level response. Therefore, a solution to an accurate fatigue damage model necessitates a damage model that offers accurate prediction closer to a material level response. With this, the model will be less sensitive to numerous factors affecting the fatigue performance of CFRP. Indirectly, this results in a model with minimal material parameters. Ideally, the required parameters should also be easily obtained through standard ply-based testing. In order to consider the individual as well as the synergy effect of the failure mechanisms throughout fatigue loading, the model requires applicability to all types of fatigue load history and needs to be numerically efficient even in the case that demands large scale computations. With the knowledge mentioned above, Chapter 3 of this thesis discusses a new alternative fatigue damage model to fulfil all of these criteria.

Chapter 3

Continuum Damage Model on Macro-Fatigue Specimens

3.1 Formulation

This section contains a brief presentation of the recently developed brittle continuum damage mechanics model for CFRP materials, which can be considered a generalisation of Matzenmiller et al.'s model to 3-dimensions [124]. The proposed model describes the degradation of FRP materials from the beginning up to the final failure of the material under fatigue load. It assumes the formation, growth and coalescence of microcracks as the dominant damage mechanism within the material. This includes the microcracks that form in the matrix between fibres or in the neighbouring matrix and fibre failure. The primary material response is assumed to be linear elastic, as for UD CFRP and other similar materials. The only source of nonlinearity within the model comes from the damage evolution and degradation of elastic moduli based on the anisotropic Hooke's Law formulation. Besides that, damage evolution within the material is assumed to be driven by microplastic work dissipation. The model considers the material stiffness degradation from the beginning of the fatigue load until the material reaches its final failure. In doing so, it incorporates

a unique effect for FRP materials under fatigue load that shows possible development of significant degradation in stiffness that occurs within the material starting from the initial range of the cyclic load. However, the rapid stiffness degradation in the material becomes nearly constant after several hundred cycles, before an accelerated stiffness degradation follows, until a complete loss of material stiffness and total failure of the material. This model is also applicable for all fatigue load history. It is formulated on a single-ply level, thereby naturally considering the interaction between plies and delamination driven by fatigue. The following sections will explain each component of the material model formulation more in detail.

3.1.1 Damage Variables

The material macroscopic response affected by the introduction of material damage is modelled based on Kachanov [132] and Lemaitre [133]. In association with the strain equivalence principle, the macroscopic "effective" stresses $\bar{\sigma}$ are related to the elastic strain of the material according to Hooke's Law:

$$\bar{\sigma} = (1 - D)\, E\varepsilon \tag{3.1}$$

where E is the elastic modulus of an undamaged material. Given this, the macroscopic "effective" stresses can also be defined as a function of the microscopic stress

$$\bar{\sigma} = (1 - D)\, \sigma \tag{3.2}$$

with D representing damage accrued within the material. There are three basic levels of accrued material damage defined in the formulation, mainly

$$\begin{array}{lllll} 0 & = & D & & \text{undamaged state} \\ 0 & < & D & < 1 & \text{partially damaged state} \\ & & D & = 1 & \text{complete damaged state} \end{array} \quad . \tag{3.3}$$

The introduction of damage variable D can be taken as a measure of the effective surface density of the microcracks, whereby it assumes that the load applied on the material will only be resisted by undamaged material. However, it is not an exact relation for several reasons, such as material inhomogeneity and stress concentrations development at the microcrack fronts. There are in total three separate damage variables D_1, D_2 and D_3 that represents microcrack orientation with respect to the three coordinate axes, with each of them corresponding to specific failure mechanisms. D_1 addresses microcracks that are normal to the fibre orientation, including fibre damage and failure. Meanwhile, D_2 and

D_3 are associated with the formation of microcracks between fibres besides fibre-matrix interfaces.

Additionally, it is assumed that the material response is linearly elastic, and this can be introduced through Hooke's law in its orthotropic form. Alongside elasticity parameters for the undamaged material (Young's and shear moduli E_i and G_{ij}, and Poisson's ratios ν_{ij}), damage variables can be introduced in Hooke's law as [1–3, 134]

$$\begin{pmatrix} \bar{\boldsymbol{\varepsilon}}_{\text{axial}} \\ 2\bar{\boldsymbol{\varepsilon}}_{\text{shear}} \end{pmatrix} = \begin{pmatrix} \mathbf{A} & \mathbf{0} \\ \mathbf{0} & \mathbf{B} \end{pmatrix} \begin{pmatrix} \bar{\boldsymbol{\sigma}}_{\text{axial}} \\ \bar{\boldsymbol{\sigma}}_{\text{shear}} \end{pmatrix} \tag{3.4}$$

with auxiliary matrices given by

$$\mathbf{A} = \begin{pmatrix} \frac{1}{(1-D_1)E_1} & -\frac{\nu_{21}}{E_2} & -\frac{\nu_{31}}{E_3} \\ -\frac{\nu_{12}}{E_1} & \frac{1}{(1-D_2)E_2} & -\frac{\nu_{32}}{E_3} \\ -\frac{\nu_{13}}{E_1} & -\frac{\nu_{23}}{E_2} & \frac{1}{(1-D_3)E_3} \end{pmatrix} \tag{3.5}$$

and

$$\mathbf{B} = \begin{pmatrix} \frac{1}{(1-D_2)(1-D_3)G_{23}} & 0 & 0 \\ 0 & \frac{1}{(1-D_1)(1-D_3)G_{13}} & 0 \\ 0 & 0 & \frac{1}{(1-D_1)(1-D_2)G_{12}} \end{pmatrix} \tag{3.6}$$

whereas $\mathbf{0}$ denotes a 3×3 zeros matrix. For notational simplicity, the strain and stress components are divided into axial and shear parts, which correspond to the diagonal and off-diagonal components of these tensors, respectively:

$$\bar{\boldsymbol{\varepsilon}}_{\text{axial}} = \begin{pmatrix} \bar{\varepsilon}_{11} & \bar{\varepsilon}_{22} & \bar{\varepsilon}_{33} \end{pmatrix}^T \tag{3.7a}$$

$$\bar{\boldsymbol{\varepsilon}}_{\text{shear}} = \begin{pmatrix} \bar{\varepsilon}_{23} & \bar{\varepsilon}_{13} & \bar{\varepsilon}_{12} \end{pmatrix}^T \tag{3.7b}$$

$$\bar{\boldsymbol{\sigma}}_{\text{axial}} = \begin{pmatrix} \bar{\sigma}_{11} & \bar{\sigma}_{22} & \bar{\sigma}_{33} \end{pmatrix}^T \tag{3.7c}$$

$$\bar{\boldsymbol{\sigma}}_{\text{shear}} = \begin{pmatrix} \bar{\sigma}_{23} & \bar{\sigma}_{13} & \bar{\sigma}_{12} \end{pmatrix}^T \tag{3.7d}$$

Note that Eq. (3.4) is only valid when the reference x_1 is considered to be in the fibre direction. A similar effective concept applies when all of the elastic moduli from the undamaged material are degraded by the damage variables. By this means, Eq. (3.4) can be considered as Hooke's law,

$$\bar{E}_i = (1-D_i)E_i \tag{3.8}$$

$$\bar{G}_{ij} = (1-D_i)(1-D_j)G_{ij} \tag{3.9}$$

$$\bar{\nu}_{ij} = (1 - D_i)\nu_{ij} \tag{3.10}$$

In the case of effective shear moduli, according to Eq. (3.6), two damage variables representing microcracks in both planes normal to the respective shear plane are responsible for degrading these constants. It is assumed that when either one of the damage variables $D_i \to 1$ or $D_j \to 1$, the material has lost its ability to carry the load in this direction. This assumption is advantageous in the sense whereby no additional damage variable responsible for shear damage is necessary, thus reducing the total number of damage variables present in the model. Considering Eq. (3.10) follows the compliance matrix symmetry condition, the initial elastic moduli E_i for undamaged material can be substituted with the degraded elastic moduli $\bar{E}_i$ to account for the damaged material state. Even though the material is initially transversely isotropic (i.e., $E_3 = E_2$, $G_{13} = G_{12}$, $\nu_{31} = \nu_{21}$ and $\nu_{13} = \nu_{12}$), the material became anisotropic as soon as damage variables D_2 and D_3 starts to develop. A rather similar model has been initially suggested by Matzenmiller et al. [124] with the difference in the applicability that is only suitable in 2D static damage (without fatigue), along with the use of independent shear damage variables to account for shear moduli.

3.1.2 Damage Evolution

One-dimensional considerations. The damage evolution within the material is represented by three damage variables D_i as shown in Eq. (3.4),(3.5) and (3.6). These damage variables grow from the initially given value up to the final computed loading time. It is assumed that the increase in material damage, dD depends on the amount of microplastic work density dissipated, dw^{mp} within a time increment. Herewith, micro-plasticity is defined as plasticity confined below the macroscopic yield limit with no significance on the macroscopic level. Micro-plasticity occurs within the material due to the microscopic gliding of polymeric chains in the matrix material. Microplastic deformation that develops under quasi-static loading or individual fatigue load cycles is considered limited. This results in a very small microplastic strain that is negligible when compared to elastic deformation within the material (see Figure 3.1), i.e., $\varepsilon^{\mathrm{mp}} \ll \varepsilon^{\mathrm{el}}$. Due to this reason, it is not considered in the macroscopic constitutive equation presented in Eq. (3.4). On the other hand, although the microplastic deformation under individual fatigue load cycles is minimal, repeated loading and unloading for a larger number of cycles causes dissipation accumulation. As a result, significant plastic work needs to be considered as it progresses into complete material damage. Suppose that the microplastic strain can be presented by the Ramberg-Osgood relationship, $\varepsilon^{\mathrm{mp}} \propto \left(\frac{\sigma}{E}\right)^n$. In this case, the microplastic strain increments

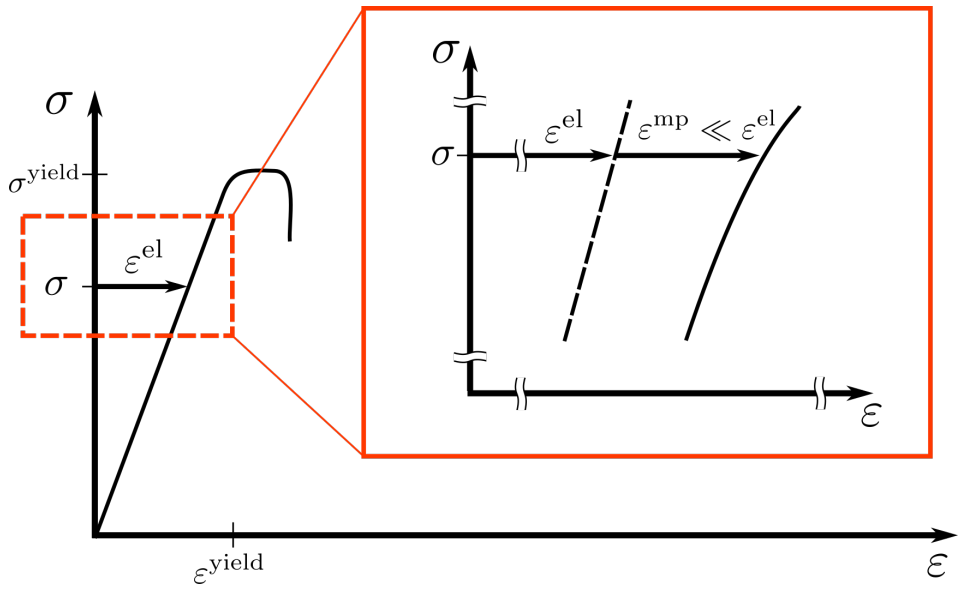

Figure 3.1: Micro-plasticity definition adapted from Hohe et al. [3].

can be approximately written as

$$\mathrm{d}w^{\mathrm{mp}} = \sigma\,\mathrm{d}\varepsilon^{\mathrm{mp}} \propto \frac{n}{E^n}\sigma^n\,\mathrm{d}\sigma \tag{3.11}$$

The one-dimensional damage evolution equation, including all material parameters (A and n), is then given by

$$\mathrm{d}D = A\,\omega(D)\,|\sigma|^n\,\mathrm{d}\sigma \tag{3.12}$$

in which all the constant prefactors were grouped into a phenomenological material constant A. Note that in the case whereby the stress level is negative, the absolute values are considered instead. By only taking the absolute value of the stress level, it is assumed that damage accumulation for both the loading and unloading part of the cycle is identical. Since a linear increase of the damage with load cycle is insufficient to represent the actual material behaviour, it is assumed that the damage increases similarly as the material loses its stiffness under fatigue loading (see Figure 3.2a), similarly as observed in experiments from Ref. [19]. For more details, see also Section 2.2. To achieve this behaviour, the (normalised) warping function $\omega(D)$, as illustrated in Figure 3.2b is introduced:

$$\omega(D) = \begin{cases} b + a_{\mathrm{I}}(D - D_{\mathrm{I}})^2 & \text{for } D \leq D_{\mathrm{I}} \\ b & \text{for } D_{\mathrm{I}} < D \leq D_{\mathrm{II}} \\ b + a_{\mathrm{II}}(D - D_{\mathrm{II}})^2 & \text{for } D > D_{\mathrm{II}} \end{cases} \tag{3.13}$$

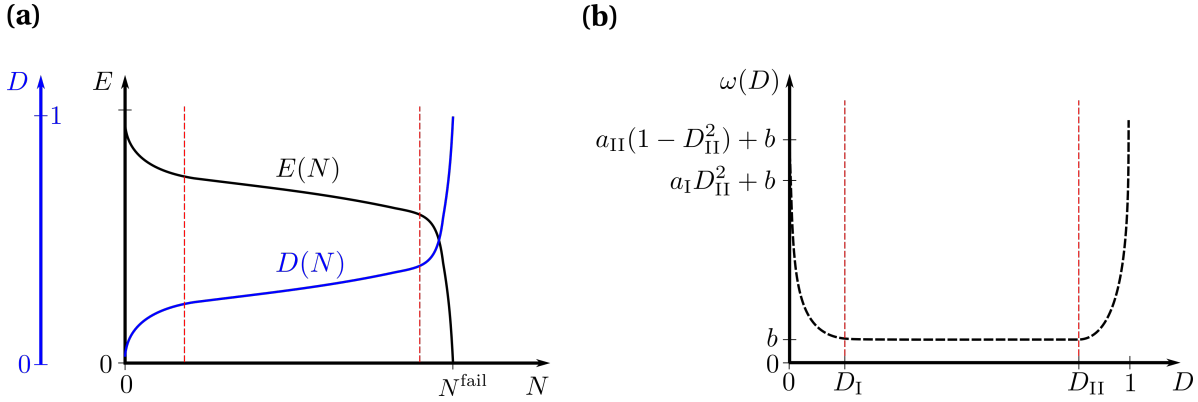

Figure 3.2: The damage evolution applied in the fatigue damage model (a: relationship between damage evolution and stiffness degradation and b: warping function). Adapted from Hohe et al.[3].

with

$$b \equiv 1 - \frac{1}{3} a_{\mathrm{I}} D_{\mathrm{I}}^3 - \frac{1}{3} a_{\mathrm{II}} (1 - D_{\mathrm{II}})^3 \tag{3.14}$$

due to the requirement

$$\int_0^1 \omega(D)\, \mathrm{d}D = 1 \tag{3.15}$$

Material parameters D_{I}, D_{II}, a_{I} and a_{II} are chosen such that the three stiffness degradation regions experienced by the material under fatigue loading can be represented. Here, the warping function presents damage evolution acceleration within the first region with small degrees of damage, D and in the third region at large degrees of damage approaching final material failure.

Three-dimensional considerations. The one-dimensional damage evolution equation presented in the section earlier is now expanded to supply for three-dimensional material consideration. In this case, it is assumed that each of the damage variables D_1, D_2 and D_3 are related to the three independent spatial directions x_1, x_2 and x_3 and they are all driven by stress components acting on the respective surfaces of the volume element. It is also assumed that the effects from all of the individual stress components can be added, resulting in

$$\begin{aligned} \mathrm{d}D_1 &= A_{11}\omega(D_1)|\sigma_{11}|^{n_{11}}|\mathrm{d}\sigma_{11}| + A_{12}\omega(D_1)|\sigma_{12}|^{n_{12}}|\mathrm{d}\sigma_{12}| \\ &\quad + A_{13}\omega(D_1)|\sigma_{13}|^{n_{13}}|\mathrm{d}\sigma_{13}| \end{aligned} \tag{3.16}$$

$$\mathrm{d}D_2 = A_{21}\omega(D_2)|\sigma_{12}|^{n_{21}}|\mathrm{d}\sigma_{12}| + A_{22}\omega(D_2)|\sigma_{22}|^{n_{22}}|\mathrm{d}\sigma_{22}| \tag{3.17}$$

$$
\begin{aligned}
& & & + A_{23}\omega(D_2)|\sigma_{23}|^{n_{23}}|\mathrm{d}\sigma_{23}| \\
\mathrm{d}D_3 &= A_{31}\omega(D_3)|\sigma_{13}|^{n_{31}}|\mathrm{d}\sigma_{13}| + A_{32}\omega(D_3)|\sigma_{23}|^{n_{32}}|\mathrm{d}\sigma_{23}| \\
& & & + A_{33}\omega(D_3)|\sigma_{33}|^{n_{33}}|\mathrm{d}\sigma_{33}|
\end{aligned} \tag{3.18}
$$

where A_{ij} and n_{ij} are material parameters and $A_{ij} \neq A_{ji}$ and $n_{ij} \neq n_{ji}$ (but $\sigma_{ij} = \sigma_{ji}$). Given the fact that the effect of microcracks development within CFRP material differs according to the type of loading (tension and compression loading), different material parameters have been used in the equation to treat these differences, i.e.,

$$
A_{11} = \begin{cases} A_{11}^{\mathrm{t}} & \text{for } \sigma_{11} \geq 0 \\ A_{11}^{\mathrm{c}} & \text{for } \sigma_{11} < 0 \end{cases} \tag{3.19}
$$

$$
A_{22} = \begin{cases} A_{22}^{\mathrm{t}} & \text{for } \sigma_{22} \geq 0 \\ A_{22}^{\mathrm{c}} & \text{for } \sigma_{22} < 0 \end{cases} \tag{3.20}
$$

$$
A_{33} = \begin{cases} A_{33}^{\mathrm{t}} & \text{for } \sigma_{33} \geq 0 \\ A_{33}^{\mathrm{c}} & \text{for } \sigma_{33} < 0 \end{cases} \tag{3.21}
$$

The same warping function for all damage variables and stress components has been considered to keep the available parameters to the minimum. Parameters A_{ij} is responsible for controlling the number of cycles to failure for different loading modes while exponents n_{ij} control the slope of the S-N curve. The influence brought by both parameters results in different amounts of damage accumulated for an identical amount of change in stress $\mathrm{d}\sigma_{ij}$ occurring at different stress levels $|\sigma_{ij}|$. A linear increase of damage with the change in stress is obtained when $n_{ij} = 0$, while an increase in damage accumulation $\mathrm{d}D_i$ with the change in stress is higher at higher stress levels $|\sigma_{ij}|$ when $n_{ij} > 0$.

3.2 Implementation

As can be seen from Eq. (3.4), the actual stresses are related to the actual strains and damage variables. Within the finite element approximation, this equation can be rewritten as

$$
\tilde{\boldsymbol{\sigma}}^{(k+1)} = \mathbf{C}(\mathbf{D}^{(k+1)}) \cdot \tilde{\boldsymbol{\varepsilon}}^{(k+1)} \tag{3.22}
$$

with

$$
\mathbf{C}(\mathbf{D}^{(k+1)}) \equiv \begin{pmatrix} \mathbf{A}^{-1}(\mathbf{D}^{(k+1)}) & \mathbf{0} \\ \mathbf{0} & \mathbf{B}^{-1}(\mathbf{D}^{(k+1)}) \end{pmatrix} \tag{3.23}
$$

and

$$\bar{\boldsymbol{\sigma}} = (\bar{\boldsymbol{\sigma}}_{\text{axial}} \quad \bar{\boldsymbol{\sigma}}_{\text{shear}})^T \tag{3.24a}$$

$$\bar{\boldsymbol{\varepsilon}} = (\bar{\boldsymbol{\varepsilon}}_{\text{axial}} \quad 2\bar{\boldsymbol{\varepsilon}}_{\text{shear}})^T \tag{3.24b}$$

$$\mathbf{D} = (D_1 \quad D_2 \quad D_3)^T \tag{3.24c}$$

On the other hand, the damage variables are dictated by the damage evolution equation, Eq. (3.12). Discretisation in time yields

$$\boldsymbol{D}^{(k+1)} = \boldsymbol{D}^{(k)} + \Delta\boldsymbol{D}(\boldsymbol{\sigma}^{(k+1)}, \mathbf{D}^{(k+1)}) \tag{3.25}$$

It is evident that Eqs. (3.22) and (3.25) form a set of coupled matrix equations: the second equation is implicit with respect to $\mathbf{D}^{(k+1)}$ and, via the dependence on $\boldsymbol{\sigma}^{(k+1)}$, the first equation becomes implicit with respect to the stress. Effectively, the value of the damage in the previous time increment is required which couples all the time increments from the beginning of the damage accumulation. This means that the entire loading history is taken into account to solve such system of equations. Solution of the sets of coupled matrix equations can be implemented using gradient descent methods or the Newton-Raphson method.

A vast number of cycles (>1,000 cycles) must be simulated in a typical fatigue loading test. Here, to compromise between the numerical cost and accuracy, only selected "representative" cycles were considered from across the loading history. Such cycle jump scheme for the damage accumulation in cyclic loading was implemented [8] by scaling the resulting damage increments in the actual cycles by their number per each representative cycle window, i.e., $\Delta D_i \rightarrow N_i^{\text{repr}} \Delta D_i^{\text{repr}}$.

It is crucial to ensure that the chosen integration time step is fine enough, especially when stresses are substantial. Note that the damage variable is proportional to $|\sigma_{ij}|^n$ where $n = 10$ is relatively high for CFRP materials, which might lead to errors or even lack of convergence when the time step is too crude. For the present analysis of CFRP materials, the above scheme was implemented in Abaqus finite element user-subroutine with the suitable cycle jump acceleration factor, N_i^{repr} value. Newton-Raphson algorithm was used to solve the coupled matrix equations iteratively. By combining all of the above, the proposed fatigue degradation model can be easily applied in structural fatigue assessment without sacrificing the ability to consider all of the conditions experienced by the material within its fatigue lifetime, including stress redistribution and stable fatigue crack growth within the material.

3.3 Results and Validations

3.3.1 Material and Experimental Methods

Several experiments have been done to create an experimental database to validate the damage degradation model discussed earlier. The reference material used for the investigation is a filament wound carbon fibre reinforced with epoxy matrix composite with 0.64 fibre volume fraction, commonly used in hydrogen or other pressure vessels made of composite. In order to acquire a plane plate to manufacture specimens required for the test, the material is wound around a thick plate that is used as a winding core. Two types of reinforced plates, uniaxial and multidirectional, with a stacking sequence of $[\pm 17.3°, 90°, \pm 70°]_s$ are processed. In the case of UD material, specimens of thickness 1 mm and 2 mm were manufactured. For specimens tested under 0° loading, the thickness of the specimens are 1 mm while for all other experiments, specimens with 2 mm thickness were used. As for multidirectional reinforced plates (MD), the ply thicknesses are about 0.31 mm for the $[\pm 17.3°]$ plies, 0.48 mm for the $[90°]$ plies and two times 0.13 mm for the centre $[\pm 70°]$ ply. The filament winding process causes $[\pm\alpha]$ plies to form interwoven layers instead of two separate $[+\alpha]$ and $[-\alpha]$ plies.

In the case of UD fibre reinforced material with 1 mm thickness, specimens of outer dimensions 240 mm × 15 mm are extracted to be tested under tensile loading within fibre direction. However, the width of some specimens was reduced to 10 mm to keep the required axial forces within acceptable limits. Specimens to be tested under tensile load perpendicular to the fibre direction were extracted from the thick UD plates with an outer dimension of 250 mm × 25 mm. In the case of tensile specimens extracted from MD laminates, the outer dimension of the specimens is 250 mm × 20 mm, whereas all compression specimens (UD and MD) outer dimensions are 155 mm × 10 mm.

The material characterisation was done based on two tests, mainly quasi-static and cyclic loading conditions. Regarding the quasi-static test under tension loading, a mechanical clamping system was used to test the specimens in an electromechanical Hegewald & Peschke machine up until specimen failure. The tensile test was done under displacement control with a displacement rate of 2 mm/min. As for the compression test, a specially designed parallel clamping was used with the same displacement rate as the tensile test. Both tests were done at room temperature with three types of recorded data, reaction force, crosshead displacement and axial strain, throughout the entire test duration to evaluate the stress-strain response of the material.

As for the case of fatigue test, a hydraulic MTS machine utilising the same clamping sys-

tem as in the tensile test previously was used under force control. Three fatigue stress ratios to represent tensile, compressive and alternating loads, denoted by $R = 0.1$, 10 and -1, with test frequencies between 0.1 Hz and 5 Hz depending on the applied fatigue load level and the resulting cyclic strains, were considered. The fatigue specimens were tested until complete failure or 100,000 cycles, where all of the specimens that reach 100,000 cycles without failing are considered run-outs. The maximum number of cycles limiting the fatigue test is determined based on the industrial requirements of composite gaseous fuel tanks that last up to 60,000 filling cycles throughout their operating lifespan. The force, displacement peaks, including the number of cycles for each specimen, are recorded throughout the test to evaluate fatigue specimens. The material stiffness degradation was measured by attaching strain gauges to some of the selected specimens. All of the tests were done at ambient temperature.

3.3.2 Experimental Results

The full results for quasi-static experiments under tensile and compressive load for both UD and MD reinforced laminates are presented in Hohe et al. [3]. A brittle response can be seen in most cases where the stress-strain curve is approximately linear. Most specimens experienced sudden failure, with no distinct plastic deformation observed. Only one of the 0° UD specimens (ZU1-1.2-01B-02) shows significant stress-strain curve nonlinearity before failing. In the case of all other specimens, a small nonlinearity just before the specimen fails can be seen, including 90° UD under compression. The elastic stiffness across all fibre orientations under both types of loading, tension and compression, show visible resemblance.

Figure 3.3 and 3.4 present results from fatigue test for all fibre orientations under three types of stress ratios. The following equation presents statistical analysis on distribution of errors for each data group,

$$f(\Delta \log \sigma) = \frac{1}{s\sqrt{2\pi}} e^{\frac{-(\Delta \log \sigma)^2}{2s^2}} \tag{3.26}$$

where s is the standard deviation of the data error and $\Delta \log \sigma = \log \sigma - (\log \sigma)_{\text{mean}}$. The mean of the distribution is represented as straight line in both Figure 3.3 and 3.4. It can be determined from

$$(\log \sigma)_{\text{mean}} = m \times \log N_f + c \tag{3.27}$$

where m and c is the gradient and intercept value while N_f is the number of cycles to

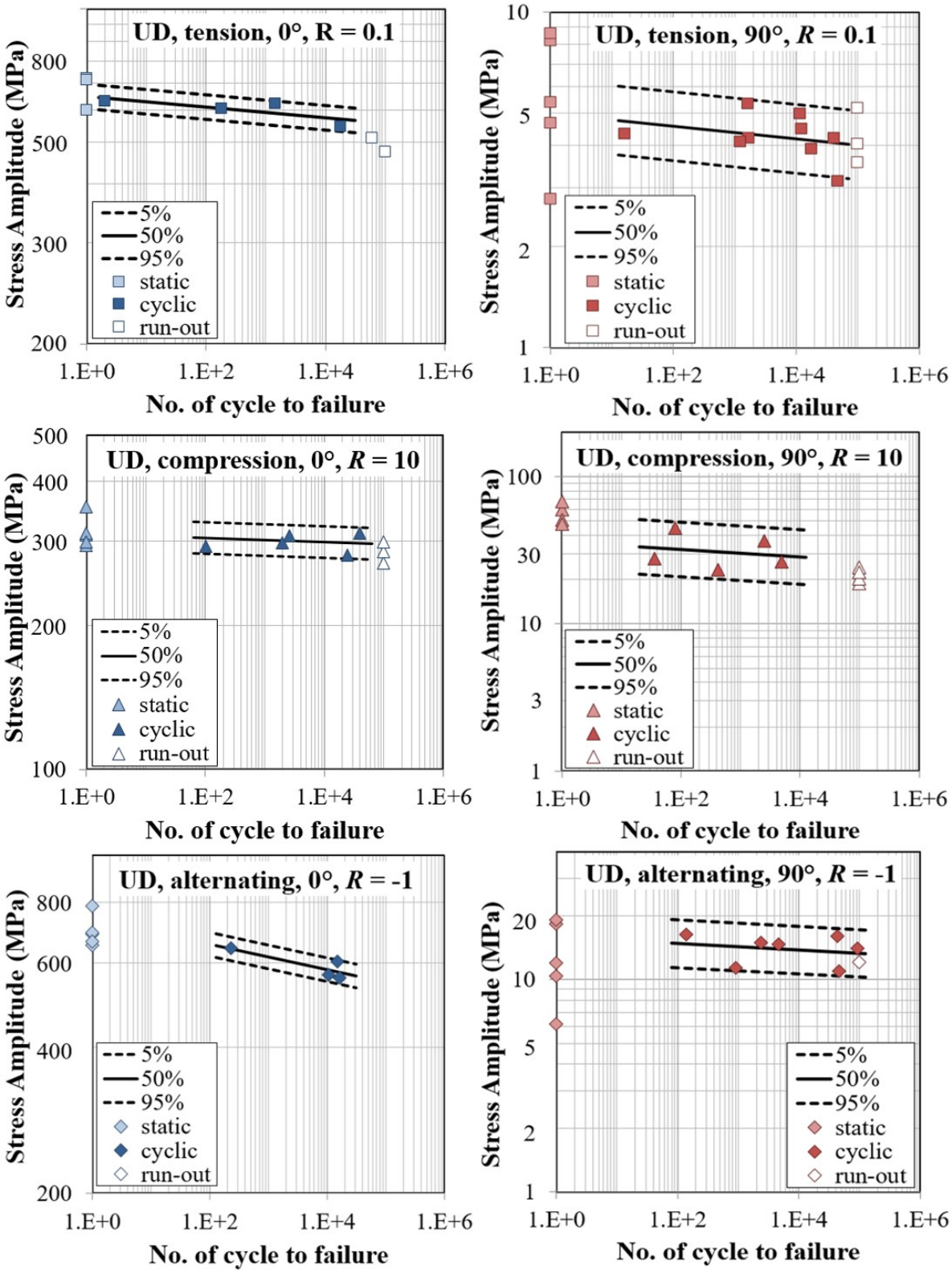

Figure 3.3: S-N curves for fatigue experiments on unidirectional specimens

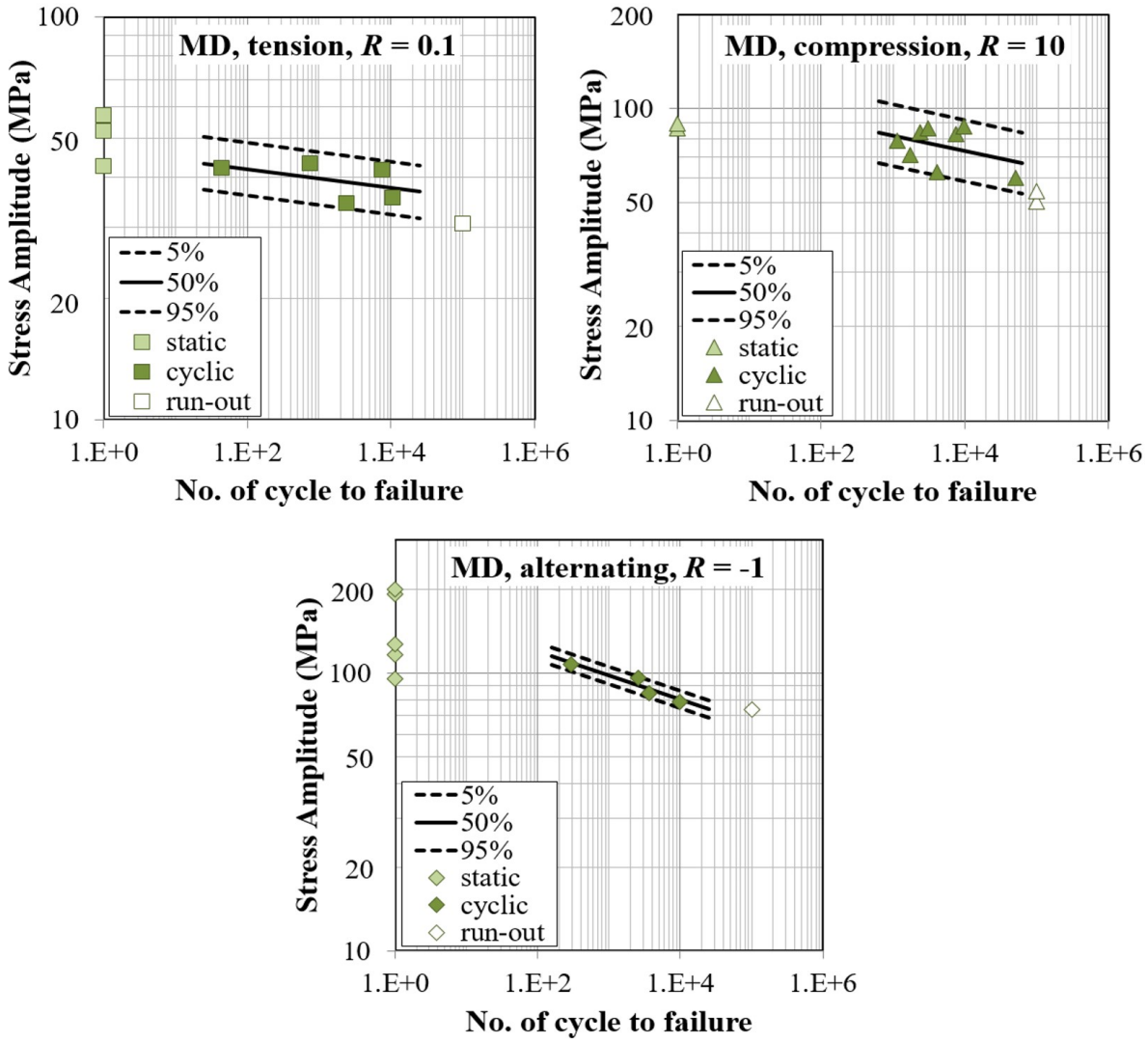

Figure 3.4: S-N curves for fatigue experiments on multidirectional specimens

failure. The 5%/95% quantile of the error distribution is shown in these figures as dashed lines and is defined by $\pm\alpha s$. The α is given as

$$\int_{-\alpha s}^{+\alpha s} f(\Delta \log\sigma)\, d\left(\Delta \log\sigma\right) = \mathrm{Erf}\left\{\frac{\alpha}{\sqrt{2}}\right\} = 0.90 \tag{3.28}$$

where α is found to be 1.64485 and the error function is given by

$$\mathrm{Erf}(x) = \frac{2}{\sqrt{\pi}} \int_0^x e^{-t^2}\, dt\,. \tag{3.29}$$

for real x. Results from run-out specimens, including quasi-static results that have been transformed into quasi-amplitude according to the respective stress ratio, are also included. A relatively small gradient is observed for all cases of fatigue tests. The absolute results scatter in all cases is relatively small, although 90° UD specimens show a slightly higher scatter.

There are quite a lot of difficulties in measuring the stiffness degradation of the material during fatigue loading. The difficulty arises from the heavy noise disturbances in the signal and specimen surface damage that causes inaccurate reading from the clip gauges attached to the specimen surface. Despite the difficulties, results on the stiffness degradation of the material obtained are presented in Hohe et al. [3]. Apparent initial degradation can be seen in two 0° specimens under tensile fatigue and one 0° specimen under compression fatigue load. Contrary to the case of 90° specimens, no initial degradation was observed in both types of cyclic loading. A distinctive stiffness degradation can be observed in MD specimens under tensile fatigue. This is probably due to interaction between the plies of different fibre orientations. Unfortunately, no conclusive local strain measurements for MD specimens under compression fatigue can be attained.

3.3.3 Parameter Determination

The fatigue degradation model that was introduced previously was applied to the experimental results in Section 3.3.2. According to several steps, all required material parameters concerning the damage evolution equations were determined based on the reverse engineering method. Firstly, all elastic constants are determined as the secant moduli from the quasi-static stress-strain curves roughly between 0.05% and 0.25% of nominal strain. It is also assumed that the material is transversely isotropic whereby direction x_2 and x_3 are equal. Combining all these, a single element FE computation under sinusoidal fatigue load is performed. In order to reduce computational time, fatigue degradation for the single element model is accelerated by using an acceleration factor of 1000 (cycle jump technique), whereby one computed cycle now represents 1000 actual cycles [8]. The FE computation

Table 3.1: Material parameters

Elastic parameters					
E_1 (GPa)	E_2 (GPa)	G_{12} (GPa)	G_{23} (GPa)	ν_{12} (-)	ν_{23} (-)
168.6	10.8	5.140	4.012	0.276	0.346
Warping function parameters					
a_I	a_{II}	D_I	D_{II}	b	
5.0	10.0	0.1	0.5	0.5	
Damage evolution parameters					
A_{11}^t (MPa^{-n+1})	A_{11}^c (MPa^{-n+1})	A_{12} (MPa^{-n+1})	A_{21} (MPa^{-n+1})		
3.25×10^{-40}	1.10×10^{-34}	0.50×10^{-8}	7.75×10^{-17}		
A_{22}^t (MPa^{-n+1})	A_{22}^c (MPa^{-n+1})	A_{23} (MPa^{-n+1})	n (-)		
2.75×10^{-17}	9.25×10^{-20}	0	10		

is then performed until the element completely fails. The element is assumed to fail when any of the damage variables D_1, D_2 or D_3 exceed 95%. The limit to define the final failure of the material is fixed at 95% to smoothen the drop in the stress-strain curve when the material reaches 100% damage. This step is necessary to guarantee numerical stability throughout the computation.

By considering two stress levels, parameters in the direction of x_1 and x_2 were varied to adapt to the experimental S-N curves. The same steps were done for both types of loading, tensile and compressive loading. It is found that taking an equal value for all of the n_{ij} parameters not only reduces the number of parameters required but also yield a good estimation. By doing this, we only require parameters A_{ij} to be modified for different loading modes. The list of all material parameters obtained is presented in Table 3.1. Although the material is treated to be transversely isotropic at the beginning, as damage variables $D_2 \neq D_3$ evolve, the transverse isotropy of the material is lost. The S-N curves from applying the fatigue degradation model are given in Figure 3.5. All cases presented in Figure 3.5 agree well with the experimental fatigue data producing a linear material response in double logarithmic relations between the stress amplitude and the number of cycles to failure. Note that the linear numerical prediction presented were obtained from multiple data points.

3.3.4 Validations

In order to validate the fatigue damage model, the identified parameters presented in Table 3.1 were applied to the fatigue experiments for UD in alternating load as well as on

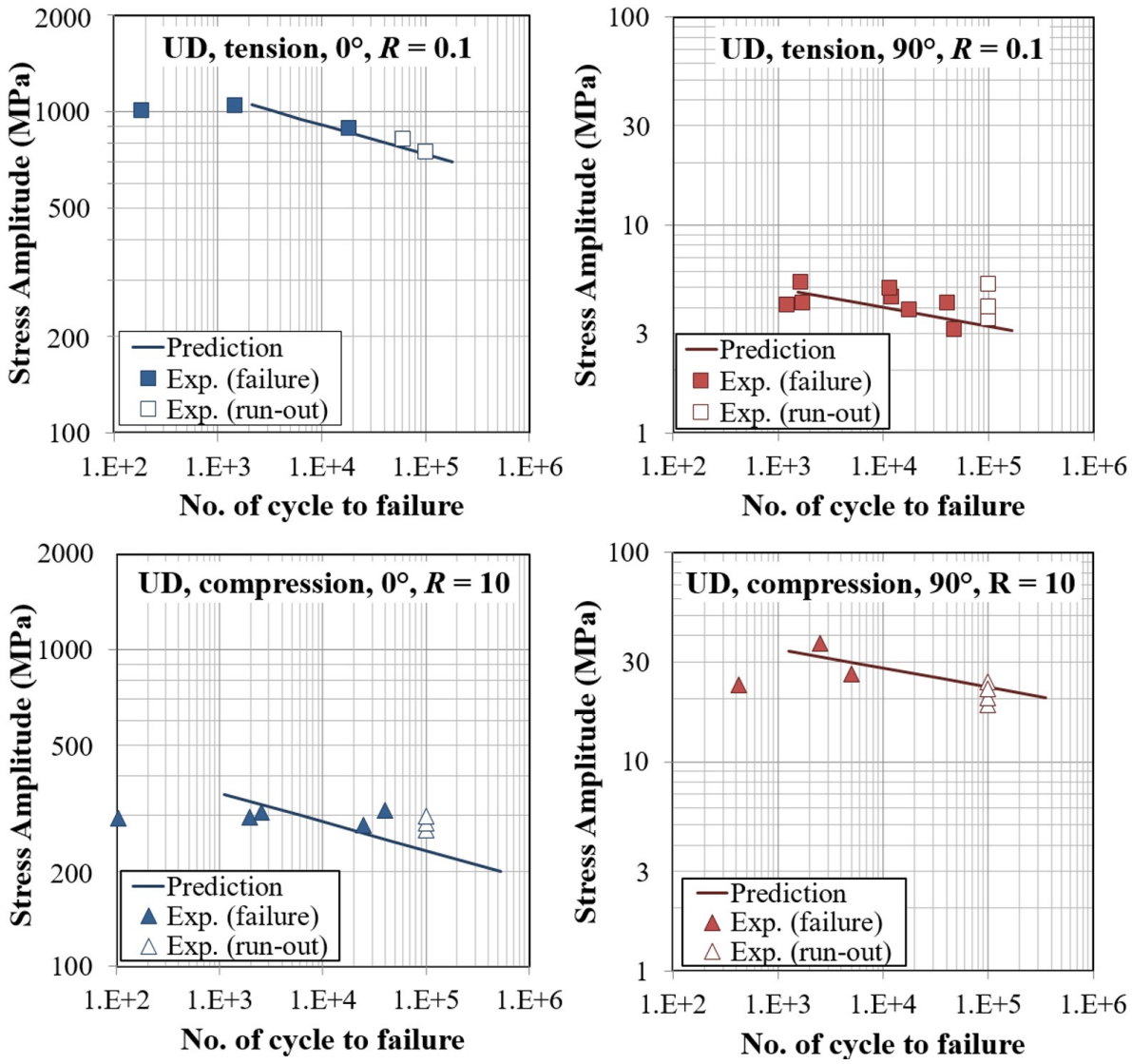

Figure 3.5: Determination of material parameters

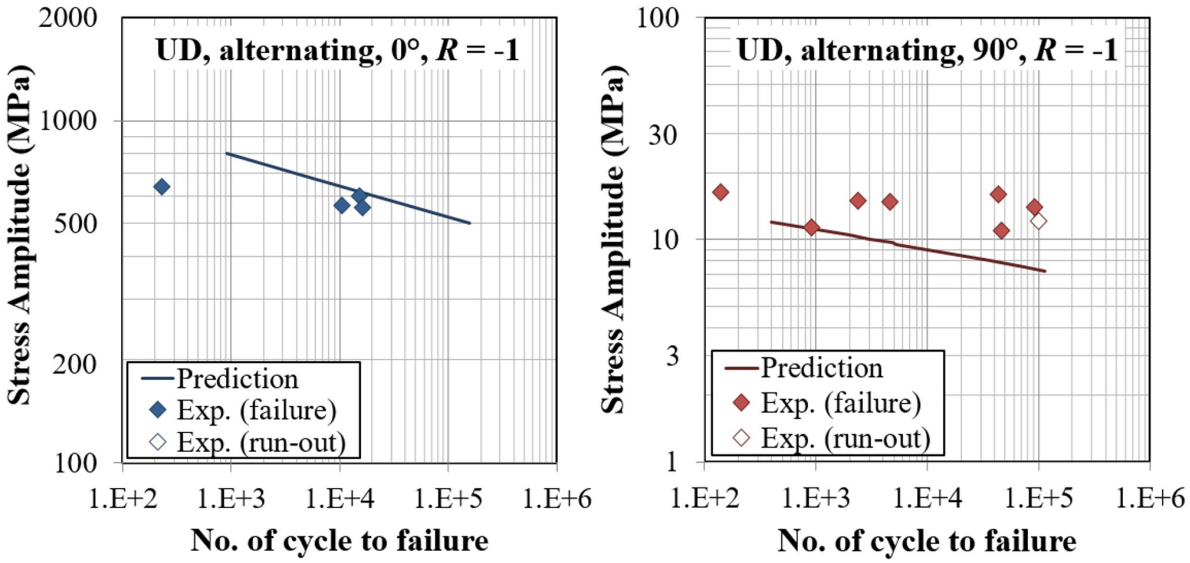

Figure 3.6: Validation on UD alternating load at 0°

MD laminates. The results of numerical prediction over UD alternating load for 0° and 90° are presented in Figure 3.6. As seen in the figures, a linear relationship on double logarithmic S-N curves was obtained for both 0° and 90°. In the case of UD at 0°, the numerical prediction shows an excellent agreement in the case of a higher number of cycles to failure than a lower number of cycles. Meanwhile, for UD at 90°, the numerical predictions are more conservative as all of the data points produced are in the range that matches the experimental lower scatter band.

Regarding specimens of MD laminates, a more complex stress-strain relation can be expected in the individual plies due to the combination of several fibre orientation plies. The interaction between these individual plies of different stiffness orientations and deformation constraints induced by the neighbouring plies create stress states that are no longer uniaxial even when the laminate is exposed to uniaxial loading [60]. In the interest of examining the model's efficacy in such conditions, the fatigue degradation model has also been applied on MD laminates experimental data. Three different stress ratios were compared against the experimental data as displayed in Figure 3.7. Linear S-N curves are obtained for MD numerical prediction similarly to the UD case. The fatigue strength in the case of tensile fatigue load as shown in Figure 3.7 is overestimated in contrast to that under compressive fatigue load. Nevertheless, prediction in both cases remains within the regular spread of experimental data. Lastly, favourable agreement for the low and high number of cycles can be seen in the case of alternating fatigue load.

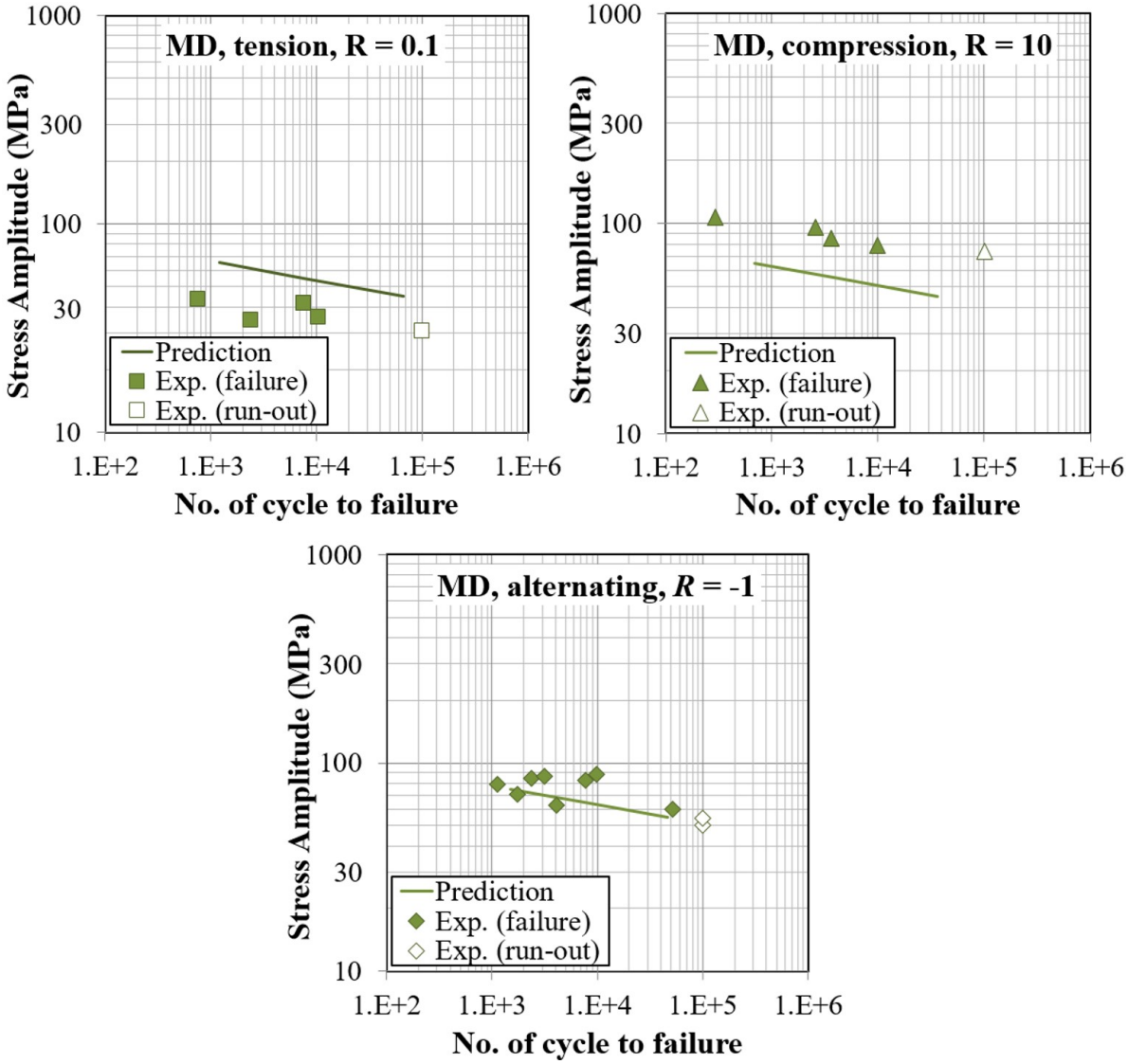

Figure 3.7: Validation on MD for three different stress ratios

3.4 Discussions

There are several advantages of the current fatigue degradation model for CFRP material. Firstly, the absence of independent shear damage variables reduces the number of damage variables required in the model. Here, the independent shear damage variables are replaced by two damage variables that represent microcracks in both planes normal to the respective shear plane. The model's formulation concept based on dissipation of microplastic work within the material presents a physical meaning on how damage evolves in CFRP material. Despite its definition, possible estimation of the microplastic work from the elastic component of stress and strain result renders numerical efficiency implementing the model. The model efficiency is substantial as it requires no actual computation of the microplastic strains. In addition to that, the model yields a linear relationship between stress amplitudes and the number of cycles to failure in double logarithmic S-N curves. This relation can be proven advantageous through simplification of the one-dimensional damage evolution equation presented in Eq. (3.12) by eliminating the influence of the warping function in Figure 3.2. This is done by adopting $\omega(D) = 1$ into Eq. (3.12). As a result, the total increase of damage, where the stress increases from σ_0 to a positive σ_1, is given by

$$\Delta D = \int_{\sigma_0}^{\sigma_1} A\sigma^n \, \mathrm{d}\sigma \tag{3.30}$$

resulting in

$$\Delta D = \frac{A}{n+1}\left(\sigma_1^{n+1} - \sigma_0^{n+1}\right) \quad . \tag{3.31}$$

The accumulation of damage for every stress cycle in the case where a cyclic load with a stress ratio of $R = 0$ is applied is then reduced to

$$\Delta D^{\text{cycle}} = \frac{2A}{n+1}\Delta\sigma^{n+1} \tag{3.32}$$

in which an equivalent damage accumulation for both, loading and unloading part of the cycle is assumed. By inverting Eq. (3.32) and incorporating the accumulation of damage $\Delta D^{\text{cycle}} = 1/N^{\text{fail}}$ per cycle in the case where a material reaches failure after N^{fail} cycles,

$$\Delta\sigma = \left(\frac{n+1}{2A}\right)^{\frac{1}{n+1}} \left(N^{\text{fail}}\right)^{-\frac{1}{n+1}} \tag{3.33}$$

and applying logarithm on both sides of Eq. (3.33),

$$\ln \Delta\sigma = \frac{1}{n+1} \ln\left(\frac{n+1}{2A}\right) - \frac{1}{n+1} \ln N^{\text{fail}} \quad . \tag{3.34}$$

the linear relationship between stress amplitudes and the number of cycles to failure in double logarithmic S-N curves are confirmed. This also substantially supports the concept of microplasticity behind the formulation of Eq. (3.12) based on the assumption of Ramberg-Osgood type power law, linking stresses to the microplastic strains to be beneficial. As a result, somewhat simplified management of material parameters A_{ij} and n_{ij} represents the position as well as the slope of the S-N curve, respectively. Besides that, the model is also shown to be applicable in the case of static failure wherein the material approaches the static strength when the number of cycles is close to one.

Despite successful validation on MD laminates' more complex stress-strain state, the fatigue degradation can be further enhanced. The numerical cost of the fatigue degradation model can be significantly reduced by noticing that in the actual simulations of CFRP materials tested here [3], the only nonlinearity is due to the damage evolution in Eq. (3.25), which is limited to the individual time steps. Thus, Eqs. (3.22) and (3.25) can be decoupled by using the backward Euler numerical differentiation on the latter to get

$$\boldsymbol{D}^{(k+1)} = \boldsymbol{D}^{(k)} + \Delta\boldsymbol{D}(\boldsymbol{\sigma}^{(k)}, \mathbf{D}^{(k)}) \tag{3.35}$$

The damage in the next step $k+1$ can be directly computed from the damage and stress values at the previous step k. Subsequently, this damage can be used to obtain new stresses from Eq. (3.22). Such a slight change in the equations simplifies the numerical procedure since no iterative solution is required, and stress and damage information from the local time point is sufficient. The numerical tests showed that the approximation introduced in Eq. (3.35) is very good, leading to only marginal deviations from the implicit scheme based on the iterative solution of coupled matrix equations, Eqs. (3.22) and (3.25). Therefore, the explicit scheme can be used for the damage accumulation analysis within the CFRP materials. Another aspect of the current model that can be improved is the stress-based split for damage evolution under tensile and compressive loading that is less physical when compared to its counterpart, strain-based. This is because strain-based considers microcrack opening effect when normal strain is positive. The current damage model is also formulated in a stress state that requires local iteration when evaluating the failure criteria, unlike strain state formulation, which employs a direct variable of strain in the standard displacement-based FE method. Another essential downside of the model is the inad-

equate representation of complex stress interactions that are common in describing the failure mechanistic of CFRP material.

Chapter 4

Characterisation of Fatigue on Micro-specimen

4.1 Micromechanical Fatigue Test

4.1.1 Material

The reference composite material that has been used for this study consists of unidirectional carbon fibres with epoxy matrix. Saertex GmbH, Germany supplied the carbon fibre of grade Toray T620 while Sika Deutschland GmbH, Germany, supplied the epoxy matrix of grade Biresin CR170. The manufacturing process to obtain the final material used in the form of a plate starts by producing a dry semi-finished textile product that consists of unidirectional carbon fibres in 0° direction as the main content, together with a few glass fibres oriented in 90° direction, taking into consideration the areal weight compared to one of the carbon fibres. The 90° glass fibres were included to form a bottom layer of the ply to provide connectivity between the semi-finished fibre product with the matrix, prior to and during the matrix infiltration process. The stacked fibres are then sewed together using polyester yarns to form one ply of unidirectional fibres. This ply is then stacked together

Table 4.1: Unidirectional carbon fibre fabric element. [136]

Construction	**Areal-weight** (g/m^2)	**Tolerance** (±%)	**Material**
0°	312	5	Toray T620 50C
90°	9	5	E-Glas 34tex
Powder-Binder	8	± 3	Momentive EPR 05390
Stitching	6	± 1	PES

Table 4.2: Composite resin system. [137]

Physical data	**Resin: Epoxy**	**Hardener: Amine**
Single components	**Biresin CR170**	**Biresin CH150-3**
Viscosity at 25°C (mPas)	13000	20
Density at 25°C (g/cm3)	1.14	0.94
Mixing ratio (in parts by weight)	100	24
Mixture		
Pot life, 100g/RT (min)	60	
Mixed viscosity, 25°C (mPas)	1600	
Mechanical characteristics of the pure resin samples*		
Resin, Biresin CR170 with hardener, Biresin CH150-3		
Shore hardness (-)	ISO 868	D84
Flexural modulus (MPa)	ISO 178	2800
Tensile modulus (MPa)	ISO 527	2700
Flexural strength (MPa)	ISO 178	133
Tensile strength (MPa)	ISO 527	87
Tensile elongation (%)	ISO 527	6.6
Impact strength (kJ/m2)	ISO 179	42
Thermal characteristics of the pure resin samples*		
Resin, Biresin CR170 with hardener, Biresin CH150-3		
Heat resistance (°C)	ISO 75B	139
	ISO 75C	125
Glass transition temperature (°C)	ISO 11357	143

* approximate values after 4h/140°C.

to form 8 layers of unidirectional fibres. The stacked arrangements are fixed together using thermoplastic adhesive spots, placed and fixed into a closed mould, followed by the matrix injection into the mould. This process, called the resin transfer moulding (RTM), allows a continuous matrix to form around the fibre. RTM was performed by Fraunhofer ICT, Pfinztal, Germany [135]. The output material consists of 8 plies of unidirectional carbon fibres in the form of a plate with a plate thickness of 2.4 mm and a fibre volume fraction of 50%. Various raw material components, as well as their mechanical properties involved in this process, are presented in Table 4.1 and 4.2.

4.1.2 Experimental Test Setup

One of the main objectives of this study is to investigate the material behaviour under fatigue loading conditions at the microscopic sub-millimetre scale. A specialised micromechanical setup, shown in Figure 4.1, provides additional advantages that standard testing could not offer, as discussed previously in Section 2.4. This setup is based on Kennerknecht [138] allows a small scale monotonic test such as tensile test [40, 139] and fatigue test to be conducted without any limitation on the tested material. It also can test any material under the frequency ranges that are important to understand the fracture behaviour of the material. Most importantly, the setup allows an in-situ observation on microstructure level during testing to monitor fracture initiation within the material. The setup has been shown to work on micro-fatigue of metallic materials [140–142]. Here, it will be shown that the setup can be used in micro-fatigue tests on composite reference materials.

The setup consists of the following components:

1. prestressed piezoelectric actuator with amplifier modules
2. high load linear DC motor with mercury DC motor controller
3. XY translation stage
4. X-displacement stage
5. load cell
6. telecentric lens
7. machine vision camera
8. LED light source with optical fibre
9. computer
10. other components: pressure regulators, pneumatic cylinders and accessories, camera link frame grabber with Field Programmable Gate Array (FPGA) image processing, individual component adapters

Details on each component specification can be obtained from Table 4.3. The setup can generally be divided into two parts: the fixed part located on the left-hand side of the setup and the movable part on the right side of the setup. The specimen is mounted in between the two parts of the test setup to allow it to be loaded mechanically. The fixed part consists of the XY translation stage, a load cell, and the one-half part of the clamping system. As indicated in Figure 4.1, one XY stage is mounted vertically on the fixed side of the setup in the direction transverse to the loading direction. This is done to allow more effortless adjustment of specimen alignment prior to the test. The movement of this stage

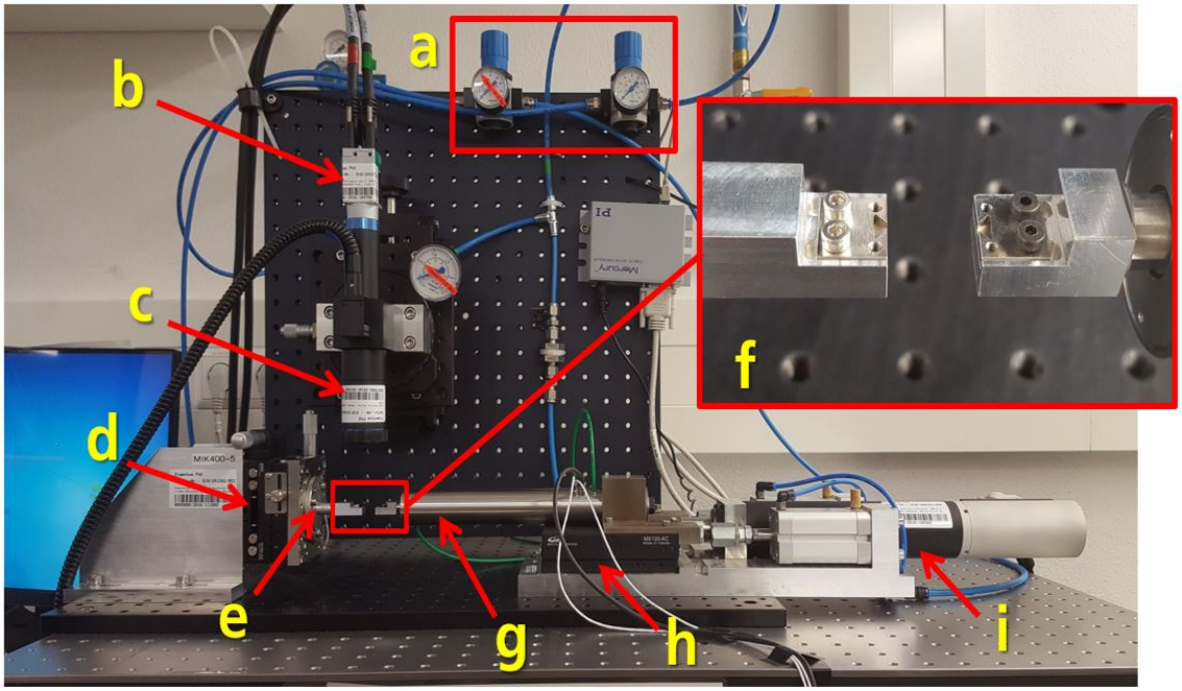

Figure 4.1: Micromechanical setup as built for in-situ observation during experiments (a: pneumatic control, b: camera, c: telecentric lens, d: XY translation stage, e: loadcell, f: clamps, g: piezoelectric actuator, h: X displacement table, i: motor).

can be manually driven in the y-direction and the z-direction by the attached micrometre screws. A load cell connected to the half part of the clamping system is attached to the stage by using a specially manufactured adapter. The load cell functions as a device that measures the load exerted on the specimen throughout the test. The specimen clamp is exclusively machined with high precision detailing the specimen shape (grooves). Such grooves facilitate the specimens to self-align based on the interlocking mechanism of the triangular area in the specimen sections.

The movable part of the setup consists of a piezoelectric actuator, a linear motor and

Table 4.3: Micromechanical setup components details.

Component	Specification	Model/ Company
Piezoelectric actuator	180 µm travel range	Physik Instrumente, Germany
Linear DC motor	50 mm displacement range	Physik Instrumente, Germany
XY translation stage	7G-MXG6-122CE	Vision Lasertechnik, Germany
Load cell	20 N	XFTC300 Measurement Specialties, USA
Telecentric lens	Magnification: 10x Resolution: 1.5 µm WD: 55.2 mm	SOD-10X Moritex Corporation, Japan
Machine vision camera	4 mega pixel	Basler acA2040-180kc RAUSCHER, Germany
LED light source	150 Watt, 5800 K	F3000/PHOTONIC Optics, Austria
FPGA	NI PCIe-7852R	National Instrument, USA

X-displacement stage, and another half part of the clamping system. The piezoelectric actuator produces a linear motion along the x-axis with a relatively low displacement amplitude and high force, suitable for testing under high-frequency conditions. When an additional extension of displacement in the x-direction provided by the piezoelectric actuator is required, the setup is also equipped with a linear motor that provides a high travel range with reduced dynamical capacity. Apart from the linear motor, the travel range of the piezoelectric actuator can also be amplified by the X-displacement stage attached under the piezoelectric actuator. This stage is not directly connected to the linear motor; however, continuous contact between the motor and the stage is ensured by a weak spring inside the stage that causes the motor to push against it. Due to this mechanism, the stage can be separated from the motor when a small load pulling the stage apart is applied. A counterweight with a deflection roller is placed on the table to secure the stage position pushing against the motor continuously. Another part of the setup responsible for continuous specimen surface monitoring comprises a machine vision camera (Basler acA2040-180kc) and a telecentric lens. A combination of both optical devices aids in the uninterrupted observation of the specimen surface prior to the test, during specimen alignment, and optical observation during the test. Lastly, all the components are then connected to a computer. A data acquisition board is installed in the computer to facilitate the exchange of analogue inputs and outputs, along with a Field Programmable Gate Array (FPGA) for image processing done through LabView programming.

Due to its complexity and high precision requirement to ensure the highest measurement accuracy, the setup requires a controlled environment for optimal performance. The whole setup is installed on an optical table to isolate any vibration on the setup. This is because the setup is susceptible to the vibration that might disrupt or even invalidate the tests. The setup is also operated in a climate control environment as an extreme variation of temperatures and humidity would significantly affect the precision range of the setup.

4.1.3 Specimen Preparation

The microscopic scale of the specimen requires a more sophisticated sample preparation process than the standard sample preparation for macro-testing. Previous studies [138, 140–142] have successfully shown the possibility of micro-sample preparation on metallic materials. However, the intricate nature of specimen preparation for composite material for the micro-fatigue test has never been discussed before. This section presents a detailed specimen preparation process that is necessary for micro-testing.

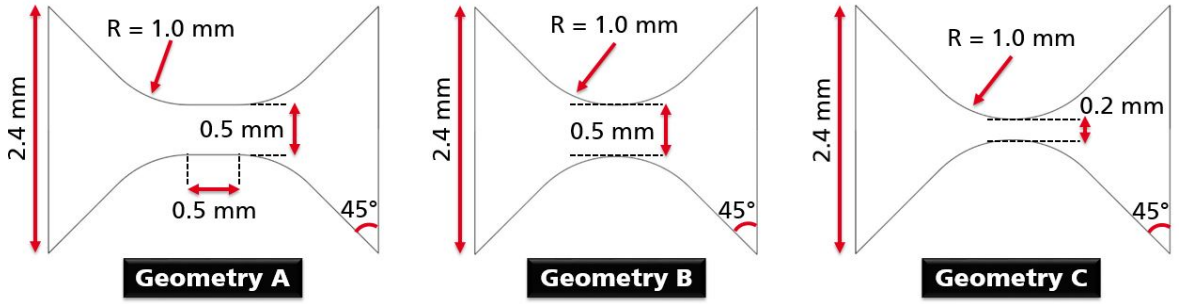

Figure 4.2: Three proposed geometries for micro-specimens, Geometry A, Geometry B and Geometry C.

Selection of final geometry. Before the actual preparation process can be started, the final geometry of the specimen has to be selected. Geometry selection involves stress analysis simulation to look at different stress concentration regions for proposed three hourglass geometries. The main difference in all of these geometries is the dimension of the gauge section. Dimensions for all of the proposed geometries are given in Figure 4.2. This figure shows that Geometry A has the widest gauge section of 0.5 mm while Geometry C has the narrowest gauge section of around 0.2 mm. Geometry C was chosen as the final geometry due to its smallest region within the gauge section capable of ensuring a localised material failure formation. With specimen fracture occurring within a well-defined region, fracture initiation during the test can be easily observed and monitored. Once the final geometry has been chosen, the specimen preparation process begins.

Extraction of small squares from the large plate. There are a total of 5 different fibre orientation specimens extracted from the unidirectional plate that has been considered for the micro-fatigue test, mainly 0°, 30°, 45°, 60° and 90°. The specimen preparation process started with the extraction of several smaller squares with the dimension of 4 cm × 4 cm from a large plate of carbon fibre/epoxy composite as described in Section 4.1.1. These smaller squares can be extracted either by using a slicer or by employing the waterjet cutting technique.

Slicing. The slicer can extract the small squares from the main plate and cut those squares into thin strips to be used in the following process. The procedure of using a slicer starts by fixing the material to be sliced onto the material table inside the slicer with a clamping device as shown in Figure 4.3a and Figure 4.3c. The feeder control for the material table positioning as shown in Figure 4.3d is then adjusted to mark the starting position of the material plate. Next, the hose for the cooling lubricant should be adjusted to provide a direct flow of the lubricant towards the cutting disc during the slicing to ensure that a clean cut can be obtained without damaging the cutting disc or the material. The cutting disc used in this process is the one from Struers model 10S25 as demonstrated in Figure 4.3b.

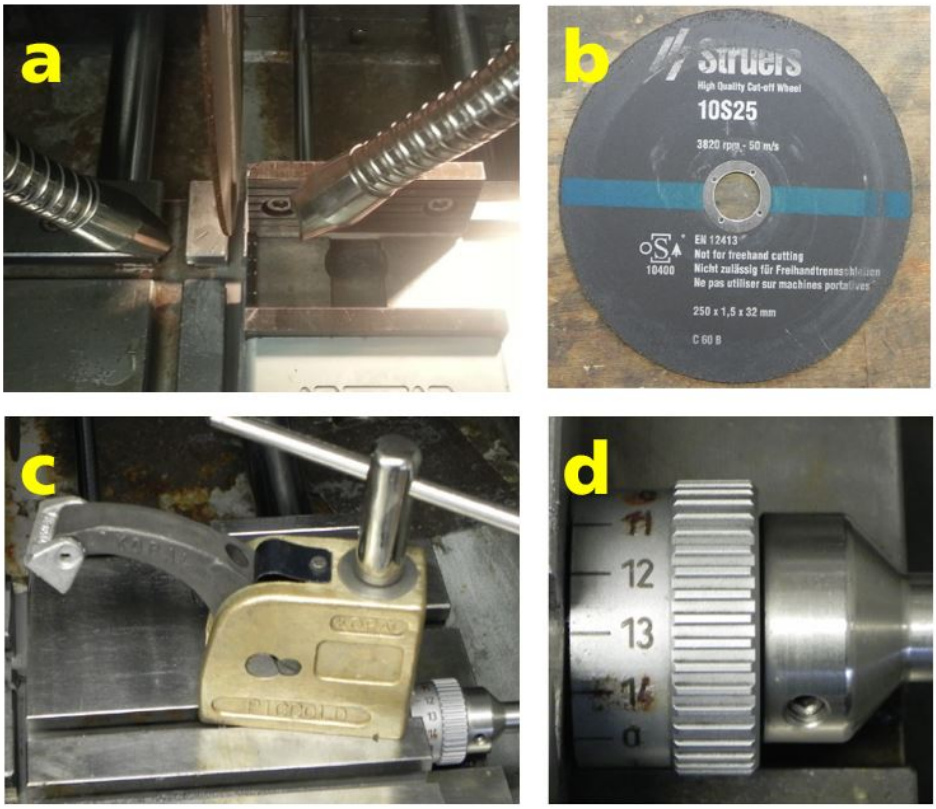

Figure 4.3: Slicing of material into 1 mm thickness thin strips (a: Square plate placement during slicing with cooling lubricant hose directed towards the cutting disc, b: Cutting disc used for slicing, c: Clamping device, d: Feeder control for material table positioning).

Once every component is in place, the safety cover of the slicer is secured. The slicer is set by inputting the rotation of the cutting speed to 1300 rpm before the slicing process starts. The slicing runs automatically and stops once the disc finishes cutting the whole strip. Once the whole strip is completed, the safety cover of the slicer is removed to adjust the feeder controller by 25-27 marks to have enough material for the next strip. The whole process is repeated until the whole square plate has been cut into strips of roughly 1 mm thickness. Some of these thin strips sometimes contain burr that usually forms on the edge of the strips. The burr can be removed carefully using a razor blade to obtain thin strips with clean and smooth edges. Ensuring that the strip edge is clean and smooth is essential for the following process in specimen preparation.

Gluing. Before grinding or polishing the thin strips can begin, the thin strip needs to be attached to the sample holder. The strip is attached to the sample holder by applying a small amount of cyanoacrylate (CA) glue on both ends of the strip to secure its place on the sample holder. In order to ensure easy removal of the thin strip from the sample holder in the later process, a thin adhesive tape is applied to cover the surface of the strip before gluing. The thin strip set on the sample holder is then placed under a compressive

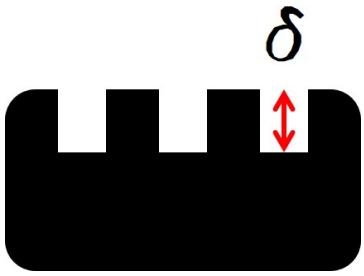

Figure 4.4: Sample holder notch depth, δ = 0.6 mm, 0.2 mm and 0.1 mm.

device that presses the thin strip to adhere to the sample holder continuously for about 15 minutes under the pressure of 4 bars. The process is repeated until the sample holder is filled. The same gluing step has been used for each step in the specimen preparation process that requires gluing the strips onto the sample holder. The strips after gluing to the sample holder can be referred to in Figure 4.5a. There are three different sample holders with three different notch depths of 0.6 mm, 0.2 mm and 0.1 mm as illustrated in Figure 4.4. The sample holders were designed to have different notch depths to control the thickness of the thin material strips for each step of the process. The final sample thickness required for the testing is approximately 150µm.

One of the main setbacks in the specimen preparation process involves attaching and detaching the material strips onto sample holders. This process causes a lot of material strips to break into pieces, especially strips that are used for off-axis specimens. Material strips for off-axis specimens are more brittle in nature compared to longitudinal specimens. Due to this reason, detaching the strips is one of the processes where the loss of material often happens. To minimise material loss, a layer of adhesive tape to cover the surface of the strip that will be glued onto the sample holder is applied, as mentioned previously. This is particularly helpful for off-axis material strips rather than longitudinal strips. However, the layer of adhesive tape needs to be replaced every time the strip needs to be attached to another sample holder. Since the strip is now covered with adhesive tape and not glued directly onto the sample holder, this unfortunately also increases the risk of the strip detaching during grinding and polishing. Therefore, it is important to ensure that the surface of the strip is first clean before applying the adhesive tape layer and glued to the sample holder. A soft rubber eraser is sometimes used to remove a slight glue stain from the previous adhesive tape that remains on the strip. It is important to note that this must be done gingerly to avoid introducing any scratches on the polished surface of the strip or even breaking the thin strip.

Grinding. After the thin strips were attached to the sample holder using CA glue, the grinding and polishing processes were done on the material following three different stages using Struers Tegamin 30 grinding and polishing machine. There are four steps of grinding involved whereby four different grit sandpaper were used: 320, 600, 1200 and 2500 µm. A 6-way perforated sample mover plate, as shown in Figure 4.5b, is best for this process. The contact force for each stage of the grinding process is set to be at 5 N. The sample mover plate rotation and the turning table rotation are maintained at 150 (1/min). The first grinding process starts with the material strips attached to the 0.6 mm sample holder. This step aims to obtain material strips with uniform thickness. Next, the material strips are transferred to a 0.2 mm sample holder to remove more material from the strip and get a thinner strip.

Polishing. Finally, the strips are transferred to the 0.1 mm sample holder to smoothen out the surfaces and the last stage of polishing. Regarding polishing, there are two steps of polishing required to obtain the final surface quality required. The first cycle of polishing involves 9µ polishing mat of Texmet followed by 3µ with MD-DAC polishing mat as displayed in Figure 4.5c and Figure 4.5d. It is also important to accompany the polishing process with the diamond suspension to ensure the best quality of the polished surface. The contact force between the specimen and the polishing plate is between 25-30 N. The same

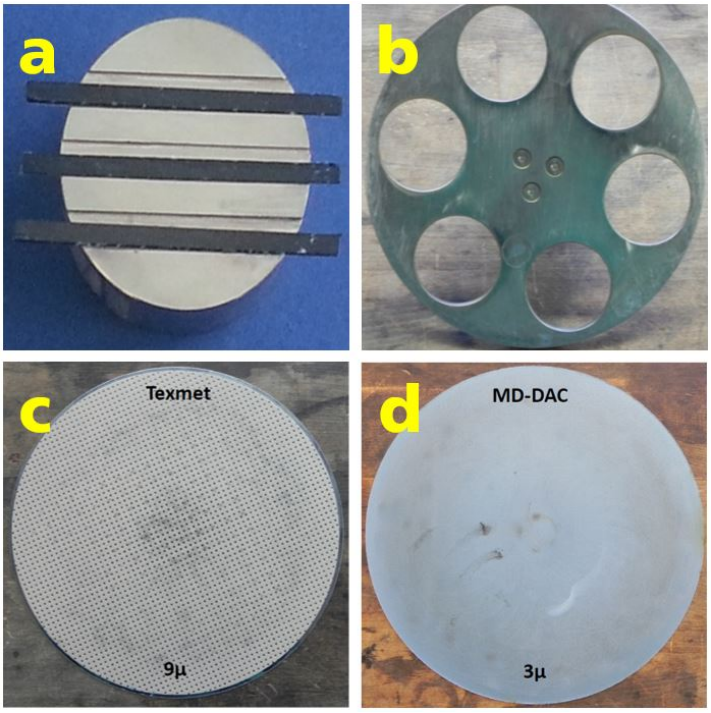

Figure 4.5: Grinding and polishing step in specimen preparation process (a: Material strips attached to the sample holder, b: 6-way perforated sample mover plate, c: 9µ Texmet polishing mat, d: 3µ MD-DAC polishing mat).

Table 4.4: Summary of settings required for grinding and polishing process.

Process	Sequence	Contact Force (N)	Rotation (1/min)		Rotation Direction
			Sample Mover Plate	Turning Table	
Grinding	# 320 # 600 # 1200 # 2500	5	150	150	Same
Polishing	9µ 3µ	25-30	150	150	Opposite

sample mover plate and turning table rotation as in the grinding process is maintained, except that the direction of the rotation is now opposite. During the polishing stage, both sides of the material strip surfaces were constantly monitored to ensure that the best quality images of the sample could be obtained during testing. Figure 4.6 shows the difference in the material surface microstructure before and after polishing.

The grinding and polishing process was done on both sides of the strip surfaces until the final strip thickness reached approximately 150µm. Extreme attention is required to preserve these surfaces throughout the whole process. The surface quality is continuously monitored and inspected under a microscope to ensure that none of the surfaces is damaged. If the specimen surface is badly damaged, the specimen has to be discarded from testing. The summary of the settings required for the grinding and polishing process involved can be summarised in Table 4.4.

Maintaining the balance of the individual sample holders with material strips attached is one of the critical issues during this process. Even a slight imbalance causes the strips to have non-uniform thickness resembling a long wedge-like cross-section. The whole material strip has to be discarded in this case as the specimen extracted from this strip has a wide variation in thickness and will no longer be valid for testing. A straightforward solution to this is to ensure that the number of glued strips on the sample holder does not

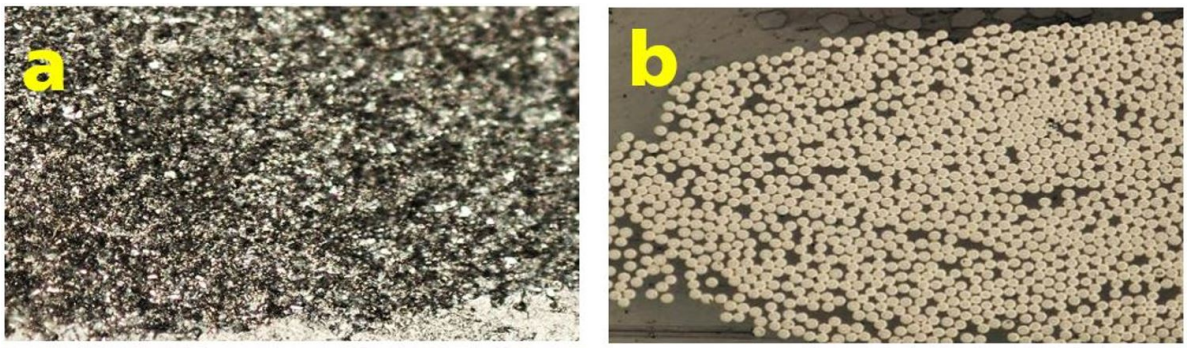

Figure 4.6: Surface polish quality (a: Before polish, b: After polish).

cause the sample holder's imbalance. This is accomplished by making sure that either two notches of the sample holder are used to attach the strip with one middle notch left empty, or all three of these notches are fully utilised simultaneously. The latter is the most preferred alternative as this will allow three strips to be ground and polished simultaneously for every sample holder. At the same time, the individual sample holder balancing can be maintained to ensure that the final polished strips are of the best quality for specimen extraction.

Additionally, the assembly balancing for grinding and polishing should also be considered to produce the best results. Usually, grinding and polishing are done using either a minimum of three sample holders or six sample holders simultaneously. When only three sample holders are used, each sample holder needs to be positioned at an equal distance to each other when using the 6-way perforated sample mover plate attached to the grinding and polishing machine. This can be achieved by placing the sample holder with one empty slot apart from each other to maintain the whole assembly's balance. If there are less than three sample holders available, a cured mounting resin of similar weight that is usually used for metallographic purposes may be utilised as the sample holder replacement to maintain the balance. Nevertheless, the preferred alternative is to fully occupy the slots in the 6-way perforated sample mover plate to avoid this problem.

Another common problem that could lead to material waste during this process is when the strip is detached from the sample holder while grinding or polishing. The detached strip that is still thick will usually be able to be reused. However, when the strip is detached during the final stage of grinding or during polishing, the strip will often break into pieces due to its brittle and fragile nature. Unless the middle strip is detached, the balancing of this sample holder needs to be adjusted before further steps can be continued. A typical cause of detachment of strip during these processes is due to remaining deposits on the notches that have not been adequately removed before the gluing stage. These deposits that clog the tight notch, especially at the notched corner, reduce the surface area of the strip that is directly adhered to the sample holder, creating a weak bond between the strip to the sample holder. These deposits can be removed by applying a few drops of cleaning agent into the sample holder notches with lightly scouring the tight corner using a metal tip. The usual cleaning agents used in this step are ethanol or acetone. Afterwards, the sample holder is placed in a beaker containing the same cleaning agent used in the previous step. The whole beaker is placed inside the ultrasonic bath for about 15 minutes to thoroughly remove all types of dirt or deposits that remain on the sample holder. Before the sample holder can be used, the final step is to dry the sample holder thoroughly.

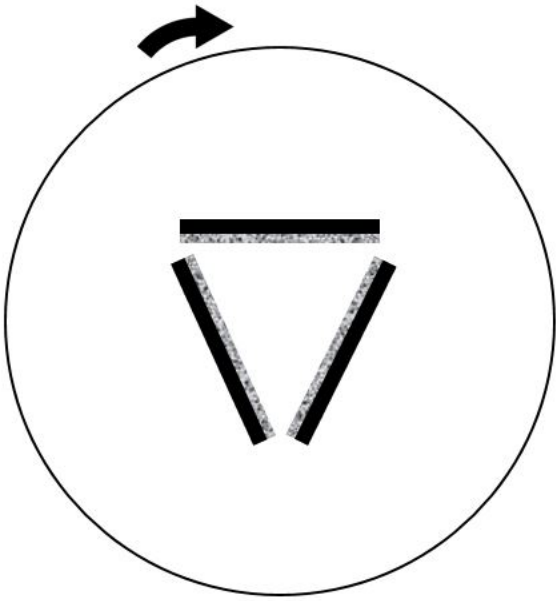

Figure 4.7: Arrangement of pressing plates on a sample mover plate without hole. Pressing plates edge with groove (represented as dotted filled region) is positioned inward towards the centre of sample mover plate.

These cleaning steps are repeated every time the sample holder is used again throughout specimen preparation.

Fixture pressing plates. A supplementary routine to smoothen the pressing plates has been developed to eliminate friction between the pressing plate with the strip top surface. The first step is to attach the pressing plates to a sample mover plate without a hole using double-sided tape. Only one surface of the pressing plate (the surface that presses the top strip surface) must be smoothened for this process. All three pressing plates can be ground and polished at the same time. The plates are arranged centrally whereby the edge with the geometry groove is positioned facing inward towards the centre of the sample mover plate, forming an open triangular shape as shown in Figure 4.7. The arrangement of the pressing plates is essential to minimise distortion damage to the geometry form on the plates due to centrifugal force and the accumulation of dirt during the operation. Besides that, the placement of the plates must form an open triangular to have enough spacing between one plate to another to facilitate the flow of the lubricant carrying all the ground material particles from accumulating in the centre region, possibly scratching the surface further. Once the plates have been attached to the sample mover plate, it is now ready for grinding. Unlike the grinding process done to prepare the material strips, there is only one grinding step required in this case (grind paper sequence #1200). The contact force necessary for the plates is 30 N with both sample mover plates and turning table, rotation direction to be the same at 150 (1/min). The plates are ground for about one minute or until the

entire surfaces are equally even. Once this is achieved, the plates are then removed from the sample mover plate and cleaned using ethanol. The plate is then thoroughly dried and re-attached to the sample mover plate using a new double-sided tape in the same manner as earlier for further steps. The next step is to polish the surface of the plates accompanied by the diamond suspension. This is done by following two polishing steps, 9µ Texmet polishing mat followed by 3µ MD-DAC polishing mat as shown in Figure 4.5c and d. The contact force of 30 N is maintained for both stages. The other settings are similar to that of polishing done on the material strip as presented in Table 4.4. After every step of grind and polish, the tape used to adhere the plates onto the sample mover plate will have to be replaced, and the pressing plates have to be thoroughly cleaned by using ethanol. This is important to prevent any material particles removed from the plate during the earlier step, scratching the plate surfaces during the more delicate step afterwards.

Milling. After the material strips and the fixture pressing plates are polished, the strips are now ready to be machined into the final hourglass geometry required for testing. In order to have a precise geometry of the specimen, the polished strips are fixed onto a specialised milling fixture as shown in Figure 4.8c by using CA glue. A pressing plate is then placed on top of each attached strip. A total of three pressing plates are required for one fixture, and these plates are then fastened in place with several pins and screws. It is important to make sure that the surface of the pressing plate touching the strips is cleaned and polished well so that the vibration from the milling process later does not further scratch and damage the polished strip surface. The primary process used in this stage of specimen preparation is CNC milling, and this process has been chosen for the case of 30°, 45°, 60° and 90° fibre orientation specimens. In order to get a good quality of samples from the milling process, the optimum milling parameters and the suitable type of mill-head need to be determined. After several trials to improve the quality of samples from the milling process, the best results for 30°, 45°, 60° and 90° fibre orientation specimens were obtained by using the diamond-coated mill-head with a cutting speed of 5,000 rpm and feed rate of 50 mm/min. Several batches of these samples were then given to the Fraunhofer IWM Workshop to be milled. An average of two specimens can be obtained from one strip of polished material. An alternative method is required to get the final geometry out of 0° fibre orientation specimens. This is due to the difficulty of attaining smooth and clean edges from the cut carbon fibre. The specimens with longitudinal fibre direction (0°) were severely damaged from the milling and therefore cut using the waterjet cutting method.

Waterjet cutting. The alternative considered for this purpose is the waterjet cutting method. This method was chosen based on its advantages on polymer materials. A separate

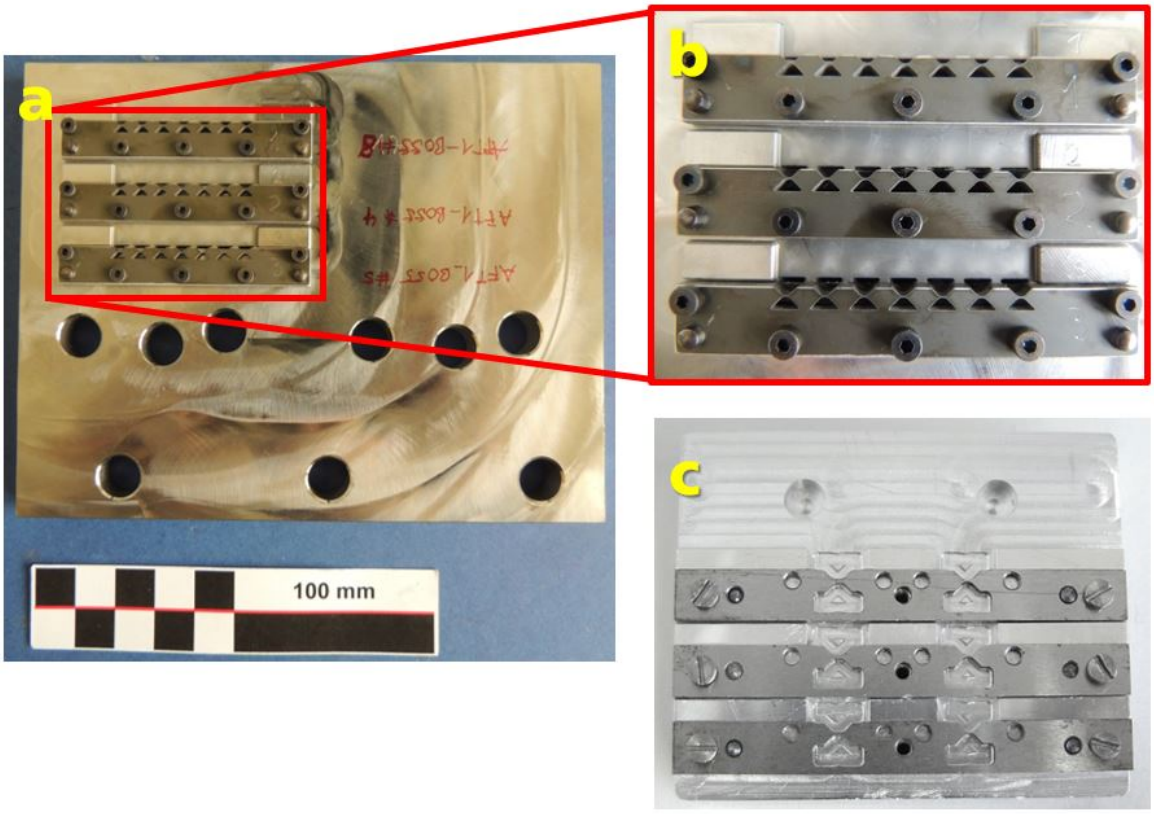

Figure 4.8: Specialised fixture used in milling and waterjet cutting (a: Overall waterjet cutting fixture, b: Geometry forms on waterjet cutting fixture, c: Milling fixture).

specialised fixture is designed and used for this process (see Figure 4.8a). A maximum of seven specimens can be extracted from one strip of polished material using waterjet cutting as displayed in Figure 4.8b. However, not all specimens are accepted for testing due to the slight thickness variation throughout the material strips that arise from the specimen preparation process. This issue will be discussed further in Section 4.3.5.

Extraction of the specimen from the fixture. Once the polished strips have been milled and cut, specimens in the form of the chosen final geometry can be extracted from each fixture. The specimen is extracted from the fixture carefully using a surgery-grade scalpel to ensure that the geometry and both sides of the surfaces are not scratched or damaged. Since the material is brittle, the specimen is easily damaged at this process stage. An average of 50% of the specimen broke; therefore, much attention is required in this process. A summary of the specimen preparation process can be illustrated in Figure 4.9.

Measurement of final dimension. The last step in specimen preparation is the final dimensions of each of the specimens using optical microscopy. Therefore, the specimen is attached to a customised specimen holder designed to ease the process of specimen rotation so that a clear view of each specimen side can be obtained. Pictures from each side of

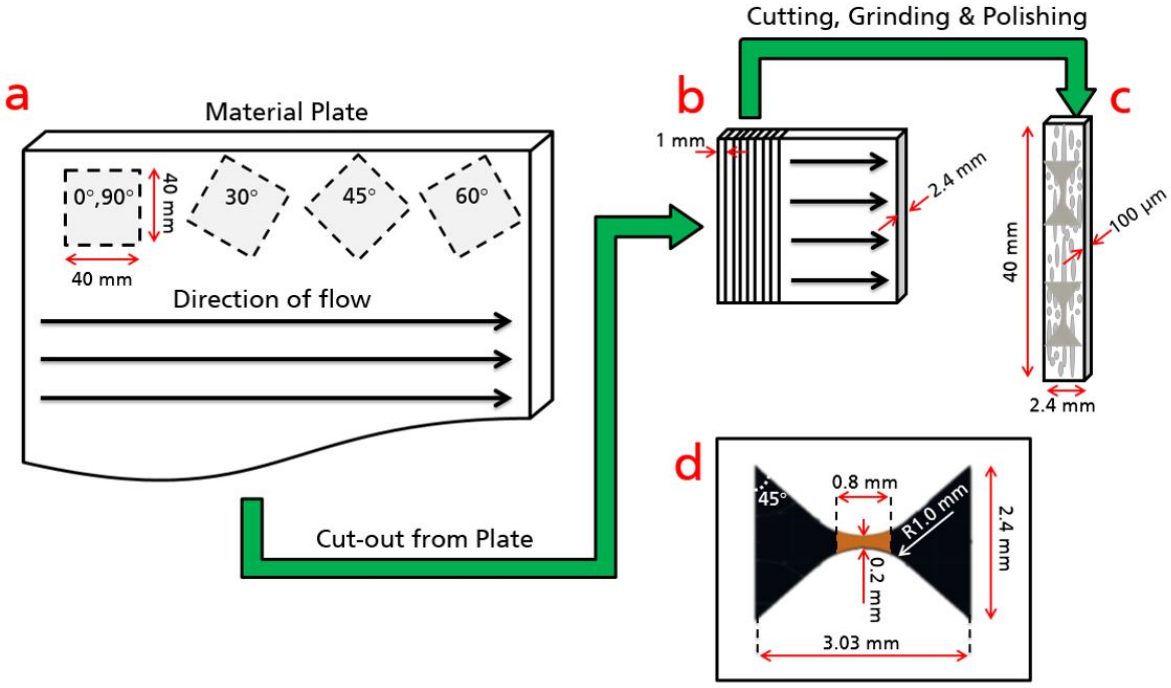

Figure 4.9: Brief summary of specimen preparation process (a: Firstly, square plates are cut from the material plate, b: Secondly, the square is then sliced into thin strips, c: Both side of the strip surfaces are ground and polished until required thickness, d: Final geometry of the specimen after milling/waterjet cutting process).

the specimen are taken using an appropriate magnification objective to maximise the view on the top and bottom edge of the specimen. There are four sides of the picture required to complete the measurement of the specimen, namely the top, bottom, right and left sides of the specimen. This allows an effective area where the applied load acted on can be determined. Several pictures should be taken for each side of the specimen by using the bright field and dark field setting for a possibility to measure the average from several measurements later. These pictures were then analysed by using the ImageJ application. The width of the gauge section is measured from several pictures taken from the top and bottom surfaces of the specimen. The specimen thickness can be obtained from the measurements of the right and left sides of the specimens. The measurements in pixels obtained for the width of the gauge section as well as the thickness are then divided by the calibration factor of the magnification objective used to get the actual length as presented in Eq. (4.1). After the measurement is complete, the specimen is ready for the micro-fatigue test.

$$\text{Actual length in } \mu\text{m} = \frac{\text{measurement in pixel}}{\text{objective calibration factor}} \tag{4.1}$$

4.1.4 Micro-Fatigue Test

To investigate the effect of fibre orientation under fatigue load, a tension-tension cyclic fatigue test was conducted under force-controlled conditions on five different fibre orientation micro-specimens of 0°, 30°, 45°, 60° and 90°. Around 10-20 specimens were tested for each condition at different stress amplitudes and constant stress ratios ($R = 0.1$). (R is defined as the ratio between the minimum and the maximum stress in the load cycle, i.e.,

$$R \equiv \frac{\min\{\sigma(t)\}}{\max\{\sigma(t)\}}\,. \tag{4.2}$$

The micro-fatigue test was carried out by using the micro-test setup introduced in Section 4.1.2 using only a piezoelectric actuator. The test was conducted under sinusoidal loading at a frequency of 10 Hz at room temperature and 53% humidity. Several necessary steps are required exclusively concerning the use of the micro-test setup. A brief micro-fatigue test procedure is explained below. In detail, a step-by-step procedure can be found in Appendix A and in-depth technical information on the control parameters of the test setup can be obtained from Kennerknecht [138].

Preparing the setup. The first step is to ensure that both half parts of the clamping system (where the specimens will be placed later) are aligned correctly and at the same height. The right side of the clamp attached to the piezoelectric actuator and motor is treated as the reference, whereas the left side of the clamp is then adjusted to match the height and the alignment of the right side clamp. Establishing horizontal and vertical alignment is vital to ensure the validity of the load applied to the specimen during the test. Due to the material's brittleness, cushioning on the bottom of the specimen is required to compensate for the slight specimen movement later when the clamp is tightened. An aluminium plate of thickness 0.2 mm in the shape of triangular grooves of the clamp is then placed inside each side of the clamp groove for cushioning purposes.

Setting preload conditions. The specimen is then placed in the triangular groove of the clamp. Preload is then applied to the specimen through the movement of the motor at a velocity of 0.001 mm/s. The preload value is minimal not to induce premature damage on the specimen while it helps the specimen self-align itself within the clamp. It is crucial to ensure that the specimen is straight. The first specimen picture under preload is then saved as a reference for in-situ observation of the specimen throughout the test. Another aluminium plate of 0.1 mm thickness is placed in each triangular groove on each side of the clamp. The thin aluminium plate act as the top cushion for the specimen. Once the aluminium plates are placed, the grips are fixed and tightened carefully to secure the spe-

cimen.

Setting actual test conditions. Once the preloading stage is completed and the specimen grip is secured, all necessary load parameters are entered into the Labview program to start the test. Due to the brittle nature of the specimen and its size, the specimen is more sensitive and prone to breaking. Extreme care is required while handling the specimen and load application setting. Therefore, several control parameters are necessary to limit the fluctuation response of the specimen under applied sinusoidal load so that the specimen response stays within the target range. Apart from the parameters to control the instability response of the specimen, data acquisition parameters are essential to ensure that complete data throughout the entire spectrum of loading are captured ultimately, especially when the test involves a vast number of cycles. More information on the required parameters can be obtained from Appendix A. The motor is then set to move until the stress applied to the specimen reaches the mean stress. Both displacements, by motor and piezoelectric actuator, are recorded. This option is particularly important when the tested specimen requires large deformation where both piezoelectric actuator and motor are required to assign necessary displacement to match the assigned load. However, this is an optional step for the current micro-fatigue test since the force will only be applied through piezoelectric actuator displacement. This is possible because the specimens tested in this micro-fatigue test do not require large deformation. Therefore, the travel range of the piezoelectric actuator is sufficient, and the motor is no longer necessary. A picture of the specimen's front surface under preload at this stage should be captured. The appropriate image size can minimise memory allocation for picture storage throughout the test. Periodic images stored throughout the test are taken from the Labview photo software, with the frequency of the images taken are set to be 1 picture/min. The final step to this stage is applying the specimen's load.

Adjustment during the test. Once the sinusoidal load is applied to the specimen, the parameters that control the fluctuation response of the specimen need to be tightened gradually to ensure no abrupt changes that may induce premature damage to the specimen were introduced. The accounted number of cycles starts once the whole system is stabilised.

End of the test. Once the specimen is broken, the test is completed. A picture of the broken specimen is saved before the broken specimen is removed from the clamps. All of the recorded data are analysed. Only load cycles that fall within the acceptable criteria requirement range are considered the actual number of cycles. The accepted stability threshold in this thesis is defined to be between 8 to 10 % from the target stress amplitude.

Fracture surface analysis. The broken specimens tested in the micro-fatigue test were analysed using the Scanning Electron Microscope (SEM) to study the fracture mechanism on the specimens' fracture surface. One-half of the broken specimens are first coated before the specimen is ready for the SEM process. The coating is necessary to improve the specimen's imaging quality under SEM. There are several types of specimen coating available for SEM. Here, a sputter coating was chosen for the fracture analysis of all micro-fatigue test specimens. An ultra-thin conductive layer of metal (coating thickness of roughly 2 nm) is created on the fracture surface. The model of the SEM device used for the fracture surface analysis is Hitachi S-3400N. The accelerating voltage is 5,000 V with an emission current between 53 k and 67 knA.

4.2 Results

This section presents the results obtained from the micro-fatigue test on the composite material, including the fracture surface analysis on the broken micro-fatigue test specimens. The in-situ observation of failure initiation on the specimen during the test and the fracture surface analysis of the broken specimens are of utmost importance for investigating the microscopic phenomena occurring in the composite material that otherwise could not be observed in a standard experimental setting [66]. There are three main categories of results obtained throughout the test. The first section focuses on the performance of the micro-specimens under fatigue load from the presented S-N curves. The second part of this section helps understand the on-set of micro-cracks within the material and how the crack progresses until failure. Finally, the last section provides information on the possible failure mechanisms detected on the fracture surface of broken micro-fatigue test specimens.

4.2.1 S-N Curves

The performance of the specimens tested in the micro-fatigue test can be presented as S-N curves as shown in Figure 4.10. There are five separate S-N curves with respect to the five tested fibre orientations, which are 0°, 30°, 45°, 60° and 90°. The micro-fatigue test was performed on various stress amplitudes under a frequency of 10 Hz with a stress ratio $R = 0.1$. The data collected in these S-N curves fulfil the following validity criteria:

- Only specimens that are fatigue tested until failure are included
- All specimens with premature cracking before the test started are discarded
- Only specimens that exhibit stable response throughout the entire test are accepted. The acceptance stability threshold is here defined to be between 8 to 10 % from the

Table 4.5: Micro-fatigue test S-N curves details.

Orientation	0°	30°	45°	60°	90°
Gradient (MPa/cycles)	-0.2056	-0.0463	-0.0112	-0.0089	-0.0094
Intercept (MPa)	1555.5	48.8	28.2	28.3	23.0
RMSE	0.1513	0.1112	0.0345	0.0579	0.0583
No. of test	16	21	24	16	14
No. of valid test	7	18	9	8	7
Accepted tests (%)	44	86	38	50	50

target stress amplitude.

All of the fatigue results are presented in S-N curves with 50%, 5% and 95% quantile representation similarly as presented in Section 3.3.2. The 0° specimens stress amplitudes from the S-N curve data (Figure 4.10) range between 80 MPa to 225 MPa, which is the highest among all other tested fibre orientations. The specimen tested at 80 MPa failed after about 349,000 cycles, while the one tested at the highest stress amplitudes failed after about 50,000 cycles. One 30° specimen lasted the longest, around 2,500,000 cycles before failing (approximately 69 hours), while the shortest is a 45° specimen at about 200 cycles (approximately 20 seconds). The summary of findings for all of the S-N curves is presented in Table 4.5. The slope of the S-N curve for specimens with fibre orientation of 30° and above are close to zero. In contrast, in the case of 0° fibre orientation specimens, the slope is significantly larger at -0.2056 MPa/cycles. Apart from having the biggest gradient compared to all other orientation specimens, 0° specimen also show the highest intercept value (extrapolated value at 0 cycle) from the linear relationship in double logarithmic scale between stress amplitudes and the number of cycle to failure. 30° fibre orientation specimens show the second-highest intercept of stress amplitude at about 48.8 MPa. Interestingly, the intercept value for 45° and 60° fibre orientation specimens is around 28 MPa, while 90° specimens have the lowest intercept at 23 MPa. The root mean square error (RMSE) for each fibre orientation has been evaluated based on Eq. (4.3).

$$\text{RMSE} = \sqrt{\frac{\sum_{i=1}^{N} \left(\log \sigma_i - \log \hat{\sigma}_i\right)^2}{N}} \tag{4.3}$$

In this equation, σ_i is the measured stress amplitude, $\hat{\sigma}_i$ is the predicted stress amplitude obtained from Eq. (3.27), and N is the number of tests. The RMSE value for 0° orientation specimens is the largest compared to off-axis specimens except for the case of 30° fibre orientation specimens. Both 0° and 30° orientation specimens have similar RMSE values of 0.1513 and 0.1112, respectively, while 45° orientation specimens have the smallest value at 0.0345. 60° and 90° orientation specimens also have a similar RMSE value of 0.058. Based

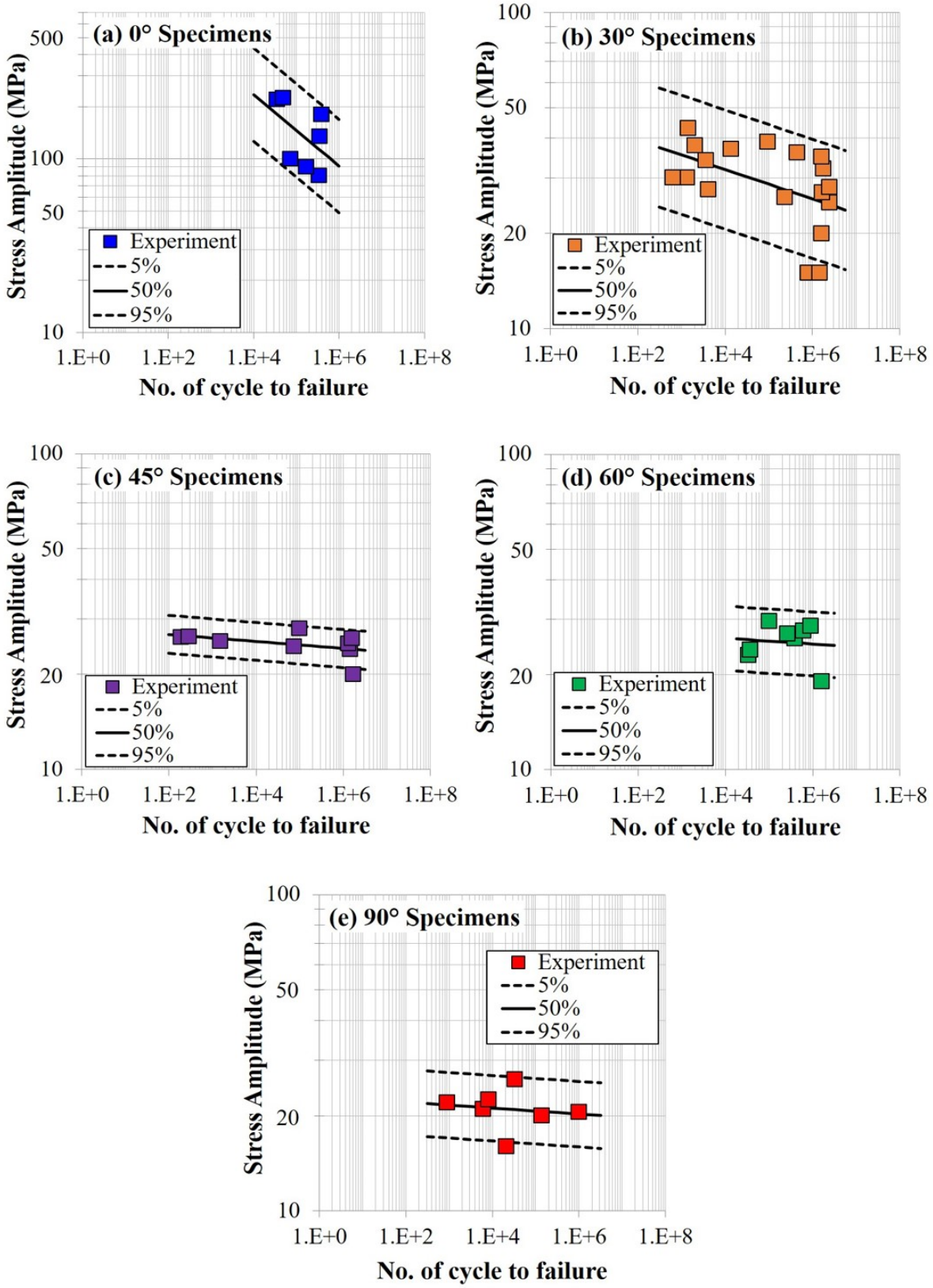

Figure 4.10: S-N curves for all five test orientations

on the validity criteria mentioned earlier, the lowest percentage of accepted tests can be seen for specimens of 45° fibre orientation with only 38%, followed by 0° specimens with 44%. 60° and 90° fibre orientation specimens have the same percentage of accepted tests while 30° fibre orientation specimens have the highest percentage of 86%.

4.2.2 In-situ Observations of Failure Initiation

The attachment of the telecentric lens to the custom-built micro-fatigue setup allows an in-situ observation of failure initiation occurring within the specimen during the micro-fatigue test. This, in particular, is important to help us understand the on-set failure behaviour on a microscopic scale. Some specimens presented in this section are not included in the S-N diagram (Figure 4.10) due to the criteria mentioned in the previous section. However, these specimens' on-set of crack initiation is still valuable and will be included. From the results of recorded pictures taken every 1 minute throughout the test, some of the specimens exhibit a single failure mechanism observable during the test. In contrast, others show multiple failure mechanisms, with one failure mechanism in particular acts as the dominant failure mechanism that causes complete loss in the load-carrying capacity of the specimen. Some of these failure mechanisms seem to be shared by all fibre orientation specimens, while others fall in the orientation-specific failure mechanism category.

One example of orientation-specific failure mechanism observed only on 0° specimens is delamination, as illustrated in Figure 4.11. Figure 4.11a shows the specimen at the beginning of the test. Due to the difficulties in the specimen manufacturing process, it can be seen that the specimen have slightly rough edges contributed by the cut fibres, especially at the curvature side of the specimen. The cutting process also contributed to the delamination in two places before the test starts, as indicated by the arrow in the same figure. No other failure in the specimen was observed until about 39,000 cycles, where a separation between fibres and matrix can be observed at the lower right side of the specimen, as highlighted in the red dashed box in Figure 4.11b. This separation significantly progresses by the time the specimen reaches 44,000 cycles in Figure 4.11c. Although substantial delamination can be observed, the specimen continues to carry the load applied for another 342,000 cycles before failing at 385,859 cycles as shown in Figure 4.11d. The two earlier regions with delamination due to manufacturing defects (indicated by the two top arrows) can be seen to progress in this figure. However, the delamination that develops during the test at the lower side of the specimen becomes the dominant failure that causes the whole specimen to fail.

Another failure mechanism observed on 0° specimen is depicted in Figure 4.12. Figure 4.12a shows the specimen before the test started, while Figure 4.12b depicts matrix

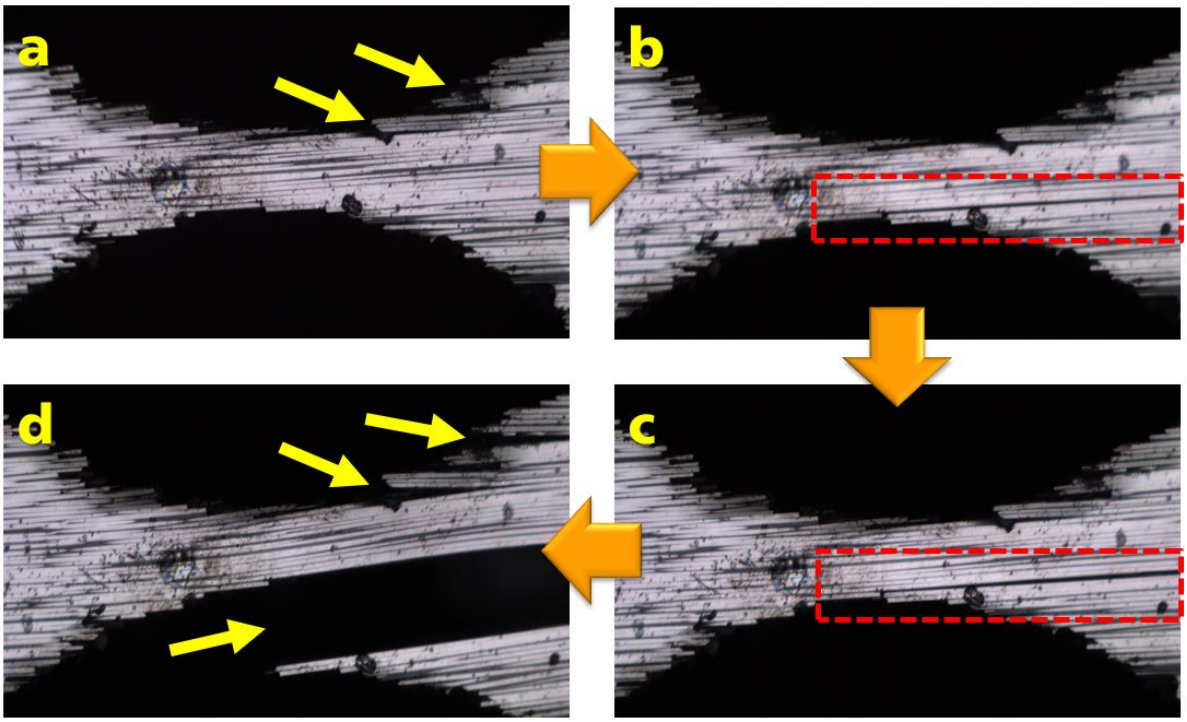

Figure 4.11: Delamination observed in 0° specimen. Panel a: beginning of test, b: 39,000 cycles, c: 44,000 cycles and, d: 385,859 cycles. Specimen number AFT3-0-08-05.

cracking that occurs within a resin-rich area as marked by an arrow on the top right side of the specimen. Despite continuous progression in the matrix cracking, the specimen failed due to fibre fracture rather than matrix cracking, as shown in Figure 4.12c after about 170,219 cycles.

A particular example of crack behaviour in a 90° specimen can be detected from Figure 4.13. There is no visible defect on the specimen before the test starts. However, a small crack begins to form close to the top edge within the gauge section of the specimen as highlighted in red dashed circle in Figure 4.13b. This small crack becomes more noticeable after about 170,021 cycles as in Figure 4.13c. The same crack advances further until it reaches a resin-rich region that passes the middle of the specimen as in Figure 4.13d. Interestingly, the crack persists from progressing further for another 362,150 cycles before it suddenly

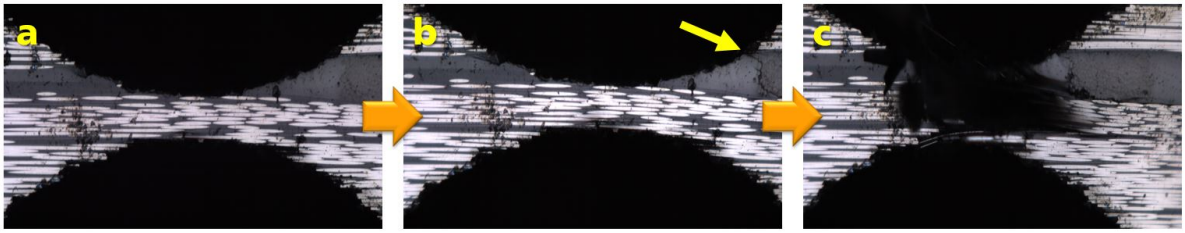

Figure 4.12: Fibre fracture observed in 0° specimen. Panel a: beginning of test, b: 169,671 cycles and c: 170,219 cycles. Specimen number AFT5-0-07-01.

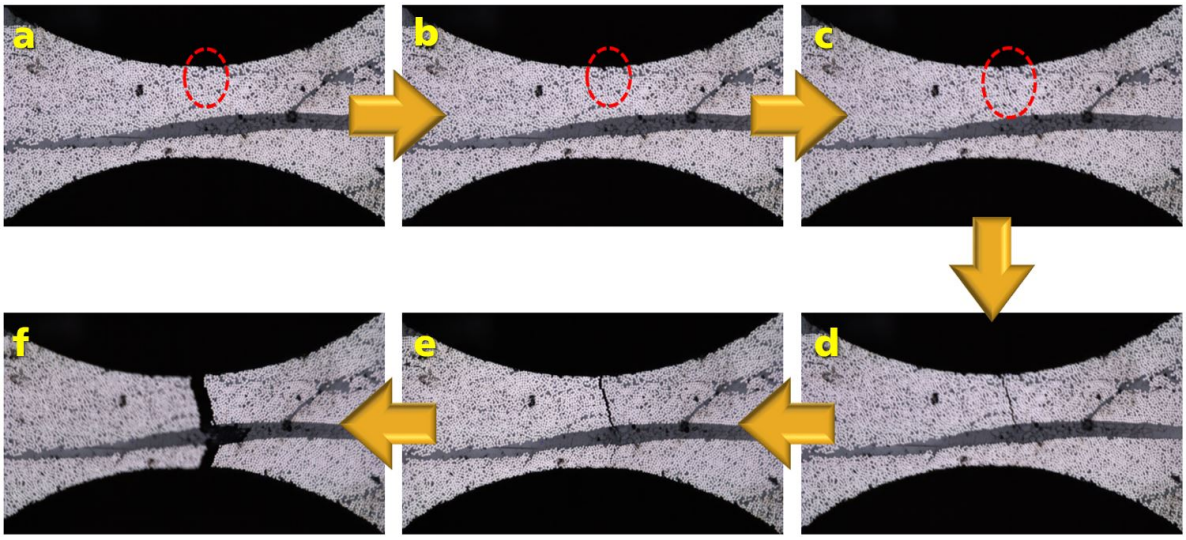

Figure 4.13: Crack damping in 90° specimen. Panel a, b and c: crack progression within 170,021 cycles, d: crack damping for 362,150 cycles, e and f: specimen failure within 10,012 cycles. Total number of cycles to failure is 542,183 cycles. Specimen number AFT3-90-02-02.

evolves and causes the specimen to be broken into halves within 10,012 cycles as can be viewed in Figure 4.13e and f. This specimen fails after about 542,183 cycles under the stress amplitude of 16 MPa. Although specimen in Figure 4.13 and Figure 4.11 have different fibre orientations and fail under different failure mechanisms, both of these specimens demonstrates the capability of its dominant crack to resist from progressing further for quite a large number of cycles before they resume to grow and cause both specimens to fail.

It is also observed that the crack initiates from existing defect in the 90° specimen as shown in Figure 4.14. The red dashed circle in Figure 4.14a indicates an existing hole on the specimen before the test started that may occur during the manufacturing process of the specimen. As the specimen continues to be fatigue-loaded, branches of crack are initiated from the existing hole, with the top crack progressing up until the top edge of the specimen in Figure 4.14b. After about 8,093 cycles, the crack advances, further splitting the specimen into two as shown in Figure 4.14c.

The most common failure observed in all specimens tested despite the orientation is the interface failure between the fibre and the matrix. Of all specimens tested, there are

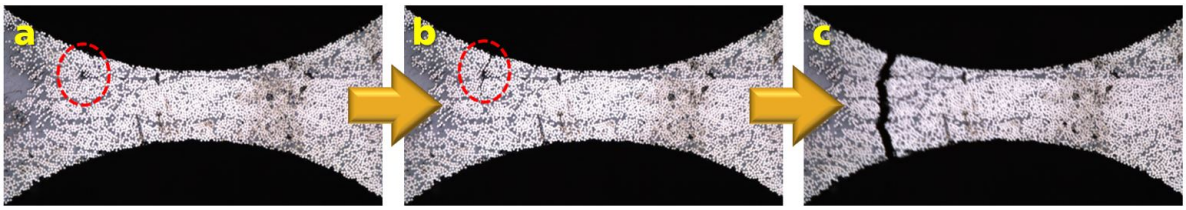

Figure 4.14: Crack initiation from existing defect due to manufacturing process in 90° specimen. Panel a: beginning of test, b: 5,732 cycles and c: 8,093 cycles. Specimen number AFT2-90-09-01.

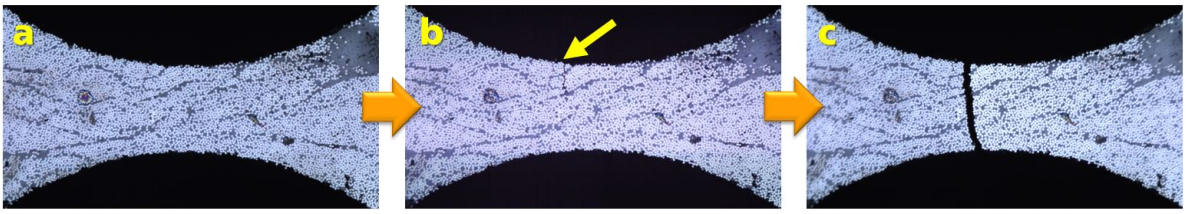

Figure 4.15: Interface failure between fibre and matrix in 90° specimen. The edge where crack initiates is indicated by arrow. Panel a: beginning of test, b: 15,413 cycles and c: 20,918 cycles. Specimen number AFT3-90-02-01.

two specimens that clearly display this as presented in Figure 4.15 and Figure 4.16. Figure 4.15a presents the specimen before the test starts. As the specimen is fatigue-loaded, a crack forms starting from the edge of the specimen (indicated by an arrow in Figure 4.15b) within the interface regions between fibre and matrix. The crack then progresses following the fibre-matrix interface path until it reaches the opposite side of the specimen edge as appeared in Figure 4.15c after 20,918 cycles. Similar behaviour can be deduced from Figure 4.16 where the crack path is not necessarily appearing to be in a straight line; instead, it follows the arrangement of the fibres that are closely packed together and progresses in the direction of these fibres interfaces with the matrix before causing failure in this specimen after 96,753 cycles.

Each specimen has its unique microstructure composition due to the size of the specimens. Some of the specimens tested consist of the resin-rich region included in the area of focus. In some specimens, the crack grows beyond this resin-rich area where plastic deformation of the matrix can be observed as in Figure 4.17. The crack initiation in this 60° specimen can be seen as pointed out by an arrow in Figure 4.17a. As the crack progresses past the fibre-rich region, it then enters the matrix-rich region, as seen in Figure 4.17b. Once the crack is in the matrix-rich region, the crack does not continue to progress further for several thousand cycles where the end of the crack can be observed (pointed out by the arrow in the magnified view of Figure 4.17b). Here, a slight change in the tone of the matrix region ahead of the crack tip can be seen. This change in tone forms an elliptical shape of

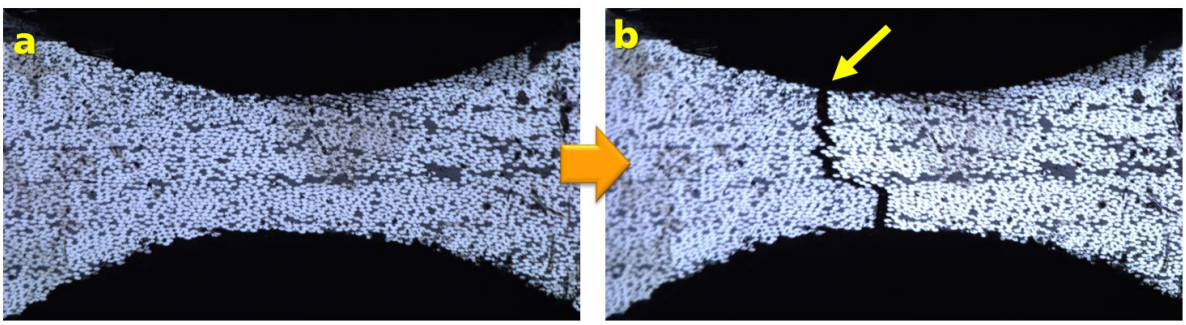

Figure 4.16: Interface failure between fibre and matrix in 30° specimen. The edge where crack initiates is indicated by arrow. Panel a: beginning of test and b: 96,753 cycles. Specimen number AFT7-30-17-01.

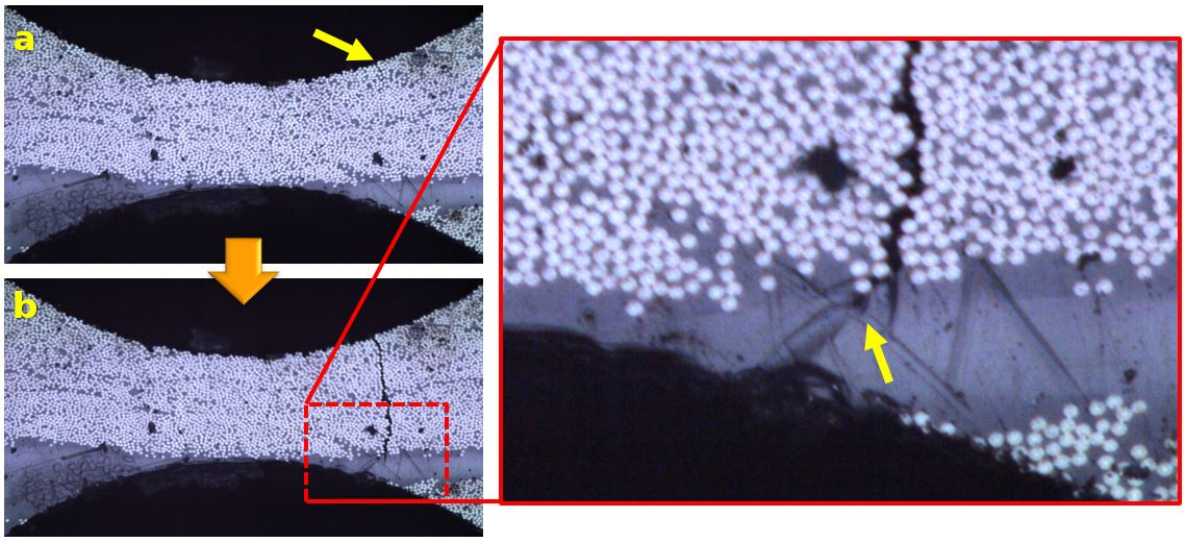

Figure 4.17: Matrix plastic deformation in 60° specimen. Panel a: crack initiation at 39,170 cycles and b: crack reaches matrix region at 112,711 cycles. The specimen breaks after 268,606 cycles. Specimen number AFT11-60-02-01.

a darker shade matrix just ahead of the crack tip. The crack then advances after roughly 155,895 cycles following the shape of the darker shade matrix, which demonstrates that this region experiences plastic deformation. The whole specimen fails after 268,606 cycles under 27 MPa stress amplitude.

Multiple failure mechanisms can also be recognised from several other specimens, including the 45° specimen. There is no observable damage on the specimen at the beginning of the test, as shown in Figure 4.18a. After 6,000 cycles, two cracks begin to form on the opposite edge within the gauge section of the specimen. The initiation points of these cracks are designated by pointed arrows in Figure 4.18b. It can be seen that both of these cracks started in the fibre-rich region before progressing into the matrix-rich region that makes up the more significant portion of the specimen mid-section. Notice also that as these cracks advance into the matrix-rich region, the shade of matrix in the vicinity of the crack changes (matrix plastic deformation), similarly as observed in Figure 4.17b. After about 1,200 cycles, the specimen failed, with only one of these cracks being the dominant crack that caused the failure to the specimen. The crack initiated within the most signific-

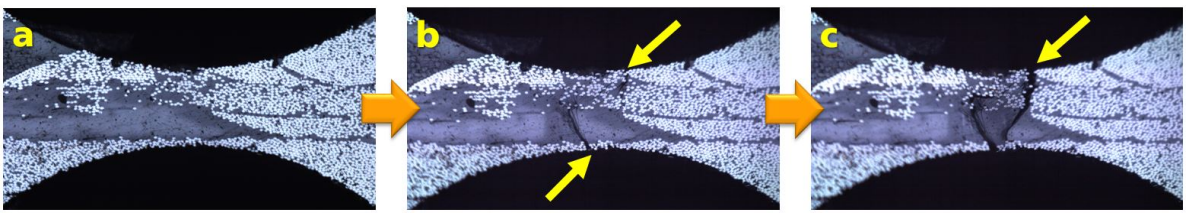

Figure 4.18: Multiple cracks formation and matrix plastic deformation in 45° specimen. Panel a: beginning of test, b: two separate cracks visible at 6,000 cycles and c: specimen breaks at 7,200 cycles. Specimen number AFT9-45-06-01.

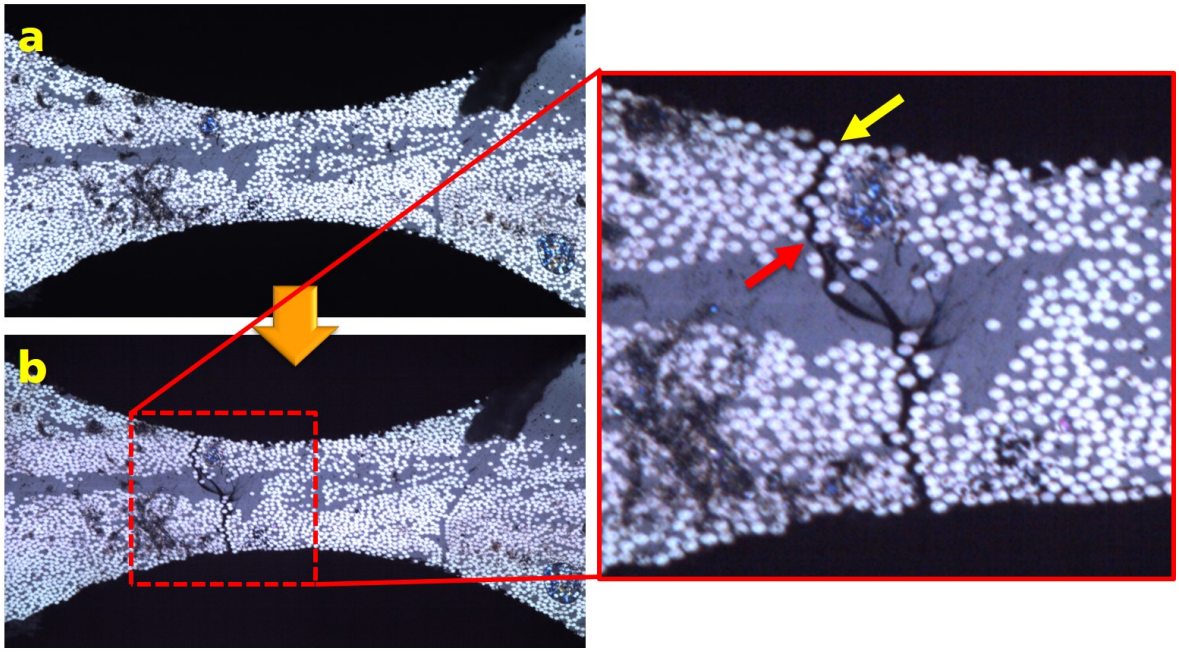

Figure 4.19: Crack branches stemming from a single crack in 45° specimen. Panel a: beginning of test and b: specimen breaks at 99,153 cycles. Specimen number AFT9-45-05-01.

ant fibre-rich region propagates faster compared to the other crack and act as the dominant crack (marked by an arrow in Figure 4.18c). Multiple cracks formation as well as matrix plastic deformation are the two failure mechanisms observable in this specimen.

Several occurrences of multiple cracks formation were observed on specimens regardless of their fibre orientations. The following example of a 45° specimen in Figure 4.19 indicates the formation of crack networks or branching from a single crack. The specimen has no visible crack at the beginning of the test, as shown in Figure 4.19a. A crack is initiated on the top edge of the specimen, indicated by a yellow arrow on Figure 4.19b, as the specimen continues to be fatigue-loaded. The crack can be seen to propagate following one path through the interfaces between fibre and matrix until the crack reaches a matrix-rich region indicated by a red arrow. Here, the crack splits into two branches following the two fibres that spread in front of the crack tip. The crack breaks further into three parts when it encounters another fibre spread apart, maintaining its preference path within the interface between fibre and matrix. The two prominent cracks then merge on the next off fibre to form the dominant crack, with several minor cracks emanating from this main crack. This dominant crack later causes the specimen to fail. What can be deduced here is that crack usually maintains one main path within the fibre-rich region; however, as crack enters the matrix-rich region, it often divides itself to form crack branches.

Not all of the dominant cracks that cause specimens to fail can be observed during the test. Some of these dominant cracks appear pretty suddenly just before the specimen

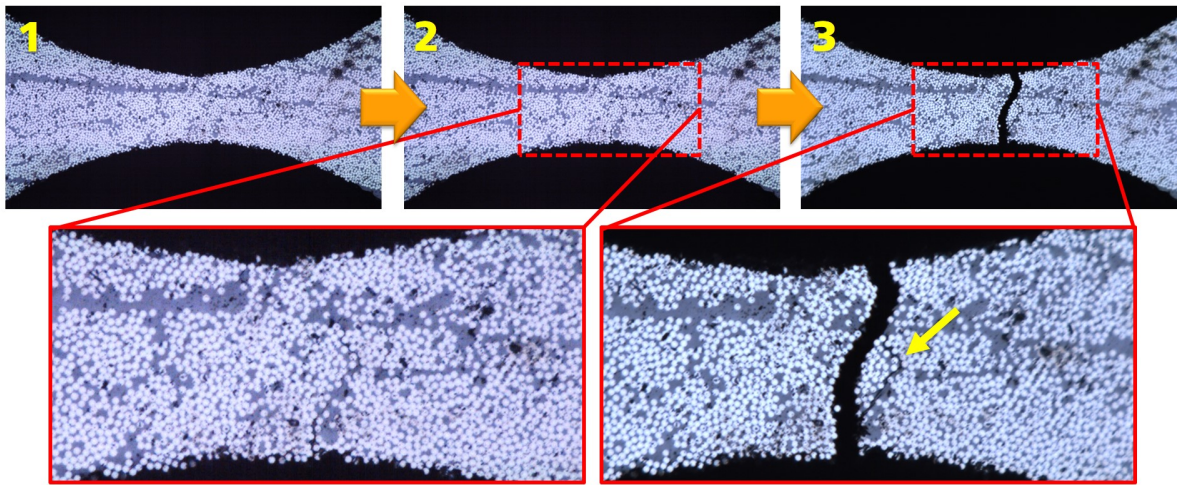

Figure 4.20: Multiple crack formation with final fracture occurring on non-observable crack in 90° specimen. Panel a: beginning of test, b: 694 cycles and c: 905 cycles. Specimen number AFT3-90-04-01.

breaks, and due to this reason, it is not visible during the test. An excellent example of this case can be referred to Figure 4.20. This 90° specimen was fatigue-loaded at 22 MPa stress amplitude with a non-observable crack at the beginning of the test (see Figure 4.20a). After reaching 694 cycles, a slight crack can be observed appearing from the lower gauge edge of the specimen moving upwards as shown in Figure 4.20b. The specimen entirely fails in a brittle manner after 905 cycles. A distinct crack sighted earlier can be seen to be on the right side (indicated by an arrow in the magnified view) to the main crack in Figure 4.20c. The magnified view of this figure indicates that the dominant crack which seems to cause the complete failure of the specimen can not be detected in Figure 4.20b while the one detected earlier is not the dominant crack here.

Figure 4.21 demonstrates another instance whereby the dominant crack that causes the specimen to fail is not observable during the test and appears abruptly just before the sample fails. A crack originates from the lower edge on the left side of the specimen after 982,110 cycles, and this crack travels into the resin-rich region upwards, forming a network

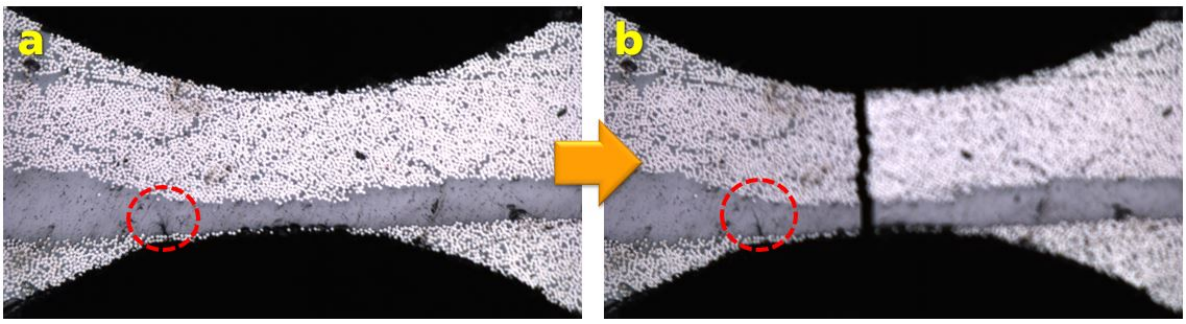

Figure 4.21: Multiple crack formation with dominant crack causes final fracture of a 90° specimen. Panel a: 982,110 cycles and b: 1,006,403 cycles. Specimen number AFT2-90-06-01.

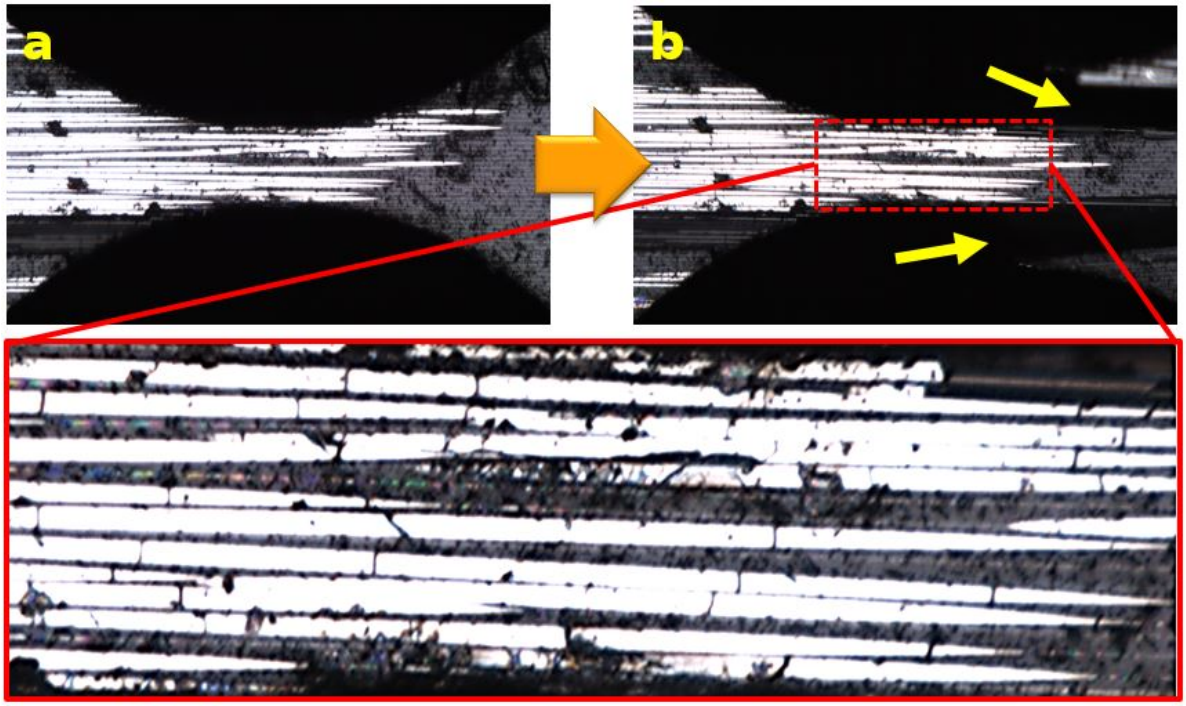

Figure 4.22: Multiple fibre fractures in 0° specimen. Panel a: beginning of test and b: specimen breaks at 358,384 cycles. Specimen number AFT3-0-03-01.

of branches as outlined in the red dotted circle in Figure 4.21a. No pronounced extension of this crack was apparent on view for another 600 cycles. Nevertheless, the specimen fails abruptly when the load cycles reach 1,006,403 cycles by a different crack that appears to the right of the first crack, according to Figure 4.21b. This second crack acted as the principal crack that causes the specimen to break, although it is not the crack that is visible throughout the test.

Multiple failure mechanisms, with one of them being multiple cracks, can also be detected in 0° specimen. Figure 4.22a depicts 0° specimen before it is fatigue loaded without any distinguishable defects prior to the test. The specimen eventually fails after 358,384 cycles, with fibre shear being the leading cause of the failure, as pointed out by the two arrows in Figure 4.22b, causing the grip on the right side of the specimen to be loosened and no further loading is possible. In addition to this, a magnified view of Figure 4.22b focusing on the fibres that appeared on the specimen surface shows severe multiple fibres cracking. Although these fibre cracks are not the leading cause of the specimen failure up to this cycle, the figure clearly shows that multiple fibre cracking already occur on the group of fibres on the surface of the specimens while the whole specimen is still intact.

Aside from possible observation on the failure mechanism of the specimen during failure, a trend on how crack propagates within different regions of the specimen can also be assessed. The subsequent two examples clarify the trend on the crack path. Figure 4.23a

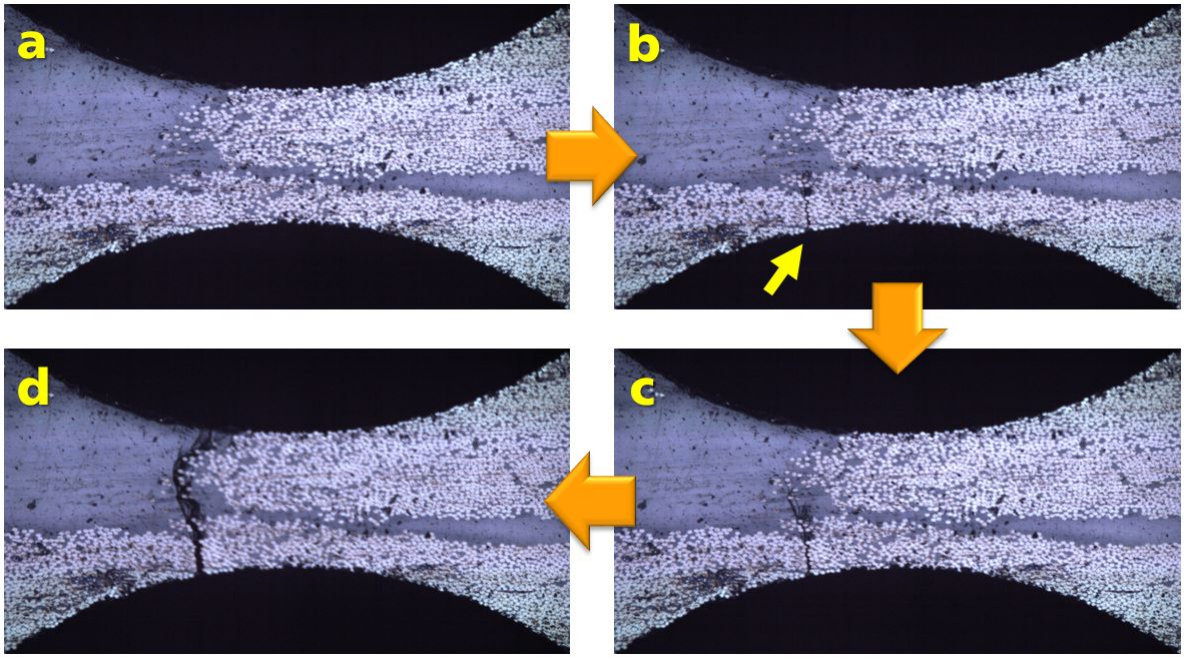

Figure 4.23: Interface between fibre and matrix as crack driving path in a 45° specimen. Panel a: beginning of test, b: 90 cycles, c: 158 cycles and d: specimen breaks at 190 cycles. Specimen number AFT10-45-01-01.

shows a 45° specimen with non-observable defect prior to the test. This specimen is fatigue-loaded at 26.2 MPa stress amplitudes where a small crack can be seen to initiate after just 90 cycles (see arrow in Figure 4.23b). This crack develops from the edge of the specimen within a fibre-rich region. It propagates following the fibre-matrix interface in an almost straight line path until it enters the matrix-rich region in Figure 4.23c. As soon as it enters the matrix-rich region, the crack spreads into several networks with the main branch that extends further towards the direction of the closest dispersed fibre from the crack tip. This network of cracks jumps from one closest dispersed fibre to another to propagate upwards, while crack branches that are too far from the next dispersed fibre cease to propagate further. As the main branch crack advances upwards, a striking crack path is developed in Figure 4.23d. The main crack continues to leap from one dispersed fibre to another to progress further until it reaches the opposite edge of the specimen and causes the specimen to break. The whole specimen break after only 190 cycles. The observed crack path illustrates the prominent role of the interface between fibre and matrix in driving crack propagation rapidly to cause total specimen failure.

The different regions of the specimen microstructure also play an essential role in affecting the crack path. Two central regions can be observed within this 45° specimen in Figure 4.24. The specimen has a resin-rich area stretched from the left to the right side of the lower bottom of the specimen, while the rest of the specimen consists of a fibre-rich region. After 1,200 cycles of fatigue loading on the specimen, a crack started to develop

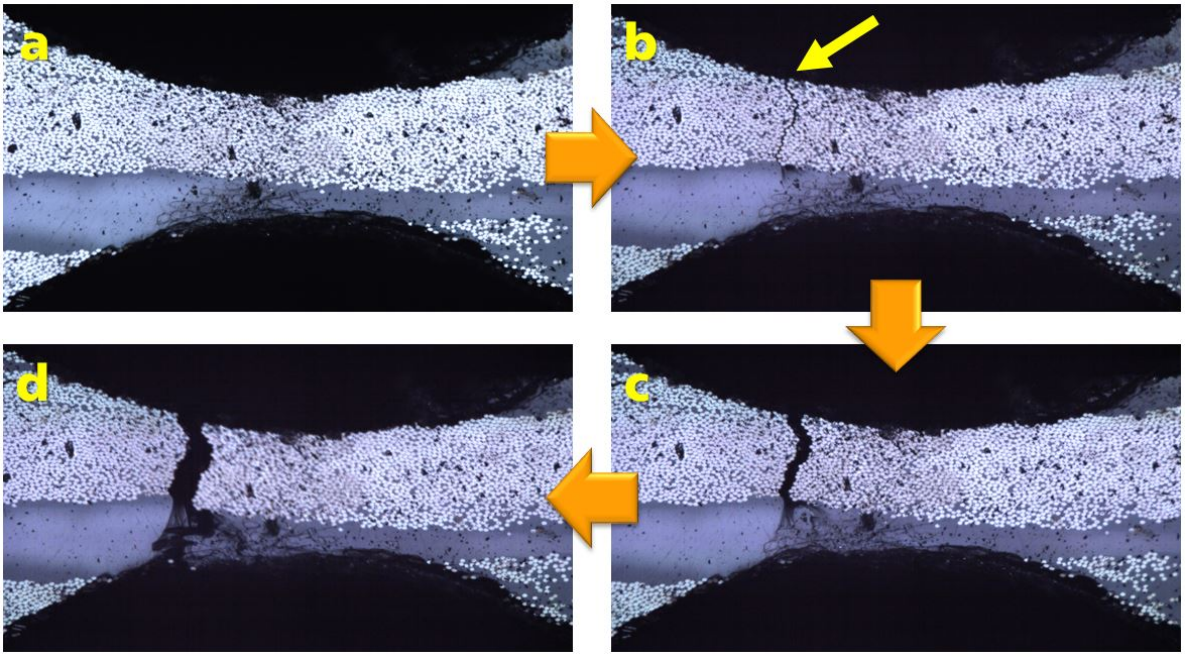

Figure 4.24: The difference in crack path propagation according to different specimen microstructure region in a 45° specimen. Panel a: beginning of test, b: 1,800 cycles, c: 2,400 cycles and d: specimen breaks at 3,000 cycles. Specimen number AFT9-45-07-02.

from the top edge of the specimen. It is important to note that this crack initiates from the fibre-rich region of the specimen instead of the resin-rich side of the specimen as marked by an arrow in Figure 4.24b. A clean course of the crack propagation can be seen across the entire fibre-rich region from this figure until the crack then reaches the subsequent matrix-rich region. Once the crack reaches this region, as in Figure 4.24c, it starts to disseminate into several branches of crack. As the crack expands, larger and broader growth of crack branches can be discovered. Hereinafter, the crack no longer advances in a single crack channel as displayed in Figure 4.24d. A complex scattering of crack branches is a frequent observation that appears in almost all specimens with crack propagation within a matrix-rich region. This is a unique criterion of crack propagation that only happens within the matrix region while the fibre-rich region often exhibits a defined course of crack propagation.

4.2.3 Analysis of Fracture Surfaces

Several selected broken specimen fracture surfaces are further analysed by using SEM to capture the failure mechanism within the studied material. Figure 4.25 shows an example of a fracture surface obtained for a 0° specimen. The primary failure mechanism observed in this 0° specimen is fibre fracture, with all of the fractured fibres appearing rough and serrated reasonably. Almost all of the fibres are observed to break roughly at the same plane, forming a smooth fracture surface with occasional fibres pull-out that appear as hollow

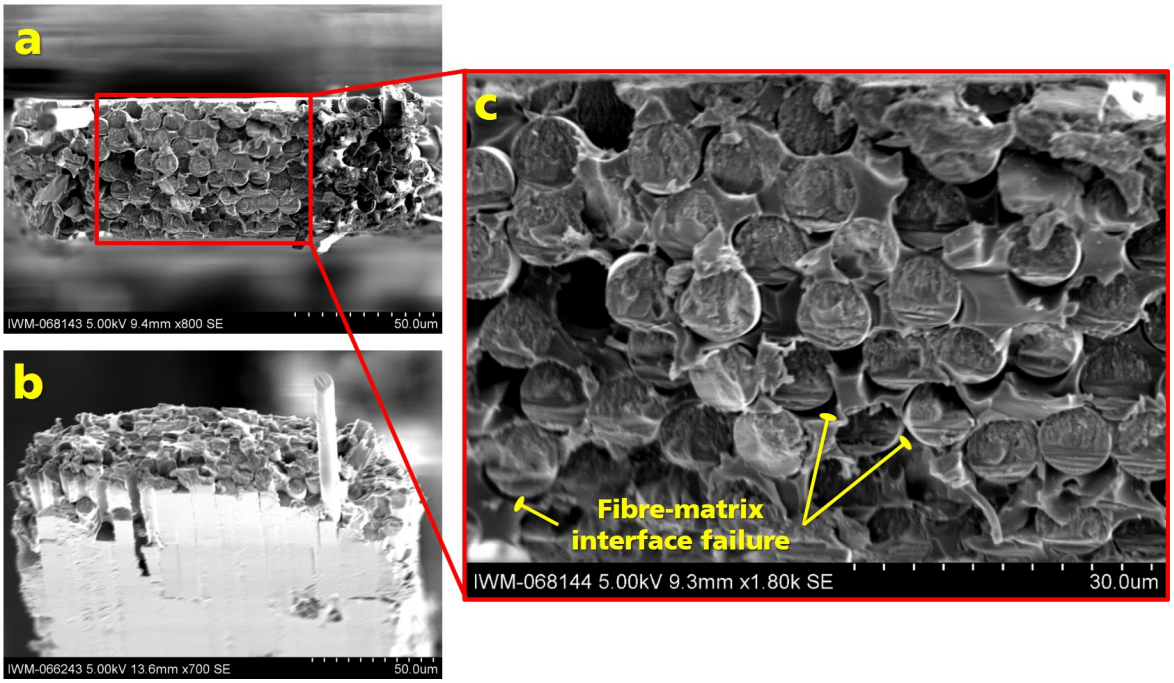

Figure 4.25: SEM of fracture surface from two different views of a 0° specimen. Panel a: specimen cross-section view, b: specimen tilted front view, and c: magnified view of the fibres. Specimen number AFT1-0-02-01.

spaces observed in Figure 4.25a and c. A longer hollow space that stretches downwards roughly 46 μm to verify fibre pull-out can also be viewed from the front view of the specimen as in Figure 4.25b. A close look at Figure 4.25c also reveals a clear gap between fibres and matrix constituents as the indication of an interface between fibre and matrix failure can be found throughout the whole specimen. A single long fibre that protrudes out of the fracture surface in Figure 4.25b has a substantial clean surface which also suggests potential interface fibre-matrix failure on this fibre before the fibre breaks and pulls out of the matrix.

A similar account can be witnessed from another 0° specimen presented in Figure 4.26 whereby all of the fibres in this specimen also break in a way that a smooth fracture surface is obtained. Although the fracture surface of this specimen is not as neat as the specimen in Figure 4.25, an almost planar surface can be seen, including several fibre pull-out markings. Unlike the previous specimen, some of the fibres located on the edge of this specimen are detached from the original fibre bundle and separated from the matrix (see Figure 4.26a) that may indicate interfibre shearing. However, this could only be identified on the right side of the specimen, whereas the left side of the specimen is very well intact. Closer inspection on these separated fibres also shows that these fibres' surfaces appeared to be smooth with hardly any traces of matrix adhering. This indicates that fibre-matrix interface failure also happened in this specimen. Figure 4.26b reveals several fibres which

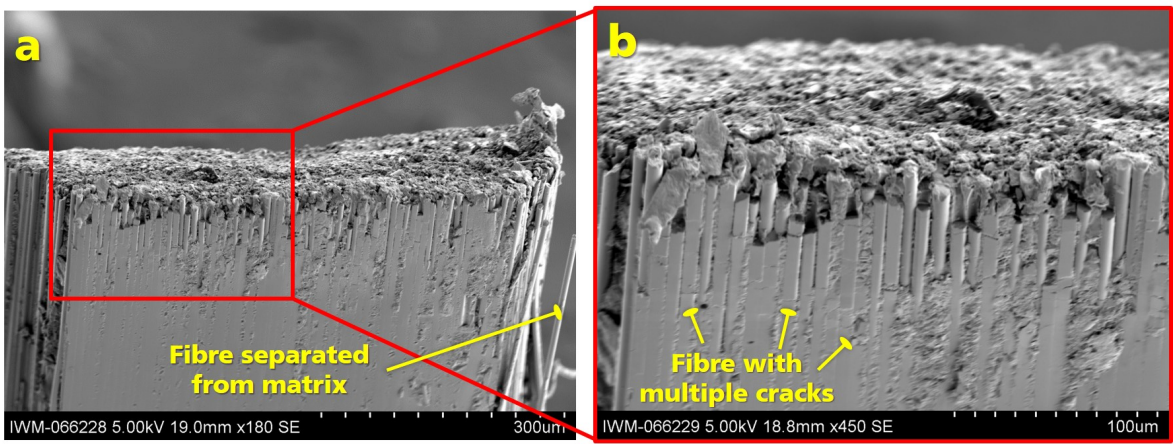

Figure 4.26: Smooth fracture surface of a 0° specimen. Panel a: Specimen tilted front view, and b: magnified view of the fibres. Specimen number AFT3-0-05-03.

exhibit multiple cracks without complete separation at these cracked locations.

Aside from the specimen in Figure 4.26, several other 0° specimens tested in the micro-fatigue test also failed due to interfibre shearing. The following is a fracture surface example of another specimen (see Figure 4.27). The fracture surface of this quarter specimen also shows a planar fracture surface as the previous two examples. There are also small fragments of broken fibres that are still attached to the fracture surface visible from the cross-section view of the specimen in Figure 4.27a. The fracture surface of a fibre-rich region can be easily distinguished as the fibre rich region fracture surface often appeared covered by small particles of matrix residues. In contrast, the matrix rich region, as observed in the left bottom corner of Figure 4.27a, has a slightly cleaner appearance with no matrix residues. Figure 4.27b shows slightly the side of the specimen that experienced interfibre shearing during the test. Separation of fibres can be easily noticed here due to the interfibre shear, with all of these fibres appearing to have a neat surface analogous to the previous examples. Other identical observations were occurrences of fibre pull-out as well as a fibre-matrix interface as focused in the magnified view of Figure 4.27c. Unlike Figure 4.25c, some of the fractured fibres surface in Figure 4.27c exhibit rugged surfaces while others are smooth.

Three separate fibre clusters resulting from the interfibre shearing induced by plies separation within the specimen is displayed in Figure 4.28a. The separation of these plies results from the manufacturing process of the material made of several plies stacked and sewed together to form a unidirectional plate, creating weak interfaces between these plies that are susceptible to interfibre shearing. Several fragments of fractured fibres are still loosely attached to the top fibre cluster, together with numerous traces of fibre pull-outs and fibre-matrix debonding. Interfibre shearing that occurs between these fibre clusters is

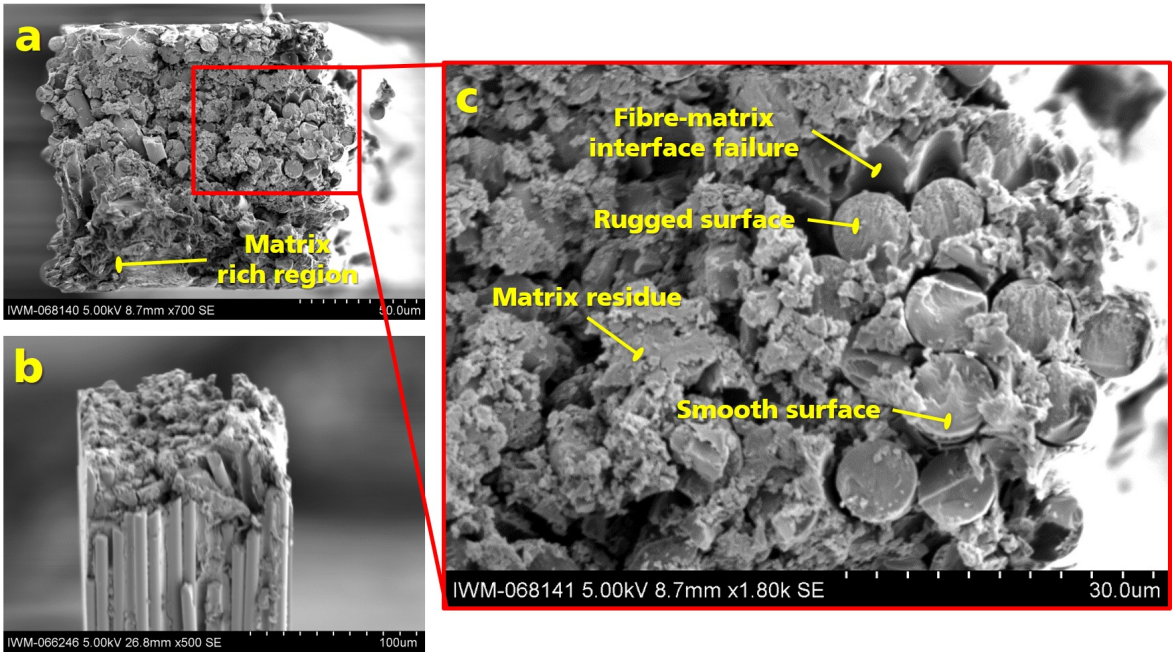

Figure 4.27: A 0° specimen that fails due to interfibre shear failure. Panel a: specimen cross-section view, b: specimen tilted side view, and c: magnified view of the fibres. Specimen number AFT5-0-06-01.

even more prominent in Figure 4.28b. The shearing advances in a straight line following the ply boundary that could potentially break the specimen into smaller pieces in the case if it proceeds further.

Failure mechanisms observed in off-axis specimens are somewhat different from longitudinal specimens, although similar ones are still present. This is mainly due to the arrangement of fibres not directly aligned to the loading direction, making matrix failure the primary failure mechanism observed in these specimens. In this case, matrix became the dominant constituents susceptible to fatigue failure. The examples below look closely at

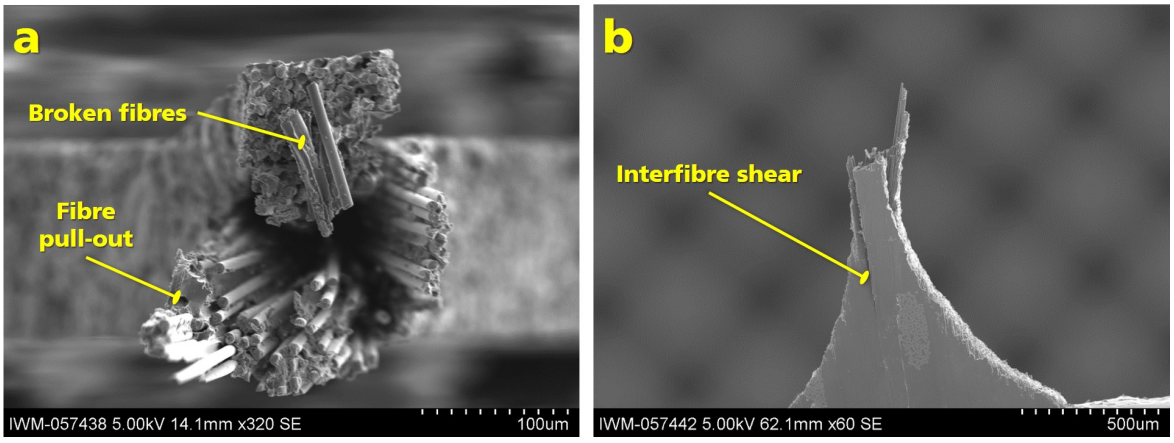

Figure 4.28: Interfibre shear between fibre clusters in 0° specimen. Panel a: specimen cross-section view, and b: specimen overall view. Specimen number AFT5-0-07-01.

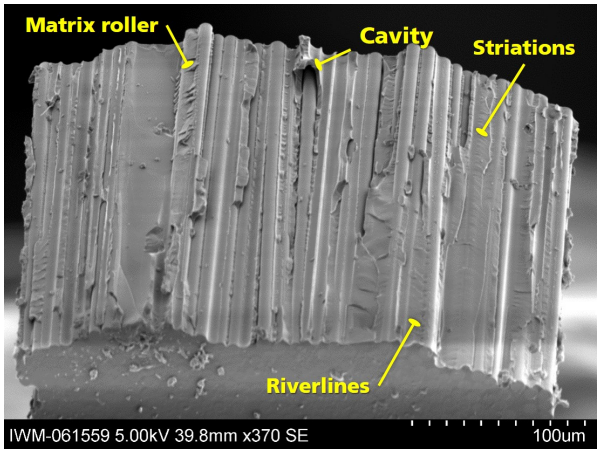

Figure 4.29: Fracture surface of a 90° specimen. Specimen number AFT2-90-09-01.

different types of failure mechanisms displayed by these off-axis specimens. One of the similarities observed in the off-axis specimen fracture surface presented in Figure 4.29 is the fibre-matrix debonding. This can be seen from the remaining fibres' visible smooth and clean surfaces. A clean and smooth fibre surface without any traces of matrix adhered to the fibre surface suggests fibre-matrix interface failure. A slight gap around the fibres and neat fibre imprint channels on the fracture surface also signify fibre-matrix failure in this specimen. Despite rarity in the occurrences of fibre pull-out on the off-axis specimen, this can be seen in this 90° specimen where a protruding clump of matrix on the middle top edge of this specimen contains a hollow space that equals the diameter of a fibre. This hollow cavity proves that fibre pull-out occurs in this specimen and fibre-matrix failure. The different types of matrix failures are also present in this specimen, such as striations, riverlines and matrix rollers that appears mainly in the matrix between two adjacent fibres.

Fibre bundle separation is one type of failure commonly visible in the off-axis specimens. This failure is also an effect contributed by fibre-matrix interface failure, as demonstrated in Figure 4.30. There are three instances of fibre bundles separation from the fracture surface of this specimen where crack that causes the fibre-matrix debonding to neatly follows the boundary of the fibre bundle instead of the individual fibre.

Another example of a 90° specimen that introduces another type of matrix failure is shown in Figure 4.31. Matrix cracking on the specimen's front surface is visible from the figure. The crack within this matrix region seems to follow a group of foreign artefact interfaces that do not appear to be carbon fibres. Each of these artefacts is twice the diameter of carbon fibres and are believed to be part of matrix impurities. The weak interfaces between these impurities within the matrix become the factor that contributes towards matrix crack inside this specimen. Apart from the matrix crack due to the matrix impurities, this specimen's other failures are fibre-matrix debonding, scarps, riverlines and ribs.

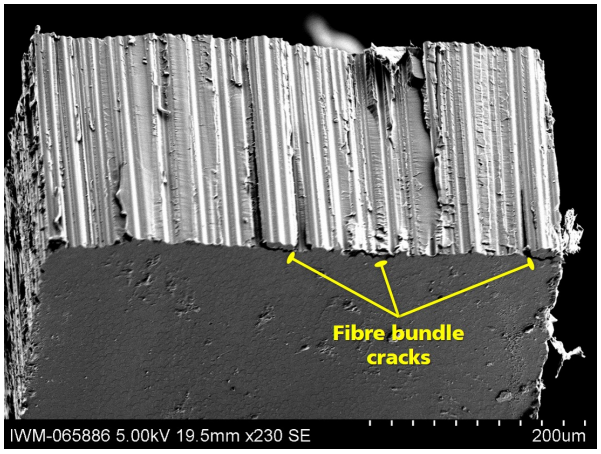

Figure 4.30: Fibre bundle separation as a result of fibre-matrix interface failure in 90° specimen. Specimen number AFT2-90-07-01.

Aside from the similar fracture surface features among all off-axis specimens, some specific features can only be observed in 45° specimens as shown in Figure 4.32. Although textured microflow can also be observed in other specimens, it is more apparent in the resin-rich region of this specimen, including the appearance of scarps. Moreover, two distinct parabola features of the textured microflow can be observed in the lower part of Figure 4.32. One unique feature that can only be explicitly observed in 45° specimens is the appearance of striations within the fibre imprint region that indicates fatigue interfibre shearing failure. This feature appears as an alternate sequence of dark and bright lines oriented perpendicular to the fibre direction. Interestingly, striations oriented in both directions can also be seen on the left fibre imprint of the exact figure. The striations' source could be from the matrix defect that appears in the form of dotted matrix residue, which factors for the striations to progress in the opposite directions. On top of this, this specimen's fracture surface also exhibits heavier matrix rollers in the lower part of the fracture

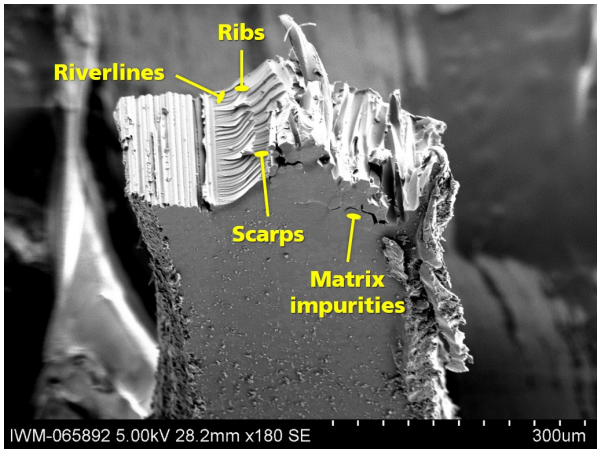

Figure 4.31: Matrix failure due to matrix impurities in 90° specimen. Specimen number AFT3-90-12-01.

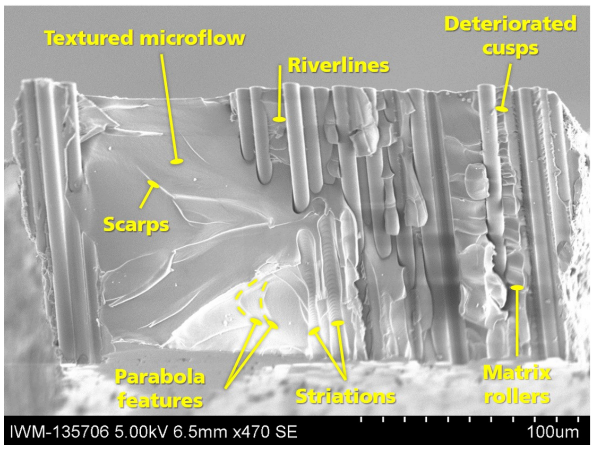

Figure 4.32: Fracture surface of a 45° specimen. Specimen number AFT9-45-06-01.

surface. It progresses towards deteriorated cusps in the upper part of the fracture surface. Likewise, in previous off-axis specimens, this specimen also depicts clear evidence of riverlines.

The use of polyester (PES) yarn to sew the plies together during the manufacturing of the material plate is also evident through fracture surface analysis of some off-axis specimens. The specimen fracture surface in Figure 4.33 shows the middle of the specimen splitting due to the congregates of PES yarns used to sew the fibres to form ply together. The splitting of the specimen occurs at the joint section between two plies stacked together. Also, note that the matrix better adheres to the yarn's surface than the carbon fibres. Apart from PES yarns that are visible, the other element that has been used in the manufacturing process of the material tested is glass fibres. The presence of glass fibres within this material can also be distinguished from several of the off-axis specimens tested as shown in Figure 4.34. The glass fibres are easily identifiable due to the opposite orientation of the

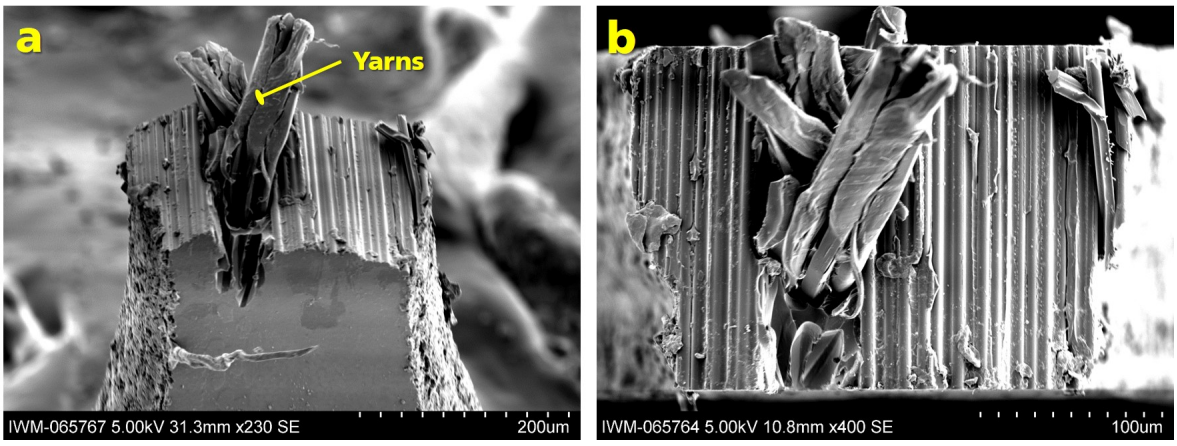

Figure 4.33: Polyester yarn in 90° specimen. Panel a: specimen tilted front view, and b: specimen cross-section view. Specimen number AFT3-90-02-02.

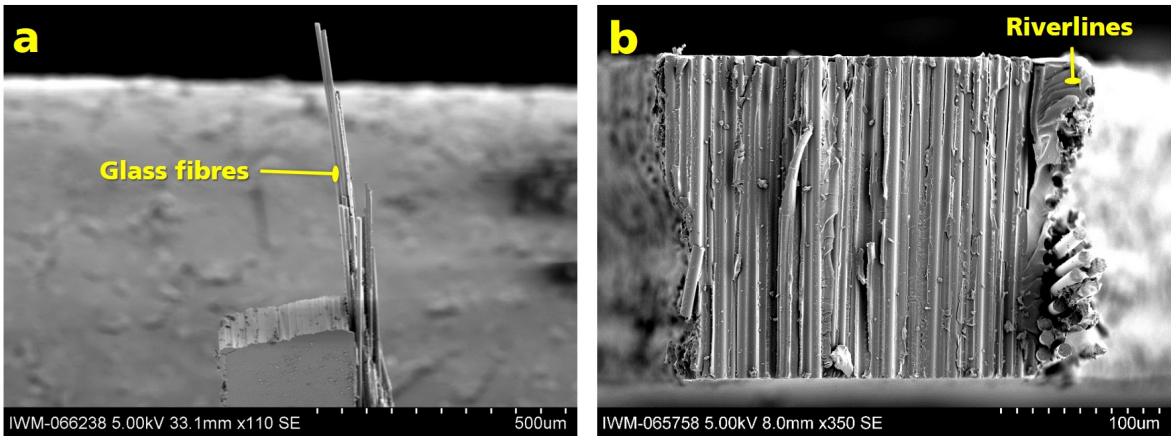

Figure 4.34: Group of glass fibres in two separate 90° specimens. Panel a: group of long glass fibres in specimen number AFT4-90-01-01, and b: group of shorter glass fibres in specimen number AFT3-90-03-01).

glass fibres to the carbon fibres. The glass fibres are seen in a group. In the case of both specimens, they are located on the edge of the gauge section of the specimens.

4.2.4 Continuum Damage Model on Micro-Fatigue Specimens

The fatigue degradation model that was introduced previously in Section 3 was applied to the results presented in Section 4.2.1. Similar steps for parameters determination as specified in Section 3.3.3 were done by using the material elastic properties obtained on the macroscopic specimens following the standardised test procedures according to the ISO standards [135].

A single element FE computation under sinusoidal fatigue load with an appropriate choice of acceleration factor has been applied. The FE computation runs until the element completely fails with an accumulation of damage variables that reaches 95%. Several assumptions have been considered to simplify the material parameters required in this case. The first assumption involves considering a monoclinic system whereby only two axes are perpendicular to each other. In this case, x_2 direction and x_3 direction are considered equivalent resulting in $dD_2 = dD_3$. As a result, $A_{22} = A_{33}$, $A_{31} = A_{21}$ and $A_{32} = A_{23}$. Due to the lack of experimental data on the effect of σ_{23} on both $\mathrm{d}D_2$ and $\mathrm{d}D_3$, A_{32} and $A_{23} = 0$. To further reduce the number of parameters involved, it also assumed that σ_{12} and σ_{13} only affect the interfibre failure without contributing towards fibre failure described in $\mathrm{d}D_1$. Therefore, A_{12} and $A_{13} = 0$. Given these assumptions, a set of parameters A and n obtained from experimental data of three different fibre orientations (0°, 90° and 45°) were determined. Since all micro-fatigue tests only involve tension-tension mode fatigue, only tension mode parameters are required here. The complete list of all material parameters obtained is presented in Table 4.6.

Table 4.6: Material parameters for micro-fatigue specimens

Elastic parameters					
E_1 (GPa)	E_2 (GPa)	G_{12} (GPa)	G_{23} (GPa)	ν_{12} (-)	ν_{23} (-)
106.8	10.2	4.2	2.7	0.3	0.3
Warping function parameters					
a_I	a_{II}	D_I	D_{II}	b	
5.0	10.0	0.1	0.5	0.5	
Damage evolution parameters					
A^t_{11} (MPa^{-n+1})	n^t_{11} (-)	A^t_{22} (MPa^{-n+1})	n^t_{22} (-)	A_{21} (MPa^{-n+1})	n_{21} (-)
6×10^{-15}	3	3×10^{-87}	50	1×10^{-76}	50

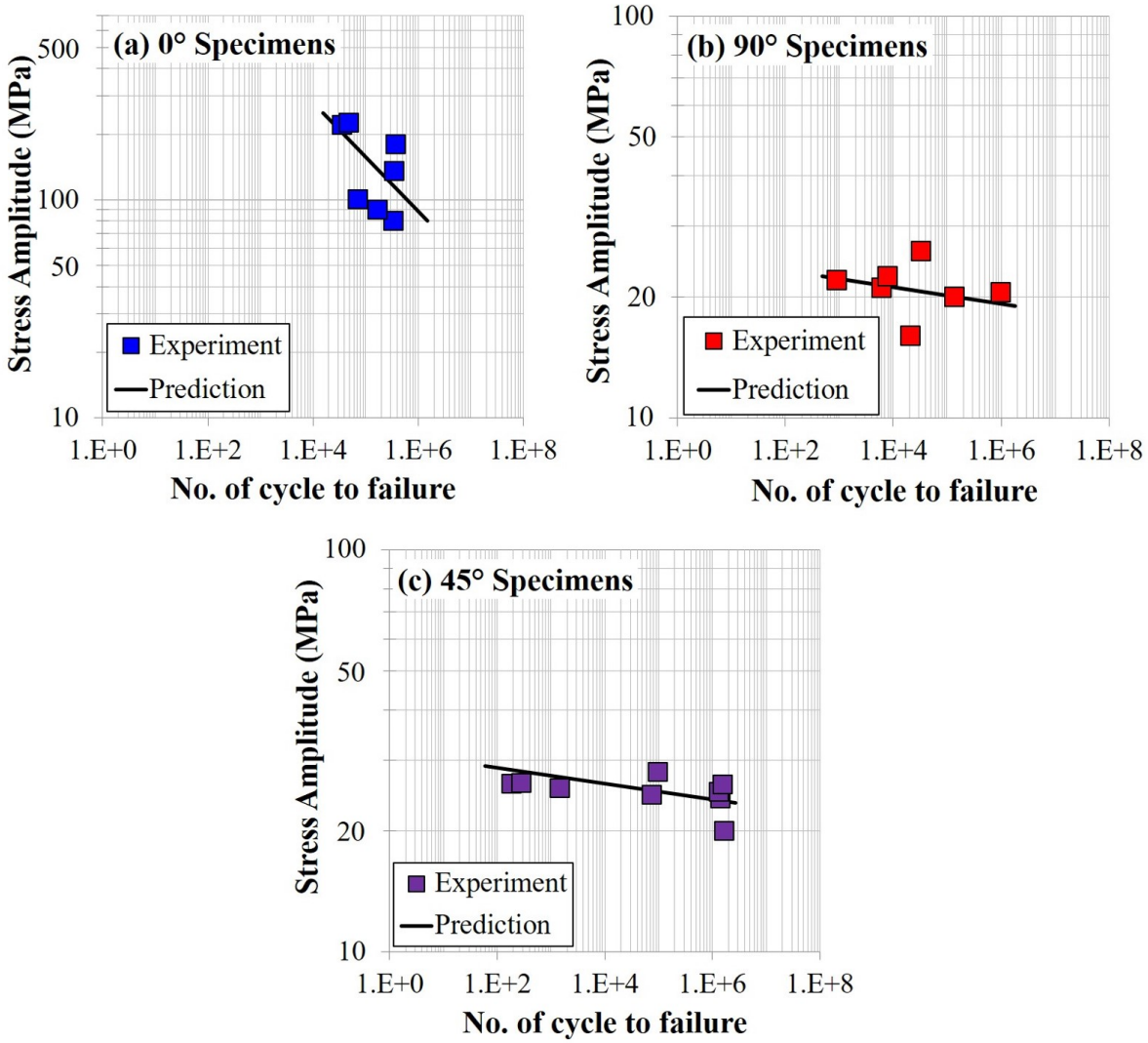

Figure 4.35: Determination of material parameters for fatigue degradation model on micro-fatigue experimental data.

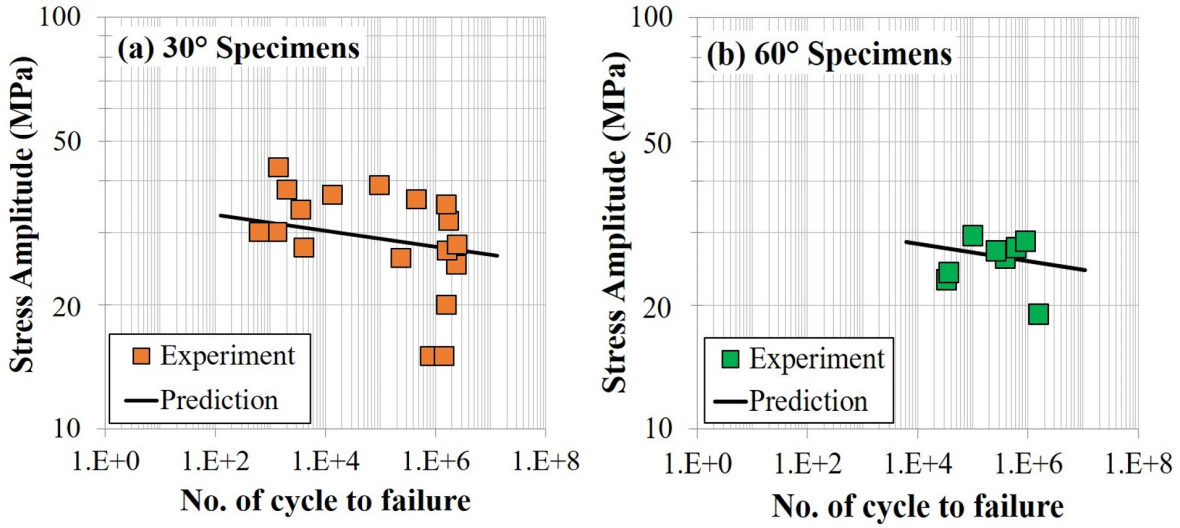

Figure 4.36: Validation on two fibre orientations (30° and 60°) from micro-fatigue experimental data.

The S-N diagrams resulting from applying the fatigue degradation model for parameters determination are given in Figure 4.35. All of the cases presented in Figure 4.35 agree well with the micro-fatigue experimental data showing linear material response in double logarithmic relations between stress amplitude and the number of cycles to failure. Note that the numerical prediction presented was obtained from multiple data points. It can be seen that a fixed value of parameter n is sufficient to produce a numerical prediction that is almost exact to the experimental data in the case of non-zero fibre orientation whereas a substantially smaller parameter n value is required to reproduce the slope of the S-N curve for 0° fibre orientation specimens.

Using only the three sets of material parameters A and n obtained earlier, the fatigue degradation model is now applied on two other fibre orientations (30° and 60°) for validation. The results of numerical predictions for the two cases are presented in Figure 4.36. A similar linear relationship on double logarithmic S-N curves was obtained as the results for the two fibre orientations presented earlier. In both cases, all of the data produced from the numerical predictions show very good agreement with the experimental data.

4.3 Discussions

4.3.1 Fatigue Failure Mechanisms

The tensile fatigue performance of CFRP presented as an S-N diagram indicates fibre orientation effect on the failure mechanisms of tested CFRP. This is evident from the value of the gradient and the intercept for 0° specimens that is the highest compared to the other fibre orientations. This is mainly because the fibres are oriented parallel to the loading

direction. In this case, all of the load applied are entirely carried by the fibres causing the most preferred failure mode to be fibre fracture. Due to the significant difference in the fibre's stiffness compared to the matrix, higher energy is required to initiate fracture within the 0° specimens. This is also evident from the higher value of fatigue tensile strength for longitudinal specimens compared to other orientation specimens. Regarding 90° specimens, the failure mechanism observed for these specimens is completely different from those of longitudinal specimens since the primary failure mode for this orientation is the matrix failure mode. In these specimens, the fibre is oriented perpendicular to the loading direction. Therefore, most of the load is now fully carried by the matrix. Due to this reason, fibre-matrix interface failure is especially important to the fatigue response of 90° specimens. 90° specimens serve as the other extreme when compared to the case of 0° specimens, which results in the lowest value of its gradient and tensile fatigue strength. Much lower energy is required to initiate failure within 90° specimen due to the weaker properties of the matrix and higher stiffness of the fibre. Interestingly, all other fibre orientation specimens fulfil the transition from longitudinal specimens to 90° specimens. These multi-fibre orientations are dominated by shearing failure mode, with 30° being the closest to the 0° specimens while 60° to the 90° specimens. Individual failure mechanisms for two extreme cases will be discussed in detail further.

Failure mechanisms in 0° specimens. Since fibres are oriented parallel to the loading direction, the load applied are carried by the fibres. This allows the fibre to confine the strain within the matrix and limits extensive distortion, thus minimising the occurrences of matrix failure. Few failure mechanisms are observable during in-situ monitoring, while others can be detected from the fracture surface analysis of the broken specimens. One of the most important damage mechanisms for longitudinal specimens is fibre fracture. Fibre fracture is the final stage of failure for longitudinal specimens after several stages of failure mechanism progression. Failure in the specimen started with the formation of voids and microcracks within the matrix, followed by coalescence of microcracks and interfacial debonding. As the crack progresses, delamination appears before it starts to grow, leading to fibre breaking. In almost all of the longitudinal specimens tested, initiation of microcracks and void can not be observed. However, specimen failure can be detected once delamination occurs. An exception is in the case of Figure 4.12. Due to the resin-rich area in the microstructure of the specimen, matrix cracks can be seen first developing within the specimen. Compared to the fibre, the weaker properties of the matrix allow failure to be initiated at lower energy. Since micro-damage initiation usually occur at the weakest spot, the matrix crack progresses further towards the fibre-matrix interface (into the fibre-

rich region), reducing the effectiveness of the stress transfer between fibres. Despite no other matrix cracking observed after the specimen reached 169,671 cycles, fibre fracture was induced in a rather explosive manner after about 548 cycles because of the enormous energy stored within the fibres that were released simultaneously when the matrix fails. Consequently, the stress fails to be distributed effectively among other fibres.

Another significant observation is multiple fibre fractures occurring in Figure 4.22. The specimen shows signs of delamination at the beginning of fatigue load followed by the development of multiple fibre fractures on the surface of the specimen within one minute of image transition (600 cycles). This indicates that the development of these multiple fibre fractures is almost instantaneous given the frequency of the loading applied (10Hz). This final specimen failure is caused by delamination instead of fibre fracture. Although this occurrence can be detected in only one specimen during the in-situ observation, similar observations can also be seen in fracture surfaces of specimen in Figure 4.25b and Figure 4.26, where both of these specimens failed due to fibre fracture. Most of the fibres on the surface of these specimens show cracks in multiple places and jagged fibre breakage along the fracture surfaces. The fracture surface behind the front surface is much smoother with more uniform fibre breaking. Based on this, we understand that these multiple fibre fractures only occur on the surfaces of the specimen that has been processed (ground and polished). The specimen preparation process involved weakens the fibres on the surface of the specimens. Presumably, all of the fibres below the prepared surface are without any cracking, which allows them to carry the load applied, thus facilitating the specimen to remain intact.

Delamination can be found in the majority of the longitudinal specimens, for example, in Figure 4.11. In this instance, fibres are separated from the matrix; however, the fibre continues to carry the applied load. Similar observation can be seen from the fatigue testing on standard specimens discussed by Kawai et al. [67]. Delaminations can be found in several places of this specimen. Some delaminations are initiated during loading, and the manufacturing process induces another before the test. In this specimen, delamination initiated during loading has a higher growth rate than the one induces through the manufacturing process, which then becomes the cause of the specimen failure. Minor delamination on the specimen edge also occurs as in Figure 4.26. Edge delamination observed in specimens usually arises from the rough fibre edges along the specimen contour during the specimen cutting process. In the case of the specimen in Figure 4.27, delamination induced during loading causes the specimen to be broken into half parallel to fibre orientation. However, the test did not stop immediately as the fibres continued to carry the load. Both halves

of the specimen later broke through fibre fracture, causing fragmentation of the specimen into four parts. This occurs due to the ineffectiveness of stress transfer caused by delamination. Unlike the previous specimen, the specimen in Figure 4.28 experienced delamination along fibre bundles causing the specimen to break into three distinct parts. The delamination occurs along the resin-rich region that separates these bundles, as this region is the weak spot preferred for microcrack propagation. In practice, once delaminations within the material occur, it is considered equivalent to total failure of the structure regardless of whether the fibres still carry the load.

Several damage mechanisms are non-observable during the in-situ monitoring, one of them being fibre pull-out as observed in Figure 4.25 and Figure 4.28. This appeared either from the view of fibre protruding from the fracture surface or a hollow cavity found on the fracture surface. Pull-out of fibres perpendicular to the fracture plane consumes far greater failure energy than the matrix fracture. Consequently, it justifies significantly higher fatigue tensile strength of the longitudinal specimens than off-axis specimens. Additionally, fibre-matrix interface failure was also detected in all longitudinal specimens, as a gap in matrix adhesion around fibres or those of protruded fibres (fibre pull-out) having a clean surface. Both events indicate low adhesion of matrix and fibre, which significantly affect fatigue lifetime of material as identified by Zhuang et al., Miyano et al. and Nakada et al. [37, 143, 144]. An obvious advantage with micro-fatigue testing here is the ability to monitor the fracture surface of the longitudinal specimens, unlike standard testing, which usually produces a very uneven fracture surface [9]. This enhances the possibility to provide more insights on fatigue fracture behaviour of UD 0° specimens.

Failure mechanisms of non-zero angle specimens. Failure mechanisms observed in UD non-zero angle specimens are different from 0° specimens. This is mainly due to the fibres not oriented parallel to the loading direction, making matrix properties a crucial contributor to its fatigue failure behaviour [145]. Accordingly, 90° specimens have the lowest tensile fatigue strength out of all non-zero angle specimens since the fibres act as important stress concentrators for crack initiation and crack paths within the material.

One of the most common damage mechanisms visible in all of these specimens is fibre-matrix interface failure. Almost all microcracks observed during the micro-fatigue test initiates from the specimen edge within the fibre-rich region. When the dominant microcrack occurs within this region, the failure is relatively progressive within a short number of cycles. Whereas a microcrack that propagates into a matrix-rich region has a much lower growth rate than a fibre-rich region. Frequently, this crack propagation is halted temporarily before it continues to progress further. This could be attributed to the weaker fibre-

matrix interface than the matrix, thus requiring a longer time and higher energy to facilitate crack growth within the matrix-rich region. Here, the matrix act somewhat like a damper for the crack temporarily; for example in Figure 4.13 and Figure 4.21.

Another important observation here is that cracks that propagate into matrix rich regions form crack branching as detected, for instance in Figure 4.19. Matrix plastic deformation also can be observed from the change in the matrix shade ahead of the crack tip from one of the branches. The change in matrix shade suggests redistribution of stress within the material by the matrix. This observation can be seen from Figure 4.17 and 4.18. This supports the understanding of the delay provided by the matrix to extend the crack further. Otherwise, specimens fully covered by fibre-rich region fail rapidly within a short cycle (see Figure 4.15, 4.16 and 4.20). Some of these cracks appear as a single crack, whereas some as multiple cracks as presented in Figure 4.20 (non-observable) and Figure 4.21 (observable). Besides that, interface failure could also be detected from the clean fibre surface without matrix residue in all fracture surfaces especially Figure 4.29 and Figure 4.30. Not only that interface failure affects individual fibres within the specimen, but it also occurs along a few fibre bundles, as displayed in Figure 4.30. Furthermore, interface failure also adds to fibre pull-out as in Figure 4.29 and Figure 4.30. This commends higher failure energy than matrix fracture that causes the material's instability/spurious mechanical response when combined. Resultantly, both specimens exhibit material response that falls outside of the accepted test range to be included in the S-N curves.

Clear evidence of interfibre shear can be detected from the fracture surface of 45° specimens through the appearance of striations within fibre imprints as seen in Figure 4.32. This observation is consistent with finding on macro-specimens reported by Grove and Smith [146]. The striations are oriented perpendicular to the fibre direction and occur as part of microcracks extension originally initiated at the fibre-matrix interface. Striations could also occur in both directions, as detected in the left side fibre of the same specimen. The striations that run in both directions are caused by localised differences in the fibre-matrix bond, which disrupts the stress states along the fibre length and causes the crack to propagate in the direction opposing each other.

Several events of manufacturing process induced failure can also be distinguished. In Figure 4.14 for example, crack is initiated from a void that forms during manufacturing of the specimen. As for Figure 4.33, we could see that delamination develops in the direction parallel to the yarn. The yarn presence in this specimen poses as the weakest spot where the crack could quickly propagate without any resisting fibre. Some 90° specimens also were found to contain a slight amount of longitudinal glass fibres, such as in Figure 4.34.

Moreover, a slight similarity in failure mechanism, particularly within this region, to UD 0° can be noted. Finally, the fracture surface of Figure 4.31 signifies the introduction of impurities into the matrix rich region that causes matrix cracking to develop around what seems to look like a bundle of much thicker fibre made of the same matrix.

A few matrix failure patterns can be recognised from the fracture surfaces of 90° specimens. Figure 4.30 and Figure 4.29 display a distinct crack growth region from the smooth area (stable fatigue crack propagation) [147] on the matrix fracture surface. While the residual fracture areas appeared to have a much more structured and rougher appearance, particularly in Figure 4.31, these findings are similar to what has been observed by Brunbauer et al. [30] along with river lines on the fracture surfaces.

4.3.2 Crack Path Pattern

A general trend on the crack propagation pattern can be deduced from the off-axis specimens tested under the micro-fatigue test, regardless of its orientation. A crack that emerges within a fibre rich region often propagates in a defined single path manner, whereas it often branches out when it reaches matrix rich region (see for example Figure 4.19, 4.21, 4.23 and 4.24). The crack growth rate for a crack within a matrix rich region is lower due to the crack growth damping effect provided by the viscosity nature of the matrix. Besides that, evidence of matrix plastic deformation can be seen within the matrix, proving that the matrix can consume more failure energy and distribute the energy by spreading the crack into networks and damping the growth. When a crack branches within a matrix rich region, the branch located the closest to fibre is the most preferred crack to extend further. This is most likely due to the crack preference to grow along the fibre/matrix interface region. In some cases, several crack branches could also extend simultaneously if multiple branches are similarly close to a dispersed fibre, whereby merging of these cracks will create a single crack path through the fibre rich region. Supposing for the case when the specimen contains multiple separate cracks, fibre volume fraction evaluation could suggest the dominant crack responsible for causing final specimen failure.

A suggestion on fibre volume fraction evaluation can be made by comparing the fibre volume against the whole volume for multiple cracks within the specimen. Figure 4.21 shows two distinct cracks initiated on the specimen during the test, with only one of the cracks responsible for causing the final specimen failure. Two areas containing the crack at the end stage of specimen fracture as in Figure 4.37 are considered, and the fibre volume fraction of these areas are evaluated. Since the specimen orientation is 90°, the volume of the fibre can be calculated simply by using the cylinder volume formula with the height of the fibre to be the same as the thickness of the specimen. Interestingly, it is found that the

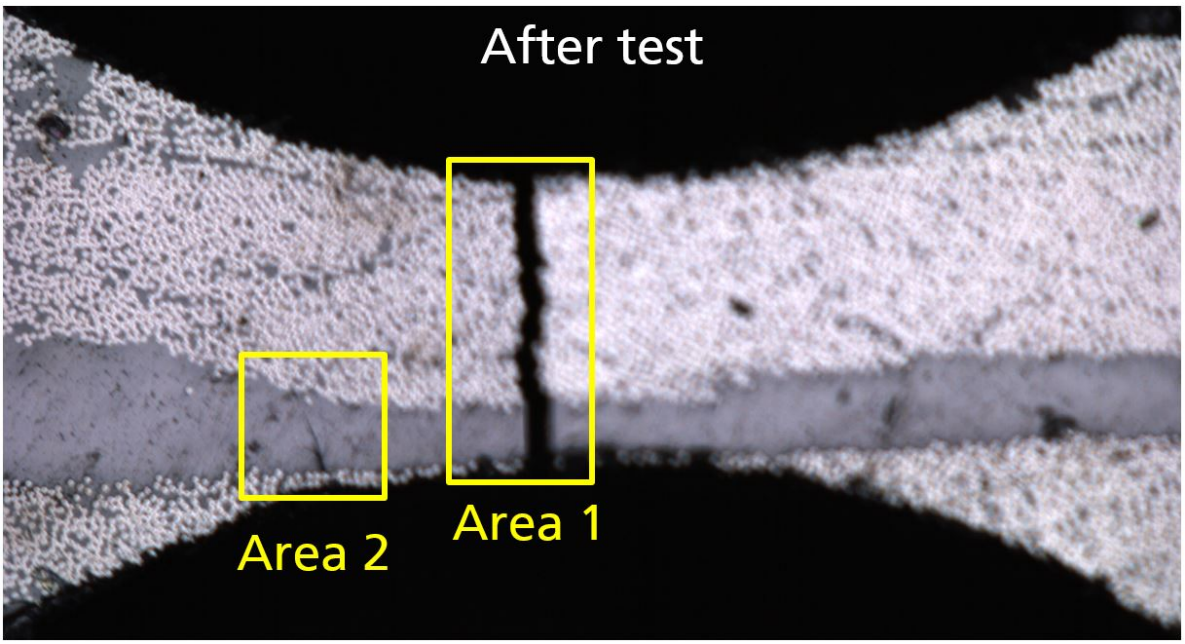

Figure 4.37: Comparison of fibre volume fraction for multiple cracks.

fibre volume fraction for the area with the dominant crack is 49.1% (Area 1), while Area 2 is 17.2%. A similar evaluation has been done on all of the 90° specimens tested as presented in Table 4.7. Likewise, the fibre volume fraction calculated from the main crack that causes the specimen to fail for all specimens is higher than 40%. This indicates that higher fibre volume fraction is certainly the crack path preference in 90° specimens. This also supports the importance of the fibre-matrix interface role in the crack propagation that causes failure within the specimens.

Crack growth direction can also be estimated based on features observed on the fracture surface of micro-specimens. In the case of longitudinal specimens with fibre fracture, radial lines or texture variation of fibre fracture surface as seen in Figure 4.27c are helpful. In this figure, a group of fractured fibres that form a flat region indicating the same fracture plane shared by these fibres can be observed. Additionally, some of these fibres ex-

Table 4.7: Results of fibre volume fraction evaluation on selected 90° specimens.

Specimens	Stress Amplitude (MPa)	No. of cycles	Fibre volume fraction (%)
AFT3-90-02-01	16	20,918	44.25
AFT3-90-01-03	20	136,588	45.50
AFT2-90-06-01	20.5	1,006,403	49.09
AFT3-90-13-01	21	6,088	40.45
AFT3-90-04-01	22	900	49.91
AFT2-90-09-01	22.5	8,093	46.02

hibit smooth and rugged surfaces. A smooth fractured fibre surface on Fibre A compared to all other fibres there, as noted in Figure 4.38, suggests crack initiation and slow crack propagation with just enough amount of energy to propagate the crack through this region. The crack later extends past the fibre into Fibre B, follows into Fibre C and D. Here, the fractured fibre surface showcases a more rugged texture due to the increase in the crack acceleration and divergence of the fracture plane as the crack enter these fibre regions. The crack can later be seen to radiate further to Fibre E, F and G with the growth indicated by yellow arrow markings in Figure 4.38. The crack growth direction follows the transition from a smooth fracture fibre surface to a more rugged surface, similar to the concept of mirror, mist, and hackle observed in macro-specimens [146].

The textured microflow is another valuable feature of the fracture surface to predict crack growth direction. The first type is known as ribs, as seen in Figure 4.31. Ribs are associated with the event of crack arrest that is regularly spaced and oriented normal to the crack growth direction [148]. Besides ribs, there are three other features whereby crack growth direction can be deduced from, and these features can be observed clearly from Figure 4.32. The first feature is termed scarps. Scarps occur when two side-by-side crack planes converge and form a slightly higher step. As mentioned by Bass in his report [148], crack grow parallel to scarps. However, in the case where evolved scarps met with converge crack planes, crack branching is formed where the crack later merge into a channel. This feature is known as riverlines as depicted in Figure 4.39a. With riverlines, the crack grows following the direction of the merging branches [148]. The last feature distinguishable from this specimen is the parabola feature. This occurs when primary and secondary crack fronts that develop separately arise from local discontinuity meets. The crack growth direction is parallel to the symmetric axis that crosses through the parabola vertex in the direction away from the vertex [148]. An illustration of the crack growth direction based on

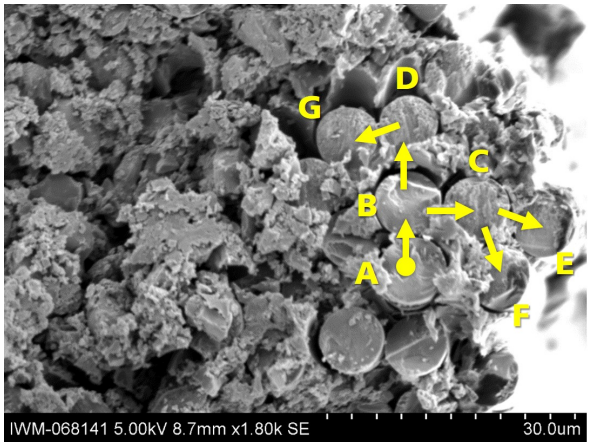

Figure 4.38: Determination of crack growth direction from radial lines on fibre fracture surface.

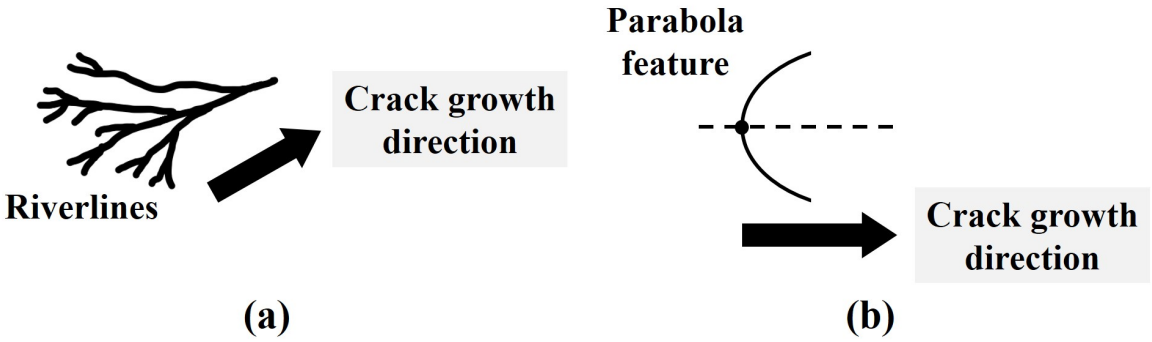

Figure 4.39: Determination of crack growth direction from textured microflow. Panel a: riverlines, and b: parabola features.

the parabola feature can be referred to in Figure 4.39b. Combining all three of these features, the global crack growth direction for the specimen in Figure 4.32 is found to be from left to right as marked in Figure 4.40.

4.3.3 Scatter Analysis

The data deviation error (data scatter) is presented by two values, namely RMSE and 5-95% percentile, where both share identical trends. It is found that 0° and 30° orientation specimens show the biggest scatter indicated by the larger value of RMSE and a wider range of stress amplitude bounded by 5% and 95% quantile lines. The reverse can be true for bigger angle orientation specimens (45° until 90° specimens). In general, the scattering in the specimens could be due to several factors, particularly sample size effect and specimen quality.

Scatter in smaller angle specimens. Several factors possibly contributed to the scatter in 0° specimens (see Figure 4.10a). The first reason for the scatter is the sample size effect which causes variation in fibre volume fraction within the gauge section from one spe-

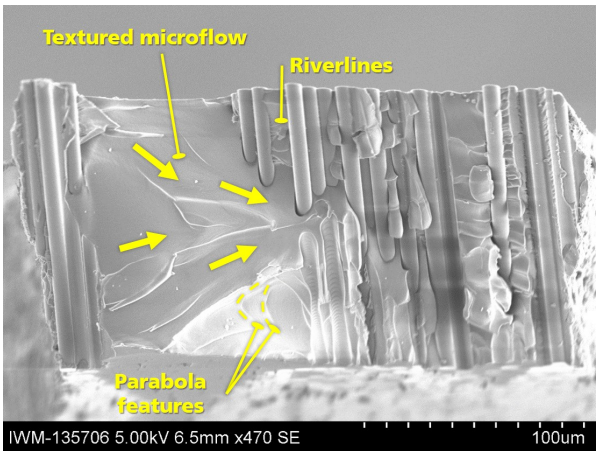

Figure 4.40: Determination of crack growth direction on Specimen AFT9-45-06-01.

cimen to another. Since most of the load is carried by these fibres, once the fibre fails in a brittle manner, it will cause stress to redistribute towards the neighbouring fibres. The stress redistribution in the form of wave propagation that originates from the defected spot increases the overall peak load experience by the neighbouring fibres. Since there is less damping medium (matrix) to absorb and spread this load effectively, especially when fibre-matrix interface failure occurs, the sudden localised peak load causes the fibre to break abruptly; hence the scatter [13]. Moreover, the quality of the 0° specimens also contributes to the scatter. The majority of the 0° specimens include some rough edges from the cutting process of the specimens. These rough edges further assist delamination within the specimen. Depending on where these delaminations are induced, the load distribution within the specimen is greatly affected. Despite the large scatter for the 0° specimens, the micro-fatigue test of this orientation specimens is valid on multiple grounds. Firstly, the specimens undergo fractures mainly within the gauge section resulting in a well-defined fracture surface. Unlike most standard 0° specimens [9, 67], fracture surface analysis on these specimens is made possible, given that the specimens experienced no fragmentation after they failed the test. Furthermore, most of the standard specimen usually experienced cracking that led to the specimen's final failure within the clamping region. This is because this part of the specimen sustained a higher force due to clamping [9]. Additionally, the wave propagation from the entire test setup presents a greater effect on the specimen when compared to the micro-fatigue setup on micro-specimen. With regards to the scatter in the 30° specimen shown in Figure 4.10b, the specimen quality of this orientation specimen is undoubtedly better when compared to the 0° specimens. However, high scatter can still be found within these specimens, although not exactly surprising as shown to be common for UD CFRP material by Barron et al. [44]. Another possible cause of the high scattering for both orientation specimens could arise due to the ability of the material to dissipate energy at different stress amplitudes. As shown by Montesano et al. [46], the temperature within the material increases sharply when the specimens are tested at high stress amplitude compared to the low stress amplitude. The specimen's ability to dissipate energy varies from one point within the specimen to another due to the inhomogeneity in the specimen microstructure. Non-uniform temperature distribution occurs within the specimen, also from one specimen to another, which might have caused higher scatter in general for both 0° and 30° orientation specimens. Nevertheless, the result suggests that more study is required further to understand the failure behaviour of these orientation specimens.

Scatter in bigger angle specimens. Bigger angle specimens display higher microstructure inhomogeneity from one specimen to another. The scatter for all of these specimens are lower when compared to 0° and 30° orientation specimens (see Figure 4.10c, d and e). The lower scattering is potentially due to the primary failure mechanism for off-axis specimens, which involves fibre-matrix interface debonding. Since the specimens are prepared to ensure that the gauge section will be made of only one fibre bundle (achievable in most cases), most specimens' primary failure mechanism is preserved for as long as the specimens failed within the gauge section. Due to this, scattering contributed by the microstructure inhomogeneity within the off-axis specimens is eliminated. Hence, smaller scatter can be found in bigger angle specimens.

Overall, scattering within the specimens could be due to several factors, with some of the factors affecting all orientations while the other seems to affect only a particular orientation. The sample size effect, which is more critical in the case of micro-specimens, introduces variation in one specimen microstructure to another. This could be seen affecting all specimen orientations. Another critical factor that causes scatter is the specimen manufacturing process quality. This is found to affect 0° specimens the most compared to other specimen orientations.

4.3.4 Test Acceptance and Failure Mode

The percentage for accepted test ranges from 38% up to 86% across all specimen orientations because of the different material response from the specimen during the test that causes the measured load experienced by the specimens to move outside of the intended stress amplitude level range. Specimens with 45° and 0° orientation are found to have the lowest acceptance percentage, while 60° and 90° orientation specimens have identical acceptance percentages, with 30° orientation specimens being the most stable.

Unstable material response in 45° orientation specimens. The instability due to the spurious material response within 45° orientation specimens is likely contributed by inter-fibre shearing as the dominant failure mechanism within the specimens. According to Barron et al. and Kharrazi et al. [44, 149], ±45° are more affected by frequency during loading due to the heat dissipation through the fibre-matrix shearing than 0° UD CFRP. Given this knowledge and the high degree of inter-fibre shearing within our micro-specimens, similar observations are highly potential to apply to these specimens. More kinetic energy is generated through inter-fibre shearing within the specimens, which later is converted into heat energy and dissipates through the same mechanism. Sensitivity to the loading frequency and higher amount of kinetic energy generation coupled with heat energy dissipa-

tion might have been the most significant contributor to the instability experienced during the test. This effect may be further studied in the future by introducing a micro-fatigue test on different frequencies. Since the majority of the 45° specimens tested are of excellent quality, the material response instability is solely due to the inter-fibre shearing mechanism of the specimens.

Unstable material response in 0° orientation specimens. The unstable material response within 0° specimens during the test is mostly due to the heterogeneous microcrack initiation that later leads towards delamination within the specimens. This is a non-preferred mechanism in the longitudinal specimens as it dramatically reduces the effectiveness of stress transfer between one fibre to another by the matrix. Since delamination might be one of the failure modes that require the least amount of energy to be initiated, the possibility for this type of failure to be initiated in the specimen is unpredictable and simply difficult to be detected [150]. The uncertainty in delamination initiation causes the material response to be chaotic. Particularly when delamination can be easily induced by several factors such as specimen size effect and specimen quality. Delamination that is induced by machining defects [47] and residual stresses from the manufacturing process [48] is, to this day, unavoidable.

Unstable material response in 60° and 90° orientation specimens. 60° and 90° orientation specimens demonstrate equal instability in the material response during the micro-fatigue test. This is probable considering the characteristic of the specimens being the most brittle compared to other orientation specimens. The brittleness is contributed by fibre-matrix interface debonding acting as the dominant failure mode for both orientations [32]. The brittle nature of the specimens leads to reduced ability of the specimens to relax (response) during fatigue loading. As an effect, microcrack density is much lower as stress redistribution is ineffective, which later causes rapid coalescence and abrupt failure of the specimens [151].

Material response in 30° orientation specimens. Surprisingly, 30° orientation specimens have the highest percentage of test acceptance which also means that the specimens are the most stable during the test. The high test acceptance percentage is presumably due to no chaotic delamination occurring within the specimens during the test, unlike 0° orientation specimens. Apart from that, these specimens also are less brittle when compared to 60° and 90° specimens. It is a fascinating finding with a moderate effect of inter-fibre shear within the material compared to 45° specimens.

Table 4.8: Specimens observations from different milling parameters.

Parameters	Specimens*	Observation on specimens		
		heat zone	rough edges	specimen breaks
Cutting speed: 10,000 rpm	L	Severe	Severe	Yes
Feedrate: 67 mm/min	O	Severe	Moderate	No
Cutting speed: 15,000 rpm	L	Mild	Severe	Yes
Feedrate: 50 mm/min	O	Mild	Mild	No
Cutting speed: 5,000 rpm	L	None	Severe	Yes
Feedrate: 50 mm/min	O	None	None	No

* L: Longitudinal specimens, O: Off-axis specimens.

4.3.5 Effect of Milling Parameters on Specimen Quality

Milling parameters play an important role in producing good quality specimens. The study's two main parameters vary the cutting speed and feedrate, maintaining the same type of micro-mill head throughout the study (diamond coated mill head). Table 4.8 provides observations on longitudinal and off-axis specimens as an effect of changing the milling parameters. From the observations summarised in Table 4.8, it is found that these milling parameters yield different effects for longitudinal and off-axis specimens. There are three primary observations done on the specimens to determine their quality. These include the appearance of a heat-affected zone (HAZ) on the specimen surface, rough edges including the formation of burr that is still attached to the specimen edges, and breaking of specimens. In the first parameters trial set, all specimens show severe HAZ appearance, with most of them occurring along the edges of the specimens. However, in some of the cases, we could also see the occurrences of smaller disperse HAZ over the entire specimen surface (see Figure 4.41a), including the HAZ that started from the edge and radiates to the middle of the specimen (see Figure 4.41b).

Based on all of the specimens investigated, severe HAZ can be observed in all specimens cut with high feedrate and cutting speed. A combination of high value in both parameters creates more heated particle fragments and shards from the cutting process, which flew onto the specimen surfaces, spreading a smaller disperse HAZ and some scratching the surface. This is potentially due to the increase in the temperature and amount of heat generated during the cutting process, especially since the micro-milling is done in dry conditions without coolant. This condition matches what has been found by Gara et al. [152], who observed that the heat generated during machining of CFRP (slotting) is removed mainly by the formation of chips that has greater temperature when compared to the cutting tool and workpiece contact temperature. Considering dry micro-milling is un-

avoidable because of CFRP susceptibility towards moisture, reducing the cutting speed, and the feedrate is the best chance to minimise the heating effect. This is evident when the appearance of HAZ on all specimen surfaces is eliminated from the result of milling using the smallest feedrate and cutting speed.

In terms of the quality of specimen edges, it is visible from observation under the optical microscope. Most of the specimens exhibit the formation of small and brittle swarf and burrs, likely due to this material's low shear stress resistance. Significant improvement in the amount of visible formation of burrs, including the size of the burrs on the specimen edges, can be obtained from reducing the cutting speed and feedrate in the case of off-axis specimens, unlike longitudinal specimens. No visible improvement can be seen in the case of longitudinal specimens for every trial set of milling parameters. All longitudinal specimens exhibit rough protrusion of fibres and severe delamination that starts from the edge of the specimen, with some of the specimens even breaking. Figure 4.42 shows an example of longitudinal specimen damages after milling. Notice that the top-left edge of the specimen in Figure 4.42a is relatively smooth, whereas the top-right edge of the specimen is severely damaged with evidence of delamination. This severe fluffing of fibre end and delamination could be due to the fibre bending effect caused by the mill head just before the fibres are cut. This observation is even more severe, especially along the edges where there is a width transition from the gauge section to the triangular section of the specimen. This finding is parallel to the study done by Pecat et al. and Ghafarizadeh et al. [153, 154], which explains the effect of cutting direction on the surface quality of CFRP. Since the milling direction moves from left to right, the top left region of the specimen exhibits a similar cutting quality of +45° angle to the mill head, the gauge section to the 0° angle, while the top right side of the specimen to the -45° angle, as shown by Pecat et al. [153]. The bending of fibres caused by the mill head produces a high tensile load perpendicular to the fibre

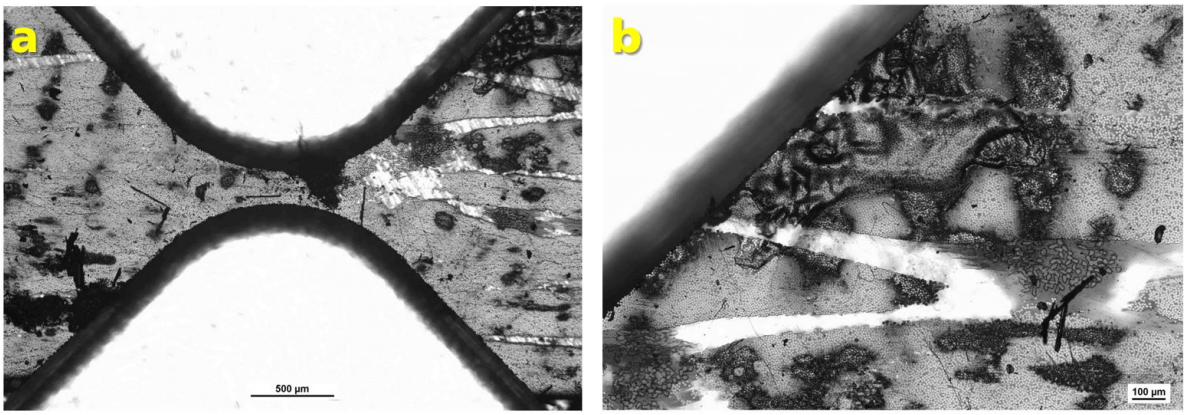

Figure 4.41: Observation of heat affected zone on transverse specimen.

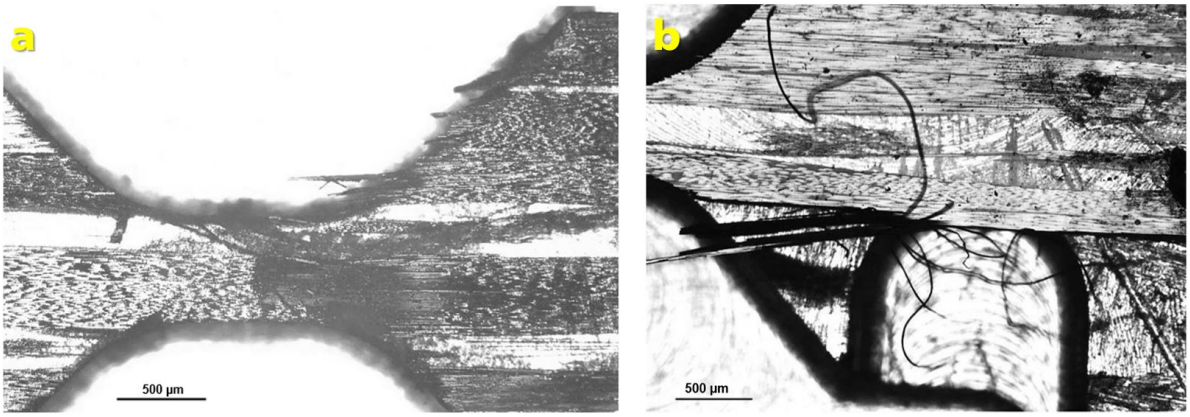

Figure 4.42: Effect of milling on longitudinal specimen (a: severe damage on the specimen surface, b: delamination that causes the specimen to break).

direction. Due to the low tensile strength of the UD fibres where matrix properties most dominate, severe cracks parallel to the fibre direction or delamination can be seen when the angle between the fibres and the mill head is -45°. However, in the case where the angle of the fibres and the mill head is +45°, the tensile load applied nearly follows the direction of the fibre where the tensile strength is maximum. Therefore, no severe delamination can be noticed on this side of the specimen. Severe delamination in the specimens followed by the specimen breaking could also be detected as in Figure 4.42b. From the three sets of parameters tested, it is established that the most critical parameter which influences the surface quality of the specimens is the feedrate. This conclusion is supported by similar findings by Caggiano and Azmi et al. [155, 156].

4.3.6 Fatigue on Macro-specimen vs. Micro-specimen

Table 4.9 presents summarised results between S-N curves of macro-specimens [3] and micro-specimens presented earlier in Section 3.3.2 and Section 4.2.1. Here, only 0° and 90° specimens tested under the same $R = 0.1$ stress ratio are considered.

The S-N curve gradient between 0° and 90° macro-specimens do not vary much in value, while a significant difference can be observed in the case of micro-specimens. This indicates fatigue response of macro-specimens which are insensitive to its microstructure

Table 4.9: Summarised S-N curve results for macro-specimens and micro-specimens.

Type	Macro-specimen		Micro-specimen	
Orientation	0°	90°	0°	90°
Gradient (MPa/cycles)	-0.0160	-0.0190	-0.2056	-0.0094
Intercept (MPa)	1096.1	5.0	1555.5	23.0
RMSE	0.0191	0.0585	0.1513	0.0583

and closer towards an average response of the material in general. In contrast, the fatigue response of micro-specimens is highly dependant on their local microstructure. A similar conclusion can be observed from the fatigue damage model material parameters (set of A and n) for both types of specimens. A fixed value of parameter n from Table 3.1 is sufficient to satisfactorily represent the gradient of all macro-specimens S-N curves presented in Section 3.3.2. Unlike in the case of micro-specimens, a significant difference in the value of parameter n between 0° specimens and the non-zero orientation specimens as presented in Table 4.6 is required to reproduce sufficiently the S-N curves for the respective orientation. This indicates that the fatigue damage model parameters depend heavily on the fibre orientation of the micro-specimens compared to that of macro-specimens. On the other hand, all of the non-zero orientation micro-specimens (30°, 45°, 60° and 90°) share a common parameter n value due to the small variation in the S-N curve gradient between these orientations.

The scatter of data for both specimens are represented by the value of RMSE. 90° orientation macro-specimens were found to have higher scatter than 0° orientation macro-specimens demonstrated by a higher value of RMSE. However, the difference in the RMSE value between these two orientations (macro-specimens) is not as big as the difference in value between two orientations of micro-specimens. 0° fibre orientation micro-specimens have the highest scatter compared to 90° orientation micro-specimens. This significant difference between macro-specimens and micro-specimens can be attributed to the higher level of material inhomogeneity within micro-specimens. The microstructure effect on micro-specimens is enhanced by their size, resulting in a significant variation between one specimen to another, compared to the macro-specimens. With a higher degree of anisotropic observed in UD micro-specimens, the effect of fibre orientation is more critical in micro-specimens compared to macro-specimens. This also explains the need for each orientation's individual fatigue damage model material parameters to describe better the effect of fibre orientation and size on micro-specimens. Interestingly, 90° orientation for both macro-specimens and micro-specimens have almost equal values of RMSE and share a similar level of scattering. This is probably due to the same dominant failure mechanism shared by the two types of specimens, fibre-matrix interface failure that similarly affect both macro- and micro-specimens.

Regarding the intercept value between both types of specimens, no qualitative difference can be noted. The different intercept values for macro-specimens and micro-specimens are only due to two different CFRP materials. Overall results of micro-specimens, in general, show comparable quality to the macro-specimens regardless of the challenges as-

sociated with preparing, handling and measuring the micro-specimens. This justifies the validity of the micro-fatigue test and supports the added advantage of this test over the standard test.

Even though more attention is required to identify the material parameters in the case of specimens with a higher degree of anisotropy, the current fatigue damage model formulation works well in fatigue life prediction for both macro and micro UD specimens. Whereas in the case of MD specimens where complex stress-strain states are involved, the current formulation can be further improved. Apart from the inadequate representation of the complex stress-strain state, CFRP's crucial failure mechanisms under fatigue loading need to be addressed to provide a complete picture in the analysis of fatigue damage computationally. Due to these reasons, a new mechanism-driven damage evolution model concept will be introduced in the following section to present a potential alternative of fatigue damage model for CFRP or similar materials.

4.3.7 Improved Formulation Based on Mechanism-Driven Damage Model

An idea of a potential alternative of fatigue damage model based on CFRP material's failure mechanisms is discussed here. This model is a two-dimensional elasticity model that is based on similar anisotropic damage presented earlier [3] derived from Matzenmiller et al. [124] combining a concept introduced by Maimí et al. [130, 131]. The inverse of the constitutive equation can be given by

$$\begin{pmatrix}\sigma_{11}\\ \sigma_{22}\\ \sigma_{12}\end{pmatrix} = \begin{pmatrix} \frac{(1-D_1)E_1}{1-(1-D_1)(1-D_2)\nu_{12}\nu_{21}} & \frac{(1-D_1)(1-D_2)E_1\nu_{21}}{1-(1-D_1)(1-D_2)\nu_{12}\nu_{21}} & 0 \\ \frac{(1-D_1)(1-D_2)E_2\nu_{12}}{1-(1-D_1)(1-D_2)\nu_{12}\nu_{21}} & \frac{(1-D_2)E_2}{1-(1-D_1)(1-D_2)\nu_{12}\nu_{21}} & 0 \\ 0 & 0 & (1-D_6)G_{12} \end{pmatrix} \begin{pmatrix}\varepsilon_{11}\\ \varepsilon_{22}\\ 2\varepsilon_{12}\end{pmatrix} \tag{4.4}$$

where E_i, ν_{ij} and G_{ij} are the elastic constants and $D_i \in [0,1]$ are the damage variables. The model reference coordinate is defined in relation to the fibre orientation with x_1 is the fibre direction. Three damage variables form the internal variable of the model with D_1 is associated with longitudinal fibre failure while D_2 corresponds to transverse matrix microcracking within the material. The third damage variable, D_6, on the other hand, is influenced by both transverse and longitudinal microcracks. Each of the damage variables varies $D_i = 0 \rightarrow 1$ to indicate damage evolution within the material until material failure.

Determination of active damage variables is necessary to consider different damage effects under tension and compression due to the unilateral effect caused by transverse microcrack closure from compressive loads. With an assumption that the primary dam-

age mechanism within the material is the microcrack formation, the damage variables are further divided into

$$D_1 = \begin{cases} D_{1+} & \text{for} \quad \varepsilon_{11} \geq 0 \\ D_{1-} & \text{for} \quad \varepsilon_{11} < 0 \end{cases} \tag{4.5a}$$

$$D_2 = \begin{cases} D_{2+} & \text{for} \quad \varepsilon_{22} \geq 0 \\ D_{2-} & \text{for} \quad \varepsilon_{22} < 0 \end{cases} \tag{4.5b}$$

The original model introduced by Maimí et al. [130, 131] distinguish between the tensile and compression loading mode based on the sign of the normal stress; however, the present idea suggests a strain-based definition to retain the physical meaning of microcrack opening under positive normal strain when loaded.

Surface-bound elastic domain. The accuracy of a damage model depends on its definition of elastic response domain that manages to capture complex stress-strain states within the material. In this model, the elastic domain is bound by four surfaces. Each surface defines one failure mechanism occurring in the composite material using a set of standard failure criteria. Since this model is formulated in a strain state, the failure envelope is also defined in strain space. Although most of the failure criteria available for composite is defined in terms of stress, as long as the material response is linearly elastic, reformulation of these failure criteria is possible. In this case, the nominal stress components can be computed using

$$\begin{pmatrix} \varepsilon_{11} \\ \varepsilon_{22} \\ 2\varepsilon_{12} \end{pmatrix} = \begin{pmatrix} \frac{1}{(1-D_1)E_1} & -\frac{\nu_{21}}{E_2} & 0 \\ -\frac{\nu_{12}}{E_2} & \frac{1}{(1-D_2)E_2} & 0 \\ 0 & 0 & \frac{1}{(1-D_6)E_6} \end{pmatrix} \begin{pmatrix} \sigma_{11} \\ \sigma_{22} \\ \sigma_{12} \end{pmatrix} \tag{4.6}$$

under the assumption that the material is undamaged ($D_i = 0$). The nominal stress components $\tilde{\sigma}_{ij}$ obtained previously is then utilised to define the surfaces that bounds the elastic domain. Despite damage accumulation during material deformation, these surfaces remain constant, supposedly to match the classical failure criteria. The LaRC03/04 criteria as presented in the original Maimí et al. model are used to define the failure envelopes [126–131] accounting for longitudinal and transverse fracture under tension and compression. The four surfaces outlining the elastic domain is given by Eq. (2.2) where F_i, $\Phi_i(\tilde{\sigma}_{ij}, R_i)$ and $r_i = 1$ are the damage activation functions, loading functions and elastic damage thresholds, respectively, whereas $\tilde{\sigma}_{ij}$ are the nominal stresses. The value of the elastic damage threshold r_i remain constant in this present model contrary to the one define in the original model.

Failure criteria. Four LaRC03/04 failure criteria are applied to the present model to define the surfaces [126–131] that bound the elastic domain. The first criterion is aimed at fibre tensile failure as described in Eq. (2.3) whereby fracture under this loading mode occur perpendicular to the fibre direction. In the case of compressive longitudinal failure, the material fails under the event of shear kinking and neighbouring matrix damage [130, 131, 157, 158] and the criteria defining the longitudinal compressive failure is expressed in Eq. (2.4). There are two types of transverse failure, in addition to the longitudinal failures mentioned above, that is applied to the present model. The first type is fracture perpendicular to the fibre direction with fracture angle $\alpha_0 = 0^\circ$. The failure criterion is given by Eq. (2.8) whereas, in the case where the material undergoes high transverse compressive stresses $\tilde{\sigma}_{22} < 0$ compared to the in-plane shear stress, where the loading closely resembles pure transverse compression, the fracture angle $\alpha_0 = 53^\circ$. The failure criterion for this case is given in Eq. (2.9). The surfaces that confine the elastic domain of this present model is similar to those presented in Figure 2.3.

Fatigue damage evolution. Combining the idea of the previous one-dimensional fatigue damage evolution that is based on microplastic work introduced earlier in Eq. (3.12) [1, 3] with the loading functions from Maimí et al. [130, 131], the newly defined one-dimensional fatigue damage evolution is given by

$$\mathrm{d}D = A\omega(D)\,\phi^n\,\mathrm{d}\phi \tag{4.7}$$

where A and n are material parameters and $\omega(D)$ is the warping function similarly as defined in Eq. (3.13),(3.14) and (3.15). With the new damage evolution equation, the five damage variables D_{1+}, D_{1-}, D_{2+}, D_{2-} and D_6 are assumed to be driven by the loading functions Φ_i. Note that the value of ϕ in Eq. (4.7) is always positive by itself and therefore does not require absolute sign as in the case of Eq. (3.12).

The relationship between the five damage variables D_{1+}, D_{1-}, D_{2+}, D_{2-} and D_6, with the loading functions Φ_{1+}, Φ_{1-}, Φ_{2+} and Φ_{2-}, are derived based on similar dependency of damage variables with the elastic damage thresholds r_{1+}, r_{1-}, r_{2+} and r_{2-} from the Maimí et al. model [130, 131]. Resulting in

$$\mathrm{d}D_{1+} = \begin{cases} A_{1+}\omega(D)\Phi_{1+}^{n_{1+}}\mathrm{d}\Phi_{1+} & \text{if } \mathrm{d}\Phi_{1+} \geq 0 \quad \text{and } \Phi_{1+} \geq \Phi_{1-} \\ A_{1-}\omega(D)\Phi_{1-}^{n_{1-}}\mathrm{d}\Phi_{1-} & \text{if } \mathrm{d}\Phi_{1-} \geq 0 \quad \text{and } \Phi_{1+} < \Phi_{1-} \\ 0 & \text{else} \end{cases} \tag{4.8a}$$

$$\mathrm{d}D_{1-} = \begin{cases} pA_{1+}\omega(D)\Phi_{1+}^{n_{1+}}\mathrm{d}\Phi_{1+} & \text{if } \mathrm{d}\Phi_{1+} \geq 0 \quad \text{and } \Phi_{1+} \geq \Phi_{1-} \\ A_{1-}\omega(D)\Phi_{1-}^{n_{1-}}\mathrm{d}\Phi_{1-} & \text{if } \mathrm{d}\Phi_{1-} \geq 0 \quad \text{and } \Phi_{1+} < \Phi_{1-} \\ 0 & \text{else} \end{cases} \tag{4.8b}$$

$$\mathrm{d}D_{2+} = \begin{cases} A_{2+}\omega(D)\Phi_{2+}^{n_{2+}}\mathrm{d}\Phi_{2+} & \text{if } \mathrm{d}\Phi_{2+} \geq 0 \quad \text{and } \Phi_{2+} \geq \Phi_{2-} \\ A_{2-}\omega(D)\Phi_{2-}^{n_{2-}}\mathrm{d}\Phi_{2-} & \text{if } \mathrm{d}\Phi_{2-} \geq 0 \quad \text{and } \Phi_{2+} < \Phi_{2-} \\ 0 & \text{else} \end{cases} \tag{4.8c}$$

$$\mathrm{d}D_{2-} = \begin{cases} A_{2-}\omega(D)\Phi_{2-}^{n_{2-}}\mathrm{d}\Phi_{2-} & \text{if } \mathrm{d}\Phi_{2-} \geq 0 \\ 0 & \text{else} \end{cases} \tag{4.8d}$$

$$\mathrm{d}D_{6} = \begin{cases} A_{1+}\omega(D)\Phi_{1+}^{n_{1+}}\mathrm{d}\Phi_{1+} & \text{if } \mathrm{d}\Phi_{1+} \geq 0 \quad \text{and } \Phi_{1+} \geq \Phi_{1-} \\ A_{1-}\omega(D)\Phi_{1-}^{n_{1-}}\mathrm{d}\Phi_{1-} & \text{if } \mathrm{d}\Phi_{1-} \geq 0 \quad \text{and } \Phi_{1+} < \Phi_{1-} \\ A_{6}\omega(D)\Phi_{2+}^{n_{6}}\mathrm{d}\Phi_{2+} & \text{if } \mathrm{d}\Phi_{2+} \geq 0 \quad \text{and } \Phi_{2+} \geq \Phi_{2-} \\ A_{6}\omega(D)\Phi_{2-}^{n_{6}}\mathrm{d}\Phi_{2-} & \text{if } \mathrm{d}\Phi_{2-} \geq 0 \quad \text{and } \Phi_{2+} < \Phi_{2-} \\ 0 & \text{else} \end{cases} \tag{4.8e}$$

In the above equations, $p = q\frac{E_1 - E_2}{E_1}$ where $q = 0$ when the broken fibres under compression are assumed to be still inline, and the original stiffness is unaffected, whereas $q = 1$ when the broken fibres no longer contribute to the stiffness of the material along with stiffness due to matrix closure. In the event when several conditions in Eq. (4.8e) is true, the summation of all of the components are to be taken as the effective damage evolutions. The suggested fatigue damage model comprises of 19 to 25 material parameters. The required parameters are four independent elastic constants (E_i, ν_{ij} and G_{ij}), six static strength parameters R_{ij}, five scaling parameters A, five exponents n, broken fibre stiffness factor q and four independent warping function parameters (a_I, a_{II}, D_I and D_{II}).

The new fatigue damage model approach discussed here offers several advantages. One of the advantages lies in the formulation of the strain-based model compared to the previous stress-based model [3]. This means that no local iteration is required to evaluate failure criteria since the strain variable obtained from the standard displacement-based FE method can be presently used. Besides that, the implementation of LaRC03/04 failure criteria [126–131] to define the elastic limit indirectly supplement the stress interaction effects to address complex stress-strain states. Moreover, all of the required material parameters for this new idea of fatigue damage model should be easily attainable through standard testing of CFRP material. However, in terms of its accuracy and effectiveness, this new fatigue damage model approach has to be studied further.

4.3.8 Advantages and Disadvantage of Micro-Fatigue Testing

Advantages of micro-fatigue testing. There are several notable advantages of micro-fatigue testing compared to the standard fatigue test on CFRP. The first one can be witnessed from the failure behaviour of longitudinal specimens tested under the micro-fatigue test. Almost all specimens broke within the gauge section with defined fibre fracture as the dominant failure mechanism. This is an exceptional result since it also supports the validity of the test, given that the typical standard specimen usually experiences breaking within the clamp area [9]. The test design also presents the ability to observe the onset damage within the material on fibre resolution during the test. This allows detailed study of the local effect, such as inhomogeneity, microcrack, and crack density, within the material. Since the micro-fatigue test involves testing a minimal amount of fibre content within the specimen, the test results provide an insight that is much closer to the material level response of CFRP. Whereas in standard testing, however, it is much closer to simple structure level response due to the size of the specimen [66]. These two different response levels are crucial as they greatly contribute to a different failure behaviour of the material itself. On structure level response, the material fails in a more brittle manner involving sudden rupture of the specimen. In contrast to the failure behaviour of a specimen closer to material level response, the damage in the material is more progressive. Consequently, a specimen with structure level response usually results in fragmentations of the specimen, with respect to the specimen size, once it breaks under the applied load [9, 67]. While completely different results obtained in the case of micro-specimens as fragmentation of specimens can be significantly eliminated, even in the case of 0° specimens. This is proven from the possibility to study the fracture surfaces of 0° specimens under SEM. On top of that, the versatility of the micro-test setup for its ability to test unlimited types of material promise great benefits to various material engineering fields [138, 140–142]. Especially in the study of composite material, standard testing often requires specimen adaptation in terms of overall specimen geometry [3], in order to capture effective load on different fibre orientation specimens. Brunbauer and Pinter [9], in their experiment, adapted the 0° UD specimens by reducing the thickness and width of the specimens to compensate for the high tensile loads on the fibres. The adjustments necessary for the standard specimen sometimes complicates the specimen loading. Moreover, it induces unwanted specimen breaking that affects the actual material behaviour. The microstructure inhomogeneity in micro-specimens opens a new avenue to an in-depth study of the material's crack path and propagation prediction. Methods to control microstructure inhomogeneity within micro-specimens can be further developed, greatly benefiting the composite field.

Disadvantages of micro-fatigue testing. Undeniably, there are several disadvantages of the micro-fatigue testing of CFRP materials. First is its high dependency on the specimen quality in preserving the accuracy of the test. The specimen quality is mainly corroborated by the material and specimen preparation process. Therefore, special attention to these processes is essential to achieve reliable results. Due to micro specimens size, tedious specimen preparation and handling are required throughout the process. This includes handling the specimen using a vacuum tweezer in most cases to protect the specimens' polished surfaces and many more. Nevertheless, these demands are undoubtedly considered normal, especially for a newly developed test method to extract additional information from the specimens. Micro-specimens pose a greater chance to exhibit higher variance in material response due to their high dependency on material characteristics. Lastly, higher scatter can also be expected when testing with micro-specimens. The specimen size effect can contribute to the scattering, introducing microstructure inhomogeneity from one specimen to another. Due to this reason, many tests are required for the results to reach a certain level of statistical confidence.

Chapter 5

Conclusions

Fatigue fracture mechanics of CFRP material is highly complex. Although standard testing guidelines offer a systematic analysis of this material, it provides information on how the material fails at a simple structural level (macro-level response) which do not encompass the material level response (micro-level response). Therefore, the micro-fatigue test is helpful to complement the existing available standards. The present study has successfully demonstrated this new test's capability on composite material whereby the test validity has been confirmed from the similarity between the fracture observation and surface to the specimens tested macroscopically. Even without the need for a tab attached to the specimens, longitudinal micro-specimens were found to break at the gauge section of the specimen with no sign of fragmentation as usually obtained in standard specimens. This allows fracture surface analysis even on the longitudinal specimens, unlike in standard testing.

The micro-fatigue test also enables in-situ observation of damage throughout the whole fatigue lifetime. This opens up a greater potential for an in-depth study of local effects in the material, especially because this method is not limited to only CFRP material. The present study has shown that it is possible to directly observe several critical phenomena that occur when CFRP is loaded under fatigue loading: (i) formation of multiple cracks,

(ii) crack branching, (iii) crack initiation and propagation in the different microstructural region of the specimen (fibre-rich region and matrix-rich region), (iv) crack path pattern, (v) crack damping in the matrix-rich region as indication of redistribution of stresses, (vi) effect on crack initiation and propagation around foreign artefact within the material and finally, (vii) influence of fibre volume fraction on final specimen failure. Given all of these advantages, the micro-fatigue test certainly provides the ability to test CFRP closer to its material level. This method gives the insight to understand better, manage, and design CFRP structures to reach their optimum mechanical performance in fatigue. Furthermore, this will help formulate a more accurate material model to allow better material response prediction and minimise CFRP fatigue performance dependency on various levels.

The accuracy of micro-fatigue test results depends highly on the quality of the micro-specimens due to the specimen preparation process. Although the current development of the specimen preparation process has been shown to produce reliable specimens quality, it is still a tedious process. Further optimisation of the procedures is naturally the best way to reduce manufacturing defects within the specimen. Consequently, this would increase the quality of the specimens. This should further reduce scattering in test results and lower the need for a large amount of test data to achieve a reasonable statistical confidence level. To better understand factors affecting fatigue, the micro-fatigue test can be extended further under different conditions, such as studying frequency, temperature, stress ratio effects, and many more. It could also be extended for various types of loading, making this test a versatile tool to study any material closer to its micro-level response.

From the aspect of fatigue damage modelling, a new CDM model for fatigue and degradation of CFRP has been proposed. The model is formulated based on anisotropic linear elastic Hooke's law brittle model. It involves three damage variables, each representing damage effect with respect to the three coordinate axes. With the absence of independent shear damage variables, the number of damage variables and parameters could be kept at a minimal amount. The formulation concept based on the dissipation of microplastic work within the material gives a physical sense of how the damage evolves in CFRP under fatigue. The model is numerically efficient due to the estimation of microplastic work from the elastic components of stress and strain. The damage evolution depends on the stress increment, and the actual stress level with its formulation ensures a linear relationship obtained in the double log Wöhler diagram. Due to the direct relation to the S-N curves, all of the material parameters involved in the model can be easily determined. The model has been implemented in the Abaqus user-subroutine. With explicit time integration, the source of nonlinearity in the model comes only from the damage evolution. Furthermore,

this results in a numerically efficient implementation of the model. As a result of using Miner's rule damage accumulation in the formulation, the model allows damage accumulation during the stage of post-processing stress analysis without the effect of damage. This further enhances its numerical efficiency. The model has been validated against filament wound carbon fibre epoxy matrix composite. The model proves a satisfactory prediction for the case of UD and MD under tension, compression and alternating cyclic loading. Moreover, the model has also been successfully validated against UD micro-specimens under tension-tension fatigue load, which indicates the model capability to accurately predict the fatigue lifetime of CFRP material at both macro and micro-level response. Aside from that, the model also allows fatigue degradation and failure assessment at the material level response by considering the effect of damage on material stiffness locally. Additionally, the model is also applicable to static failure.

The present model, unfortunately, has some drawbacks. Firstly, discrimination on a different loading mode, tension and compression, is done based on stress. In this case, a strain-based division is more physical, whereby the microcrack opening effect during the positive value of strain is naturally considered. Apart from that, the stress-based model formulation requires local iteration during the evaluation of failure criteria. On top of that, the stress interactions effects common in describing failure mechanistic of CFRP are ineffectively represented. Therefore, another two-dimensional fatigue damage model as a possible alternative has been proposed.

The new approach of fatigue damage model maintains a similar brittle model based on anisotropic linear elastic Hooke's law in two-dimensional. It also applies the concept introduced by Maimí et al. Since the new model is formulated in strain-based, no local iteration is required to evaluate the failure criteria as strain variable can be employed directly from the standard displacement-based FE method. The new model comprises five damage variables as the internal variable of the model, considering longitudinal crack and transverse crack applied under two different types of loading, and another featuring influence from both. In an attempt to address the complex stress-strain state, the elastic limit is defined by the implementation of failure criteria originally by LaRC03/04. These criteria relate the elastic limit to failure mechanisms of CFRP under respective loading, thereby including the stress interaction effects. All of the projected material parameters for this fatigue damage model should be easily attainable through the standard testing scheme of CFRP material. However, this approach's effectiveness and accuracy have to be tested in the future. Nevertheless, this idea offers high potential in developing a reliable, realistic and systematic CFRP fatigue damage model.

In conclusion, the presented experimental and modelling approaches offer promising opportunities to study fatigue damage evolution in CFRP closer to the material level. This will provide accurate insight to understand the fracture mechanism better and manage and design CFRP towards reaching its optimum mechanical performance.

Appendices

Appendix A

Micro-fatigue Experimental Guidelines

Preparing the setup. To begin the test, three essential data need to be saved. These data are frequency, number of cycles, and all control parameters. It must be ensured that both half parts of the clamping system (where the specimens will be placed later) are correctly aligned and at the same height. This can be done optically through the live feed camera linked to the telecentric lens via the NI-Max software from National Instrument, USA. The motor displacement needs to be adjusted so that one side of the clamping system on the right side of the setup can be moved towards the other part on the left side. Since a telecentric lens is used and the magnification objective is fixed, this step is necessary to make sure that both sides of the clamp are visible. The right side of the clamp attached to the piezoelectric actuator and motor is treated as the reference, whereas the left side of the clamp is then adjusted to match the height and the alignment of the right side clamp. The triangular grooves on both sides of the clamps are used as guidance in this process, as displayed in Figure A.1. **Important:** It is possible that both sides of the clamp could crash together when the clamp's right side approaches the left side. This would cause the *permanent loadcell failure*. In order to avoid this, *an automatic stop*, triggered by the maximum force exerted by the contact of both sides, must be set prior to the alignment. A typical value is about 1% of the loadcell maximum load. If the clamps are about to touch

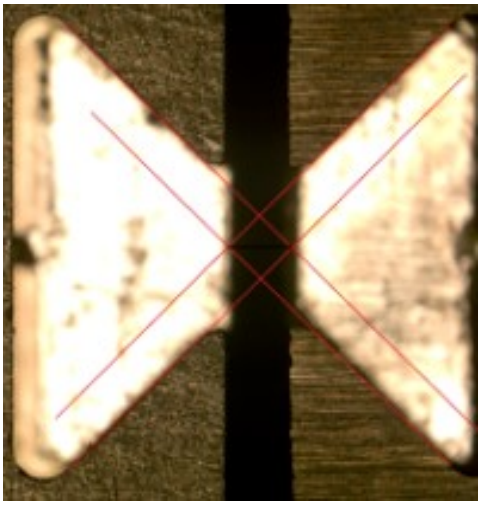

Figure A.1: Triangular grooves on both side of the clamp are matched optically to ensure proper alignment before the micro-fatigue test started.

each other while exerting a small force, further movement can already be stopped to avoid the crash impact on the loadcell. This is particularly beneficial when loadcell of smaller capacity is used. It is essential also to make sure that there are no dust particles in the vicinity of the test setup, especially inside the clamp grooves. This can be achieved by using compressed air dusters. An aluminium plate of thickness 0.2 mm in the shape of triangular grooves of the clamp is then placed inside each side of the clamp groove. The plate on both sides of the clamp acts as a bottom cushion to compensate for the slight specimen movement later when the clamp is tightened. The height on both sides of the clamps needs to be adjusted as necessary.

Setting preload conditions. In order to set the operating range as preload conditions, input the amount of preload (in volts) that corresponds to the respective load, taking into consideration the loadcell offset voltage as the maximum stop triggered voltage. To avoid loadcell overloading, the minimum stop triggered voltage is also prescribed. These settings define the allowable operating range of the setup during the preload of the specimen. After that, the setup is set to match the specimen insert position by adjusting the motor displacement to match the insert position of the specimen. The piezoelectric actuator target is then set to the middle range of the operating voltage. This allows enough variation in the piezoelectric actuator signal during loading so that the stop triggered setting will not be quickly prompted. Here, the value used throughout the test was set to 5 V. The specimen is then placed in the triangular groove of the clamp. The next step is to move the motor to apply load to the specimen. The velocity of the motor is set to be at 0.001 mm/s. The sample is now on preload, and the loading will stop automatically once the maximum load is reached or the specimen breaks. In the latter case, a stop will be triggered when the minimum load

exceeds the earlier range. The preload value is minimal not to induce premature damage on the specimen while it helps the specimen self-align itself within the clamp. It is crucial to ensure that the specimen is straight. This can be done by checking the distance between the specimen and clamp edges. The first picture of the specimen under preload is saved. This should always be done before the test starts. Afterwards, aluminium plates of 0.1 mm thickness are placed in each triangular groove on each side of the clamp. The plate on both sides of the clamp acts as the top cushion to compensate for the slight specimen movement later when the clamp is tightened. Once the aluminium plates are placed, the grips are fixed to secure the specimen. The grips need to be placed carefully *without exerting any force* on the specimen directly to avoid the specimen from breaking. Due to the brittle nature of the specimen, great attention is required in this step. The loadcell offset voltage values must be monitored continuously to know how much force is experienced by the specimen during this process. The screws on the grip need to be delicately tightened.

Setting actual test conditions. Once the preloading stage is completed, and the specimen grip is secured, all of the necessary input parameters are entered into the host program. The parameters required here are the target amplitude, mean stress, maximum and minimum offset tolerance, and maximum stop amplitude. The value used for maximum and minimum offset tolerance provides threshold constraints to limit the fluctuation response of the specimen under applied sinusoidal load so that the specimen response stays within the target range. Too strict threshold constraint value, especially at the beginning of the loading when the specimen responds most abruptly, could cause the specimen to break. Therefore, it is essential to tighten the constraint gradually as the specimen equilibrates and adapt it to the applied load signal. The value is defined as 0.1 at the beginning of the load for both the positive and the negative offset. The maximum stop amplitude is the allowable relative amplitude deviation for stop, and this value is set to be 100. The mean stress value is used to input the maximum stop triggered control value.

The other parameters required in the program are the PID and data acquisition parameters. There is a set of three PID parameters with respect to amplitude control and offset control, respectively. The only important parameters within this set are the P (Kc) parameter for amplitude and offset. The P parameter for amplitude control is set to be 0.02 Kc while the offset control is set to be -0.01 Kc. The frequency set for data acquisition in this test is 3000 Hz. Following this, the start wave load control parameters are supplied to the program. These parameters are important to minimise the instability fluctuation response from the specimens under applied load. The rest time for the start wave is 1000 s, the positive and negative tolerance of the start wave is 0.08, the amplitude of the start wave is 0.05,

while the positive and negative frequency tolerance of the start wave is 0.05. The next step is to load the specimen at the mean stress value. The load history figure that displays load over total piezoelectric actuator displacement, including motor displacement, is updated before the motor is set to move until the stress applied to the specimen reaches the mean stress. The motor movement will stop automatically once the mean stress is reached since the mean stress is input as the maximum stop triggered control value.

All motor logs can be stored by checking an option for storing, and a file will be created in the work folder. This option is particularly important when the tested specimen requires large deformation where both piezoelectric actuator and motor are required to assign necessary displacement. Therefore, this option is not compulsory. The maximum stop triggered value is now set to the actual maximum load value. The value is set by considering the maximum peak load value with permissible relative overload (set to be at 1.08) and the loadcell offset voltage. If the motor is required for the test, the motor speed for controlling the load offset is 2 mm/s. This step, however, is not important if the force will only be applied through piezoelectric actuator displacement. A picture of the specimen's front surface under preload at this stage should be captured. The appropriate image size can be set to minimise memory allocation for picture storage throughout the test. All of the required settings are then saved. The photo program to record the specimen images is now started. Periodic images stored throughout the test are taken from the Labview photo software, and this software requires the NI-MAX photo software session to be terminated.

The image frequency and the work folder path for where the images will be stored are required in this stage. Several trial images are taken until the quality of the images taken are satisfactory. The frequency of the images taken is set to be 1 picture/min. Once the quality of the pictures is satisfactory, the photo program is started. From this moment onwards, the load data log will be recorded. For the test presented in Chapter 4, only a piezoelectric actuator will be used for force application to the specimen. Therefore, the motor control tab is switched off at this point. This is possible because the specimens tested in this micro-fatigue test do not require large deformation. Therefore, the travel range of the piezoelectric actuator is sufficient, and the motor is no longer necessary. The final step to this stage is applying the specimen's load. This is done by selecting the load control tab and pressing the start wave button to apply the sinusoidal load onto the specimens. The test is now started.

Adjustment during the test. The maximum and minimum offset tolerance values have to be adjusted to stabilise the specimen's fluctuation response under applied sinusoidal load. These values are gradually adjusted towards the value of 0.01, together with one of the

PID offset parameters, P. The usual value used for P offset is -0.01 Kc. Once the specimen response is stabilised, no other parameter adjustment is required.

Stopping the test. Once the specimen is broken, the running program can be closed. The sequence to end the micro-fatigue test starts by stopping the photo program, the software to write the load data log, and the motor (in the case whereby the motor is used together with a piezoelectric actuator). A broken specimen picture at the end of the test is saved before removing it from the clamps. Next, the load control tab is switched off, and the piezoelectric actuator control value is set back to 0 V. Before switching off the test setup, the motor control tab must be switched on again to allow the motor to be set to a safety position. This position is set at 25 mm. This is a safety measure to avoid any possible collision.

Appendix B

Design of Fixtures

Design of fixtures. Several milling fixtures have been developed throughout this study to optimise the quality of the micro-specimens obtained. Figure B.1 presents four different milling fixtures, with each designed successively up to the final fixture (see Figure B.1d) used in the final preparation of the micro-specimen. Figure B.1a presents the very first design of a fixture made of non-corrosive metal with six micro-specimen forms and guidelines milled on it. Due to the size of the micro-specimen that contributes to the difficulty of aligning the strip to properly follow the geometry of the specimen manually, the three guidelines to mark the centre, top and bottom of the specimen is necessary. In the case of preparing off-axis specimens, it is essential to ensure that the gauge sections of the specimens are made out of one single fibre bundle to ensure uniform stress distribution within the gauge section during fatigue loading. Figure B.2 shows an example of a specimen microstructure that we try to avoid in order to ensure that specimen fracture will remain only within the gauge section. Due to this reason, the second fixture, as shown in Figure B.1b, was designed using poly(methyl methacrylate) (PMMA). This material is chosen due to its transparent characteristic, which allows visible light transmission through it. The borders of each geometry form milled on the fixture were painted black, and only the specimen's geometry is left unconcealed. A light source is then placed at the

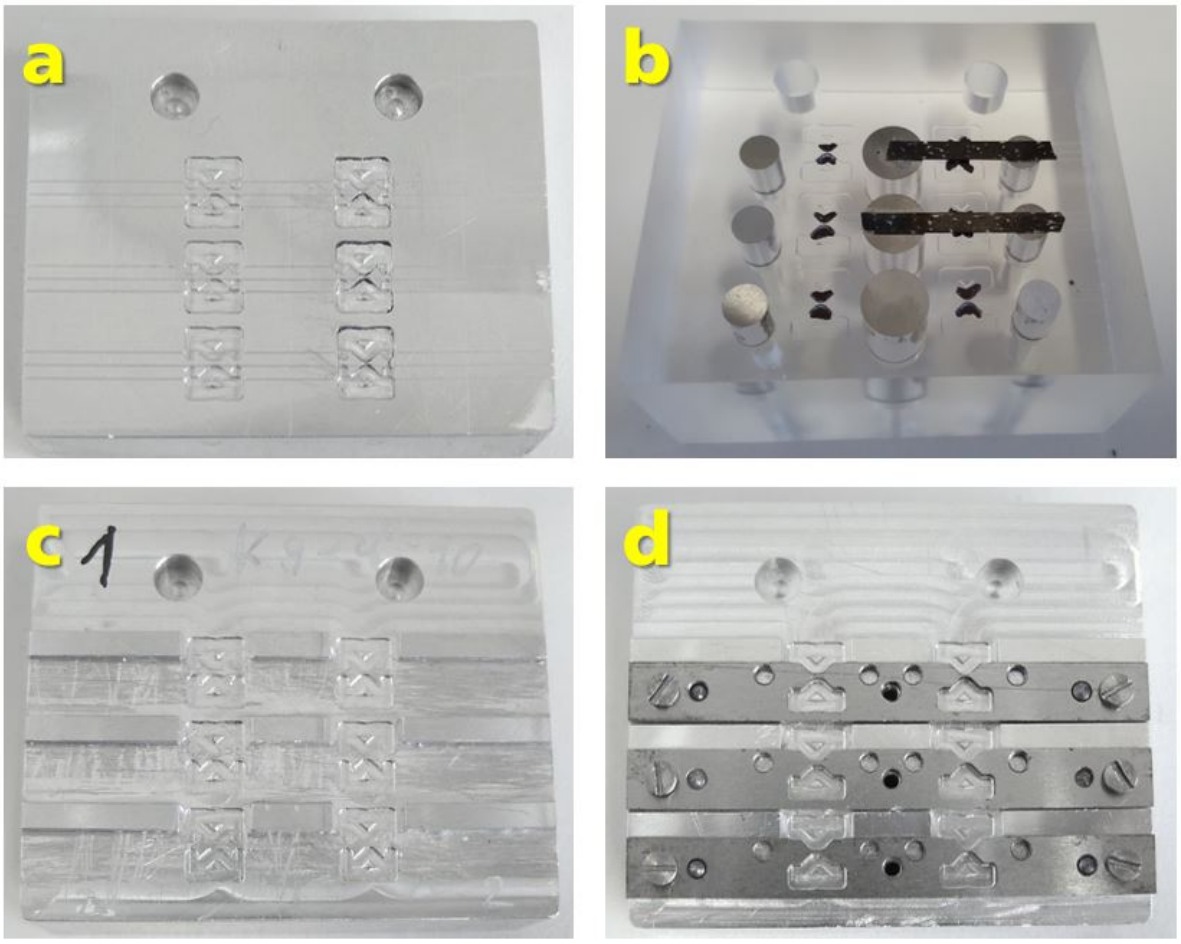

Figure B.1: Design of fixtures to further improve quality of micro-specimen.

bottom of the fixture while attaching the strips to the fixture. This makes it possible to view the geometry pattern through the material strips, thereby facilitating the alignment of the strip to be exact. The chemical reaction between CA glue with PMMA is known to leave a haze-mark on PMMA. This, unfortunately, will affect the transparency of the PMMA fixture block over a period of time. To preserve the PMMA fixture for long-term usage, nine metal plugs are inserted in the fixture block at the point where CA glue is usually applied to attach the strip. CA glue stain could also be easily removed with these plugs whenever the fixture needs to be cleaned and reused.

Despite the advantage the PMMA fixture offers, it is not cost-effective in terms of manufacturability and durability. Hence, a cheaper alternative is acquired from the subsequent design of fixture in Figure B.1c. The main difference between this fixture and the previous PMMA fixture is that we no longer rely on using a light source during the strip attachment; instead, the placement of the strip can be done under a stereomicroscope. Since the fixture is now made of non-corrosive metal, similarly to a fixture in Figure B.1a, it is more

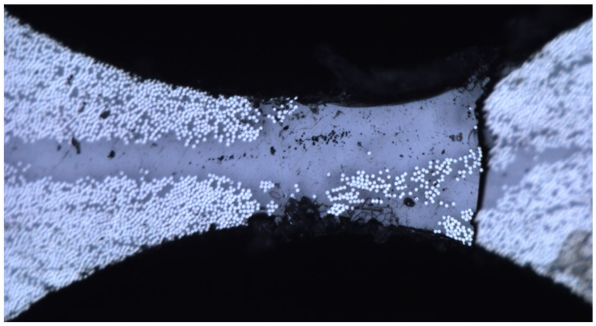

Figure B.2: Example of a specimen with gauge section outside of one fibre bundle.

economical and durable. The guidelines from both previous fixtures are now replaced with a stopper to facilitate the alignment of the strip. One common problem observed in the final specimens from all of these three fixture designs, although more critical in the first two earlier fixture designs (Figure B.1a and b), is the strip bending effect during the process of milling. The strip bending causes the specimen extracted to have variation in its width within the gauge section. This variation ranges between 11 up to 38% in the case where it is most severe. Although adding a stopper in the third fixture slightly minimises this effect in the specimens, it does not eliminate it. As a result, almost 15% of specimens extracted needs to be discarded. Although the stopper works fine on the chosen material for this project, this stopper could pose as a disadvantage in the case where the strip is wider than 3.5 mm, as it limits the ability to adjust the strip vertically in order to find the best position on the strip for the specimen extraction.

Further improvement on the fixture to eliminate bending in the strip during the milling process results in the final design of the fixture as displayed in Figure B.1d. A significant feature added to the design of the third fixture to produce the final fixture is a pressing plate secured by metal pins and screws. This pressing plate is secured on the glued strip before the fixture is sent for milling. There are in total two pins, one for each end of the pressing plate, used to maintain the alignment and position of the plate during the whole process of milling. The pressing plate is secured tightly with a screw on both ends and middle of the pressing plate. The screw, however, needs to be carefully tightened by balancing the pressure on the glued strip to ensure that the strip will not be deflected. Deflection often causes the strip to break due to its brittle nature. It is also important to ensure that the order of the pressing plate is maintained and not interchangeable between one row to another. This is because the pressing plates are machined with high precision, and therefore, changing the pressing plate from its designated position would affect the fitting between the pressing plate and the slot. Therefore, the pressing plates are always permanently labelled using laboratory engraving tools to retain their position. The incorporation of this press-

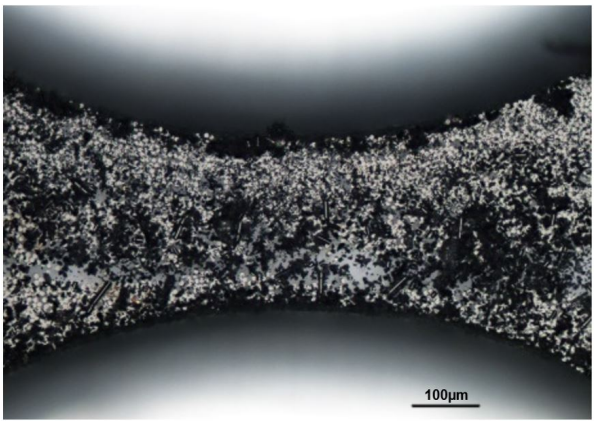

Figure B.3: Discarded specimen due to friction between strip and pressing plate.

ing plate certainly helps eliminate the bending of the strip during milling, evidently from the extracted specimens that show no variation of width within the gauge section. Unfortunately, the surface quality of the strips is badly affected due to the friction between the strip top surface and the pressing plate surface that is in contact. Figure B.3 shows one of the specimens that have to be rejected due to the friction effect introduced by the pressing plate onto the top strip surface. Severe scratches on the specimen surface kill the possibility of having in-situ observation of failure mechanism on the specimen during the test and seriously compromise the overall strength of the specimen. Most of the specimens already contain a critical number of microcracks, with some completely broken. As a remedy to this, all three fixture pressing plates must be polished before being used.

Appendix C

Micro-Fatigue Result Data

Table C.1: Specimen dimensions and results of micro-fatigue test for 0° orientation specimens.

Specimen	Thickness (μm)	Stress Amplitude (MPa)	No. of Cycle to Failure
AFT3-0-3-2*	239.81	80	348,021
AFT5-0-7-1*	132.16	90	170,219
AFT3-0-5-4*	262.21	100	72,658
AFT3-0-3-1*	214.46	135	358,384
AFT3-0-8-5*	150.14	180	385,859
AFT5-0-4-3*	161.72	220	35,788
AFT1-0-2-1*	150.14	225	49,539

* Valid specimens that are included in the S-N curves in Section 4.2.1.

Table C.2: Specimen dimensions and results of micro-fatigue test for 30° orientation specimens.

Specimen	Thickness (μm)	Stress Amplitude (MPa)	No. of Cycle to Failure
AFT7-30-11-02*	177.04	15	805,726
AFT8-30-05-02*	173.66	15	1,466,028
AFT7-30-07-02*	203.63	20	1,607,478
AFT7-30-03-02*	200.41	25	2,442,643
AFT8-30-05-01*	166.97	26	236,731
AFT7-30-13-02*	174.52	27	1,682,448
AFT7-30-12-01*	115.41	27.5	4,128
AFT7-30-04-02*	180.65	28	2,494,023
AFT7-30-08-02*	205.11	30	1,360
AFT7-30-05-01*	246.86	30	636
AFT7-30-06-02*	138.91	32	1,760,383
AFT7-30-02-01*	167.50	34	3,677
AFT7-30-04-01*	274.04	35	1,624,813
AFT7-30-14-01*	179.20	36	450,436
AFT7-30-14-02*	121.49	37	13,751
AFT7-30-18-01*	141.25	38	2,035
AFT7-30-17-01*	122.80	39	96,753
AFT7-30-18-02*	233.23	43	1,446
AFT7-30-06-01	276.72	28	-
AFT7-30-06-03	207.82	37	-
AFT7-30-10-01	115.56	40	-

* Valid specimens that are included in the S-N curves in Section 4.2.1.

Table C.3: Specimen dimensions and results of micro-fatigue test for 45° orientation specimens.

Specimen	Thickness (μm)	Stress Amplitude (MPa)	No. of Cycle to Failure
AFT10-45-03-01*	131.14	20	1,703,182
AFT9-45-16-01*	122.14	24	1,461,078
AFT10-45-06-01*	189.96	24.5	75,405
AFT9-45-10-01*	160.14	25	1,336,828
AFT10-45-02-01*	197.52	25.5	1,500
AFT9-45-04-01*	229.68	26	1,596,978
AFT10-45-01-01*	123.97	26.2	190
AFT9-45-09-01*	139.31	26.3	285
AFT9-45-05-01*	260.06	28	99,153
AFT9-45-11-01	145.62	15	-
AFT10-45-07-02	150.07	20.5	-
AFT10-45-01-02	146.73	21	-
AFT10-45-10-01	171.52	22	-
AFT9-45-09-02	110.97	23	-
AFT10-45-09-01	172.10	25	-
AFT10-45-06-02	123.31	26.5	-
AFT9-45-07-01	190.31	27	-
AFT9-45-07-02	199.07	27	-
AFT10-45-09-02	196.59	27	-
AFT9-45-12-01	244.15	28	-
AFT9-45-06-01	119.59	28.5	-
AFT9-45-13-01	170.76	29	-
AFT10-45-03-02	136.35	30	-
AFT9-45-02-01	194.67	30	-

* Valid specimens that are included in the S-N curves in Section 4.2.1.

Table C.4: Specimen dimensions and results of micro-fatigue test for 60° orientation specimens.

Specimen	Thickness (μm)	Stress Amplitude (MPa)	No. of Cycle to Failure
AFT6-60-09-01*	103.51	19	1,595,653
AFT6-60-08-02*	193.73	23	33,888
AFT6-60-05-01*	191.12	24	36,791
AFT6-60-07-01*	169.34	26	396,471
AFT11-60-02-01*	158.34	27	268,606
AFT6-60-13-01*	142.08	27.5	615,651
AFT6-60-11-01*	164.60	28.5	914,758
AFT6-60-10-01*	157.02	29.5	101,988
AFT6-60-03-01	202.55	18	-
AFT6-60-16-02	203.58	20	-
AFT6-60-14-01	179.21	25	-
AFT6-60-06-01	117.36	25	-
AFT11-60-02-02	125.03	28	-
AFT6-60-08-01	126.45	28.5	-
AFT6-60-11-02	232.71	31	-
AFT6-60-09-02	197.25	32	-

* Valid specimens that are included in the S-N curves in Section 4.2.1.

Table C.5: Specimen dimensions and results of micro-fatigue test for 90° orientation specimens.

Specimen	Thickness (μm)	Stress Amplitude (MPa)	No. of Cycle to Failure
AFT3-90-02-01*	194.63	16	20,918
AFT3-90-01-03*	114.33	20	136,588
AFT2-90-06 -01*	137.33	20.5	1,006,403
AFT3-90-13 -01*	228.24	21	6,088
AFT3-90-04 -01*	191.05	22	900
AFT2-90-09 -01*	256.61	22.5	8,093
AFT2-90-06 -02*	178.46	26	33,408
AFT3-90-11-01	179.48	6.8	-
AFT4-90-01-01	187.88	13.5	-
AFT2-90-10 -01	137.05	17	-
AFT3-90-01-01	150.90	18	-
AFT2-90-11 -01	264.46	19	-
AFT3-90-03-02	188.98	20	-
AFT3-90-10 -01	187.67	24	-

* Valid specimens that are included in the S-N curves in Section 4.2.1.

Bibliography

Bibliography

[1] J. Hohe, M. Gall, H. Gauch, S. Fliegener, and Z.M. Abdul Hamid. A material model for prediction of fatigue damage and degradation of CFRP materials. In *21st Symposium on Composites, Bremen, Germany*, Key Engineering Materials, pages 740–744. Trans Tech Publications Ltd., Stafa-Zurich, Switzerland, 2017.

[2] Z.M. Abdul Hamid, J. Hohe, M. Gall, S. Fliegener, and P. Gumbsch. Fatigue damage and degradation model for carbon fibre reinforced polymer materials. *PAMM*, 17: 259–260, 2017.

[3] J. Hohe, M. Gall, S. Fliegener, and Z.M. Abdul Hamid. A continuum damage mechanics model for fatigue and degradation of fiber reinforced materials. *Journal of Composite Materials*, 54:2837–2852, 2020.

[4] G. Marsh. Airbus A350XWB update. *Reinforced Plastics*, 54:20–24, 2010.

[5] P.T. Curtis. *A review of the fatigue of composite materials*. Royal Aircraft Establishment, Farnborough, UK, 1987.

[6] M.T.A. Ansari, K.K. Singh, and M.S. Azam. Fatigue damage analysis of fiber-reinforced polymer composites - a review. *Journal of Reinforced Plastics and Composites*, 37:636–654, 2018.

[7] P. Davies, G. Germain, B. Gaurier, A. Boisseau, and D. Perreux. Evaluation of the durability of composite tidal turbine blades. *Philosophical Transactions of the Royal Society A: Mathematical, Physical and Engineering Sciences*, 371:20120187, 2013.

[8] W. Van Paepegem. *Development and finite element implementation of a damage model for fatigue of fibre-reinforced polymers*. Ghent University Architectural and Engineering Press, Ghent, Belgium, 2002.

[9] J. Brunbauer and G. Pinter. Effects of mean stress and fibre volume content on the fatigue-induced damage mechanisms in CFRP. *International Journal of Fatigue*, 75: 28–38, 2015.

[10] M. Quaresimin and M. Ricotta. Fatigue response and damage evolution in 2D textile composites. In *Fatigue of Textile Composites*, Composites Science and Engineering, pages 193–221. Woodhead Publishing, Cambridge, UK, 2015.

[11] F.C. Campbell Jr. *Manufacturing processes for advanced composites*. Elsevier Science, Amsterdam, Netherlands, 2003.

[12] A.P. Mouritz, M.K. Bannister, P.J. Falzon, and K.H. Leong. Review of applications for advanced three-dimensional fibre textile composites. *Composites Part A: Applied Science and Manufacturing*, 30:1445–1461, 1999.

[13] P. Alam, D. Mamalis, C. Robert, C. Floreani, and C.M. Ó Brádaigh. The fatigue of carbon fibre reinforced plastics - a review. *Composites Part B: Engineering*, 166:555–579, 2019.

[14] L.C. Hollaway. A review of the present and future utilisation of FRP composites in the civil infrastructure with reference to their important in-service properties. *Construction and Building Materials*, 24:2419–2445, 2010. Special Issue on Fracture, Acoustic Emission and NDE in Concrete (KIFA-5).

[15] S. Wicaksono and G.B. Chai. A review of advances in fatigue and life prediction of fiber-reinforced composites. *Proceedings of the Institution of Mechanical Engineers, Part L: Journal of Materials: Design and Applications*, 227:179–195, 2013.

[16] E.K. Gamstedt and R. Talreja. Fatigue damage mechanisms in unidirectional carbon-fibre-reinforced plastics. *Journal of Materials Science*, 34:2535–2546, 1999.

[17] P.K. Mallick. *Fiber-reinforced composites-materials, manufacturing, and design*. CRC Press, Taylor & Francis Group, Boca Raton, USA, 1988.

[18] O. Konur and F.L. Matthews. Effect of the properties of the constituents on the fatigue performance of composites: A review. *Composites*, 20:317–328, 1989.

[19] S. DorMohammdi, C. Godines, F. Abdi, D. Huang, M. Repupilli, and L. Minnetyan. Damage-tolerant composite design principles for aircraft components under fatigue service loading using multi-scale progressive failure analysis. *Journal of Composite Materials*, 51:2181–2202, 2017.

[20] M.J. Owen and R.J. Howe. The accumulation of damage in a glass-reinforced plastic under tensile and fatigue loading. *Journal of Physics D: Applied Physics*, 5:1637–1649, 1972.

[21] H. Nouri, G. Lubineau, and D. Traudes. An experimental investigation of the effect of shear-induced diffuse damage on transverse cracking in carbon-fiber reinforced laminates. *Composite Structures*, 106:529–536, 2013.

[22] M. May and S.R. Hallett. Damage initiation in polymer matrix composites under high-cycle fatigue loading - a question of definition or a material property? *International Journal of Fatigue*, 87:59–62, 2016.

[23] A. Tabiei and W. Zhang. Composite laminate delamination simulation and experiment: A review of recent development. *Applied Mechanics Reviews*, 70(3):030801–23, 2018.

[24] ASTM E647-13. Standard test method for measurement of fatigue crack growth rates. ASTM International, West Conshohocken, USA, 2013.

[25] ASTM D6115-97. Standard test method for mode I fatigue delamination growth onset of unidirectional fiber reinforced polymer matrix composites. ASTM International, West Conshohocken, USA, 2011.

[26] Z. Wu, X. Wang, K. Iwashita, T. Sasaki, and Y. Hamaguchi. Tensile fatigue behaviour of FRP and hybrid FRP sheets. *Composites Part B: Engineering*, 41:396–402, 2010.

[27] M.J. Owen. *Fatigue of carbon-fiber-reinforced plastics*, pages 341–369. Elsevier, Amsterdam, Netherlands, 2016.

[28] H. El Kadi and F. Ellyin. Effect of stress ratio on the fatigue of unidirectional glass fibre/epoxy composite laminae. *Composites*, 25:917–924, 1994.

[29] C.J. Jones, R.F. Dickson, T. Adam, H. Reiter, and B. Harris. The environmental fatigue behaviour of reinforced plastics. *Proceedings of the Royal Society of London. A. Mathematical and Physical Sciences*, 396:315–338, 1984.

[30] J. Brunbauer, H. Stadler, and G. Pinter. Mechanical properties, fatigue damage and microstructure of carbon/epoxy laminates depending on fibre volume content. *International Journal of Fatigue*, 70:85–92, 2015.

[31] H. Masaki, O. Shojiro, C.G. Gustafson, and T. Keisuke. Effect of matrix resin on delamination fatigue crack growth in CFRP laminates. *Engineering Fracture Mechanics*, 49:35–47, 1994.

[32] T. Watanabe, Y. Takeichi, Y. Niwa, M. Hojo, and M. Kimura. Nanoscale in situ observations of crack initiation and propagation in carbon fiber/epoxy composites using synchrotron radiation x-ray computed tomography. *Composites Science and Technology*, 197:108244, 2020.

[33] S.B. Kumar, I. Sridhar, and S. Sivashanker. Influence of humid environment on the performance of high strength structural carbon fiber composites. *Materials Science and Engineering: A*, 498:174–178, 2008.

[34] R.A. Shenoi and J.F. Wellicome. *Composite Materials in Maritime Structures: Volume 1, Fundamental Aspects*. Cambridge University Press, Cambridge, UK, 1993.

[35] B. Harris, H. Reiter, T. Adam, R.F. Dickson, and G. Fernando. Fatigue behaviour of carbon fibre reinforced plastics. *Composites*, 21:232–242, 1990.

[36] R. Khan, R. Alderliesten, L. Yao, and R. Benedictus. Crack closure and fibre bridging during delamination growth in carbon fibre/epoxy laminates under mode I fatigue loading. *Composites Part A: Applied Science and Manufacturing*, 67:201–211, 2014.

[37] H. Zhuang and J.P. Wightman. The influence of surface properties on carbon fiber/epoxy matrix interfacial adhesion. *The Journal of Adhesion*, 62:213–245, 1997.

[38] D. Hull and T. Clyne. *An introduction to composite materials*. Cambridge University Press, Cambridge, UK, 2nd edition, 1996.

[39] M. Hojo, S. Matsuda, M. Tanaka, S. Ochiai, and A. Murakami. Mode I delamination fatigue properties of interlayer-toughened CF/epoxy laminates. *Composites Science and Technology*, 66:665–675, 2006.

[40] Z.M. Abdul Hamid, M. Florea, S. Fliegener, M. Schober, J. Hohe, and J. Rühe. Chemical modification of fiber-matrix interfaces of glass fiber reinforced thermoplastics and methods for interface characterization. *Advanced Engineering Materials*, 21: 1800590, 2019.

[41] S. Erden, K. Sever, Y. Seki, and M. Sarikanat. Enhancement of the mechanical properties of glass/polyester composites via matrix modification glass/polyester composite siloxane matrix modification. *Fibers and Polymers*, 11:732–737, 2010.

[42] N.J. Pagano and G.A. Schoeppner. 2.13 - Delamination of polymer matrix composites: Problems and assessment. In *Comprehensive Composite Materials*, pages 433–528. Pergamon, Oxford, UK, 2000.

[43] A. Bernasconi, P. Davoli, A. Basile, and A. Filippi. Effect of fibre orientation on the fatigue behaviour of a short glass fibre reinforced polyamide-6. *International Journal of Fatigue*, 29:199–208, 2007.

[44] V. Barron, M. Buggy, and N.H. McKenna. Frequency effects on the fatigue behaviour on carbon fibre reinforced polymer laminates. *Journal of Materials Science*, 36:1755–1761, 2001.

[45] L. Gornet, O. Wesphal, C. Burtin, J.L. Bailleul, P. Rozycki, and L. Stainier. Rapid determination of the high cycle fatigue limit curve of carbon fiber epoxy matrix composite laminates by thermography methodology: Tests and finite element simulations. *Procedia Engineering*, 66:697–704, 2013. International Conference Proceedings Fatigue Design 2013, Senlis, France.

[46] J. Montesano, Z. Fawaz, and H. Bougherara. Use of infrared thermography to investigate the fatigue behavior of a carbon fiber reinforced polymer composite. *Composite Structures*, 97:76–83, 2013.

[47] J. Paulo Davim, J. Campos Rubio, and A.M. Abrao. A novel approach based on digital image analysis to evaluate the delamination factor after drilling composite laminates. *Composites Science and Technology*, 67:1939–1945, 2007.

[48] L. Lasri, M. Nouari, and M. El Mansori. Wear resistance and induced cutting damage of aeronautical FRP components obtained by machining. *Wear*, 271:2542–2548, 2011.

[49] T. Wu, S.R. Tinkloh, T. Tröster, W. Zinn, and T. Niendorf. Determination and validation of residual stresses in CFRP/metal hybrid components using the incremental hole drilling method. *Journal of Composites Science*, 4:143, 2020.

[50] L. Liu, B.M. Zhang, D.F. Wang, and Z.J. Wu. Effects of cure cycles on void content and mechanical properties of composite laminates. *Composite Structures*, 73:303–309, 2006.

[51] B. Tavakol, P. Roozbehjavan, A. Ahmed, R. Das, R. Joven, H. Koushyar, A. Rodriguez, and B. Minaie. Prediction of residual stresses and distortion in carbon fiber-epoxy composite parts due to curing process using finite element analysis. *Journal of Applied Polymer Science*, 128:941–950, 2013.

[52] T.S. Mesogitis, A.A. Skordos, and A.C. Long. Uncertainty in the manufacturing of fibrous thermosetting composites: A review. *Composites Part A: Applied Science and Manufacturing*, 57:67–75, 2014.

[53] J. Varna, R. Joffe, L.A. Berglund, and T.S. Lundström. Effect of voids on failure mechanisms in RTM laminates. *Composites Science and Technology*, 53:241–249, 1995.

[54] S. Nonn, C. Kralovec, and M. Schagerl. Damage mechanisms under static and fatigue loading at locally compacted regions in a high pressure resin transfer molded carbon fiber non-crimp fabric. *Composites Part A: Applied Science and Manufacturing*, 115: 57–65, 2018.

[55] A. Zhang and D. Zhang. The mechanical property of CFRP laminates with voids. In *Advances in Materials and Materials Processing*, Advanced Materials Research, pages 25–28. Trans Tech Publications Ltd., Stafa-Zurich, Switzerland, 2013.

[56] S.F.M. de Almeida and Z.S.N. Neto. Effect of void content on the strength of composite laminates. *Composite Structures*, 28:139–148, 1994.

[57] S. Sisodia, K. Gamstedt, F. Edgren, and J. Varna. Effects of voids on quasi-static and tension fatigue behaviour of carbon-fibre composite laminates. *Journal of Composite Materials*, 49:2137–2148, 2015.

[58] C. Hiremath, K. Senthilnathan, A. Guha, and A. Tewari. Effect of volume fraction on damage accumulation for a lattice arrangement of fibers in CFRP. *Materials Today: Proceedings*, 2:2671–2678, 2015. 4th International Conference on Materials Processing and Characterization, Andhra Pradesh, India.

[59] J. Brunbauer, C. Gaier, and G. Pinter. Computational fatigue life prediction of continuously fibre reinforced multiaxial composites. *Composites Part B: Engineering*, 80:269–277, 2015.

[60] M. Kawai and N. Itoh. A failure-mode based anisomorphic constant life diagram for a unidirectional carbon/epoxy laminate under off-axis fatigue loading at room temperature. *Journal of Composite Materials*, 48:571–592, 2014.

[61] R.M. O'Higgins, M.A. McCarthy, and C.T. McCarthy. Comparison of open hole tension characteristics of high strength glass and carbon fibre-reinforced composite materials. *Composites Science and Technology*, 68:2770–2778, 2008.

[62] R.D.B. Sevenois and W. Van Paepegem. Fatigue damage modeling techniques for textile composites: Review and comparison with unidirectional composite modeling techniques. *Applied Mechanics Reviews*, 67(2):020802–12, 2015.

[63] DIN EN ISO 527-2:2012-06. Plastics - Determination of tensile properties - Part 2: Test conditions for moulding and extrusion plastics. Deutsches Institut für Normung e.V., Beuth Verlag GmbH, Berlin, Germany, 2012.

[64] ASTM D3479/D3479M-19. Standard test method for tension-tension fatigue of polymer matrix composite materials. ASTM International, West Conshohocken, USA, 2019.

[65] BS ISO 13003:2003. Fibre-reinforced plastics: Determination of fatigue properties under cyclic loading conditions. British Standards Institution (BSI), London, UK, 2004.

[66] J.T. Fong, ASTM International, American Society for Testing, and Materials. *What is fatigue damage?*, pages 243–266. ASTM International, West Conshohocken, USA, 1982.

[67] M. Kawai, S. Yajima, A. Hachinohe, and Y. Takano. Off-axis fatigue behavior of unidirectional carbon fiber-reinforced composites at room and high temperatures. *Journal of Composite Materials*, 35:545–576, 2001.

[68] A.L. Highsmith and K.L. Reifsnider. Stiffness-reduction mechanisms in composite laminates. In *Damage in Composite Materials: Basic mechanisms, accumulation, tolerance, and characterization*, pages 103–117. ASTM International, West Conshohocken, USA, 1982.

[69] J.A. Pascoe, R.C. Alderliesten, and R. Benedictus. Methods for the prediction of fatigue delamination growth in composites and adhesive bonds - a critical review. *Engineering Fracture Mechanics*, 112:72–96, 2013.

[70] J. Degrieck and W. Van Paepegem. Fatigue damage modeling of fibre-reinforced composite materials: Review. *Applied Mechanics Reviews*, 54:279–300, 2001.

[71] I.M. Daniel and A. Charewicz. Fatigue damage mechanisms and residual properties of graphite/epoxy laminates. *Engineering Fracture Mechanics*, 25:793–808, 1986.

[72] C.R. Kennedy, C.M. Brádaigh, and S.B. Leen. A multiaxial fatigue damage model for fibre reinforced polymer composites. *Composite Structures*, 106:201–210, 2013.

[73] P.M. Barnard, R.J. Butler, and P.T. Curtis. *Fatigue scatter of UD glass epoxy, a fact or fiction?*, pages 69–82. Springer, Dordrecht, Netherlands, 1985.

[74] W. Hwang and K.S. Han. Cumulative damage models and multi-stress fatigue life prediction. *Journal of Composite Materials*, 20:125–153, 1986.

[75] I.R. Farrow. *Damage accumulation and degradation of composite laminates under aircraft service loading: Assessment and prediction*. PhD thesis, Cranfield Institute of Technology, Cranfield, UK, 1989.

[76] A. Wöhler. Versuche zur Ermittelung auf die Eisenbahnwagen-Achseneinwirken der Kräfte und der Widerstands-fähigkeit der Wagen-Achsen (in German). *Zeitschrift für Bauwesen*, 10:583–616, 1860.

[77] M.A. Miner. Cumulative damage in fatigue. *Journal of Applied Mechanics*, 12:159–164, 1945.

[78] Z. Hashin and A. Rotem. A fatigue failure criterion for fiber reinforced materials. *Journal of Composite Materials*, 7:448–464, 1973.

[79] G.P. Sendeckyj. Fitting models to composite materials fatigue data. In *Test methods and design allowables for fibrous composites*, pages 245–260. ASTM International, West Conshohocken, USA, 1981.

[80] K.L. Reifsnider and Z. Gao. A micromechanics model for composites under fatigue loading. *International Journal of Fatigue*, 13:149–156, 1991.

[81] C.M.L. Wu. Thermal and mechanical fatigue analysis of CFRP laminates. *Composite Structures*, 25:339–344, 1993.

[82] Z. Fawaz and F. Ellyin. Fatigue failure model for fibre-reinforced materials under general loading conditions. *Journal of Composite Materials*, 28:1432–1451, 1994.

[83] J. Hartmann, E. Moosbrugger, and A. Büter. Variable amplitude loading with components made of short fiber reinforced polyamide 6.6. *Procedia Engineering*, 10: 2009–2015, 2011.

[84] M.H.R. Jen and C.H. Lee. Strength and life in thermoplastic composite laminates under static and fatigue loads. Part II: Formulation. *International Journal of Fatigue*, 20:617–629, 1998.

[85] I.P. Bond. Fatigue life prediction for GRP subjected to variable amplitude loading. *Composites Part A: Applied Science and Manufacturing*, 30:961–970, 1999.

[86] M. Gude, W. Hufenbach, I. Koch, and R. Protz. Fatigue failure criteria and degradation rules for composites under multiaxial loadings. *Mechanics of Composite Materials*, 42:443–450, 2006.

[87] N. Gathercole, H. Reiter, T. Adam, and B. Harris. Life prediction for fatigue of T800/5245 carbon-fibre composites: I. Constant-amplitude loading. *International Journal of Fatigue*, 16:523–532, 1994.

[88] T. Adam, N. Gathercole, H. Reiter, and B. Harris. Life prediction for fatigue of T800/5245 carbon-fibre composites: II. Variable-amplitude loading. *International Journal of Fatigue*, 16:533–547, 1994.

[89] B. Harris, N. Gathercole, J.A. Lee, H. Reiter, and T. Adam. Life-prediction for constant-stress fatigue in carbon-fibre composites. *Philosophical Transactions of the Royal Society of London. Series A: Mathematical, Physical and Engineering Sciences*, 355:1259–1294, 1997.

[90] S.V. Ramani and D.P. Williams. Notched and unnotched fatigue behavior of angle-ply graphite/epoxy composites. In *Symposium on Fatigue of Filamentary Composite Materials, Denver, USA*, page 27–46. ASTM International, West Conshohocken, USA, 1977.

[91] M. Kawai, Y. Matsuda, and R. Yoshimura. A general method for predicting temperature-dependent anisomorphic constant fatigue life diagram for a woven fabric carbon/epoxy laminate. *Composites Part A: Applied Science and Manufacturing*, 43:915–925, 2012.

[92] M.H. Beheshty and B. Harris. A constant-life model of fatigue behaviour for carbon-fibre composites: The effect of impact damage. *Composites Science and Technology*, 58:9–18, 1998.

[93] M.H. Beheshty, B. Harris, and T. Adam. An empirical fatigue-life model for high-performance fibre composites with and without impact damage. *Composites Part A: Applied Science and Manufacturing*, 30:971–987, 1999.

[94] J.R. Schaff and B.D. Davidson. Life prediction methodology for composite structures. Part I - Constant amplitude and two-stress level fatigue. *Journal of Composite Materials*, 31:128–157, 1997.

[95] J.C. Halpin, K.L. Jerina, and T.A. Johnson. Characterization of composites for the purpose of reliability evaluation. In *Analysis of the Test Methods for High Modulus Fibers and Composites*, ASTM STP 521, pages 5–64. ASTM International, 1973. A Symposium Presented at a Meeting of Committee D-30 on High Modulus Fibers and Their Composites, Texas, USA, 12-13 April 1972.

[96] H.A. Whitworth. Evaluation of the residual strength degradation in composite laminates under fatigue loading. *Composite Structures*, 48:261–264, 2000.

[97] A. Rotem. The fatigue behavior of composite laminates under various mean stresses. *Composite Structures*, 17:113–126, 1991.

[98] J.R. Schaff and B.D. Davidson. Life prediction methodology for composite structures. Part II - Spectrum fatigue. *Journal of Composite Materials*, 31:158–181, 1997.

[99] T.K. O'Brien and K.L. Reifsnider. Fatigue damage evaluation through stiffness measurements in boron-epoxy laminates. *Journal of Composite Materials*, 15:55–70, 1981.

[100] W. Hwang and K.S. Han. Fatigue of composites - fatigue modulus concept and life prediction. *Journal of Composite Materials*, 20:154–165, 1986.

[101] T.Y. Kam, K.H. Chu, and S.Y. Tsai. Fatigue reliability evaluation for composite laminates via a direct numerical integration technique. *International Journal of Solids and Structures*, 35:1411–1423, 1998.

[102] F. Sidoroff and B. Subagio. Fatigue damage modelling of composite materials from bending tests. In *Sixth International Conference on Composite Materials (ICCM-VI) & Second European Conference on Composite Materials (ECCM-II), London, UK*, pages 4–32. Elsevier, 1987.

[103] S. Vieillevigne, D. Jeulin, J. Renard, and N. Sicot. Modelling of the fatigue behaviour of a unidirectional glass epoxy composite submitted to fatigue loadings. In *International Conference on Fatigue of Composites. Proceedings, 3–5 June 1997, Paris, France*, pages 424–430. La Société Française de Métallurgie et de Matériaux, 1997.

[104] M. Kawai. Damage mechanics model for off-axis fatigue behavior of unidirectional carbon fiber-reinforced composites at room and high temperatures. In *Proceedings*

of the Twelfth International Conference on Composite Materials (ICCM-12). Paris, France, page 322. Citeseer, 1999.

[105] A. Fatemi and L. Yang. Cumulative fatigue damage and life prediction theories: A survey of the state of the art for homogeneous materials. *International Journal of Fatigue*, 20:9–34, 1998.

[106] Z. Khan, F.A. Al-Sulaiman, J.K. Farooqi, and M. Younas. Fatigue life predictions in woven carbon fabric/polyester composites based on modulus degradation. *Journal of Reinforced Plastics and Composites*, 20:377–398, 2001.

[107] M.M. Shokrieh and L.B. Lessard. Progressive fatigue damage modeling of composite materials, Part I: Modeling. *Journal of Composite Materials*, 34:1056–1080, 2000.

[108] M.M. Shokrieh and L.B. Lessard. Progressive fatigue damage modeling of composite materials, Part II: Material characterization and model verification. *Journal of Composite Materials*, 34:1081–1116, 2000.

[109] P. Papanikos, K.I. Tserpes, and S.P. Pantelakis. Modelling of fatigue damage progression and life of CFRP laminates. *Fatigue & Fracture of Engineering Materials & Structures*, 26:37–47, 2003.

[110] K.I. Tserpes, G. Labeas, P. Papanikos, and T. Kermanidis. Strength prediction of bolted joints in graphite/epoxy composite laminates. *Composites Part B: Engineering*, 33:521–529, 2002.

[111] A. Puck and H. Schürmann. Failure analysis of FRP laminates by means of physically based phenomenological models. *Composites Science and Technology*, 62:1633–1662, 2002.

[112] A. Puck, J. Kopp, and M. Knops. Guidelines for the determination of the parameters in Puck's action plane strength criterion. *Composites Science and Technology*, 62: 371–378, 2002.

[113] B. Mohammadi, B. Fazlali, and D. Salimi-Majd. Development of a continuum damage model for fatigue life prediction of laminated composites. *Composites Part A: Applied Science and Manufacturing*, 93:163–176, 2017.

[114] P.W. Harper and S.R. Hallett. A fatigue degradation law for cohesive interface elements - development and application to composite materials. *International Journal of Fatigue*, 32:1774–1787, 2010.

[115] M. May and S.R. Hallett. A combined model for initiation and propagation of damage under fatigue loading for cohesive interface elements. *Composites Part A: Applied Science and Manufacturing*, 41:1787–1796, 2010.

[116] C. Tao, J. Qiu, W. Yao, and H. Ji. A novel method for fatigue delamination simulation in composite laminates. *Composites Science and Technology*, 128:104–115, 2016.

[117] D.H. Allen, A.L. Highsmith, and D.C. Lo. *A continuum damage mechanics model for life prediction of laminated composites*, pages 119–128. Springer, Dordrecht, Netherlands, 1990.

[118] R. Talreja. *Damage mechanics of composite materials based on thermodynamics with internal variables*, pages 65–79. Springer, Dordrecht, Netherlands, 1990.

[119] P. Ladeveze. *A damage approach for composite structures: Theory and identification*, pages 44–57. Springer, Dordrecht, Netherlands, 1991.

[120] R. Talreja. A continuum mechanics characterization of damage in composite materials. *Proceedings of the Royal Society A. Mathematical, Physical and Engineering Sciences*, 399:195–216, 1985.

[121] R. Talreja. *A synergistic damage mechanics approach to durability of composite material systems*, pages 117–129. AA Balkema, Rotterdam, Netherlands, 1996.

[122] R. Talreja. Internal variable damage mechanics of composite materials. In *Yielding, Damage, and Failure of Anisotropic Solids*, volume 8 of *Proceedings of IUTAM/ICM Symposium 1987, Villard-de-Lans, France*, pages 509–533. Mechanical Engineering Publications, London, UK, 1990.

[123] S. Haojie, Y. Weixing, and W. Yitao. Synergistic damage mechanic model for stiffness properties of early fatigue damage in composite laminates. *Procedia Engineering*, 74:199–209, 2014.

[124] A. Matzenmiller, J. Lubliner, and R.L. Taylor. A constitutive model for anisotropic damage in fiber-composites. *Mechanics of Materials*, 20:125–152, 1995.

[125] R. Böhm, M. Gude, and W. Hufenbach. A phenomenologically based damage model for 2D and 3D-textile composites with non-crimp reinforcement. *Materials & Design*, 32:2532–2544, 2011.

[126] C.G. Dávila, P.P. Camanho, and C.A. Rose. Failure criteria for FRP laminates. *Journal of Composite Materials*, 39:323–345, 2005.

[127] S.T. Pinho, C.G. Dávila, P.P. Camanho, L. Iannucci, and P. Robinson. Failure models and criteria for FRP under-in-plane or three-dimensional stress states including shear non-linearity. Technical report, NASA Langley Research Center, Hampton, USA, 2005.

[128] S.T. Pinho, L. Iannucci, and P. Robinson. Physically-based failure models and criteria for laminated fibre-reinforced composites with emphasis on fibre kinking: Part I: Development. *Composites Part A: Applied Science and Manufacturing*, 37:63–73, 2006.

[129] S.T. Pinho, L. Iannucci, and P. Robinson. Physically based failure models and criteria for laminated fibre-reinforced composites with emphasis on fibre kinking. Part II: FE implementation. *Composites Part A: Applied Science and Manufacturing*, 37:766–777, 2006.

[130] P. Maimí, P.P. Camanho, J.A. Mayugo, and C.G. Dávila. A continuum damage model for composite laminates: Part I - Constitutive model. *Mechanics of Materials*, 39: 897–908, 2007.

[131] P. Maimí, P.P. Camanho, J.A. Mayugo, and C.G. Dávila. A continuum damage model for composite laminates: Part II - Computational implementation and validation. *Mechanics of Materials*, 39:909–919, 2007.

[132] L.M. Kachanov. *Introduction to continuum damage mechanics*. Mechanics of Elastic Stability. Springer Science & Business Media, Dordrecht, Netherlands, 1986.

[133] J. Lemaitre. *A course on damage mechanics*. Springer Verlag, Berlin, Germany, 1992.

[134] H. Gauch. Implementation and validation of a fatigue degradation model for carbon fiber reinforced plastics (in German). Master's thesis, Institute of Engineering Mechanics (ITM), Karlsruhe Institute of Technology (KIT) and Fraunhofer IWM, Karlsruhe, Germany, 2015.

[135] Karlsruhe Institute of Technology (KIT). RTM CAE/CAx – Aufbau einer durchgängigen CAE/CAx-Kette für das RTM-Verfahren vor dem Hintergrund der Herstellung von Hochleistungsfaserverbundwerkstoffen. Technical report, Institute of Vehicle System Technology (FAST), Karlsruhe Institute of Technology (KIT), Karlsruhe, Germany, 2014.

[136] Saertex® GmbH & Co. KG, Rev. 07/2011 EN 13473-1. SAERTEX GmbH & Co. KG, Germany, 2012.

[137] Biresin® CR170 and Biresin® CH150-3 Hardener, Version 7. Sika Deutschland GmbH, Germany, 2010.

[138] T. Kennerknecht. *Fatigue of micro molded materials-aluminum bronze and yttria stabilized zirconia*. PhD thesis, Karlsruhe Institute of Technology (KIT), Karlsruhe, Germany, 2014.

[139] S. Fliegener, T. Kennerknecht, and M. Kabel. Investigations into the damage mechanisms of glass fiber reinforced polypropylene based on micro specimens and precise models of their microstructure. *Composites Part B: Engineering*, 112:327–343, 2017.

[140] M. Buck, T. Straub, and C. Eberl. *Experimental investigation of damage detection and crack initiation up to the very high cycle fatigue regime*, pages 365–393. Springer Fachmedien Wiesbaden, Wiesbaden, Germany, 2018.

[141] C. Beckmann, T. Kennerknecht, J. Preußner, M. Farajian, M. Luke, and J. Hohe. Micromechanical investigation and numerical simulation of fatigue crack formation in welded joints. *Engineering Fracture Mechanics*, 198:142–157, 2018.

[142] S.A. Slaby, O. Kraft, and C. Eberl. Fatigue properties of conventionally manufactured and micro-powder-injection-moulded 17-4PH micro-components. *Fatigue & Fracture of Engineering Materials & Structures*, 39:780–789, 2016.

[143] Y. Miyano, M. Nakada, H. Kudoh, and R. Muki. Determination of tensile fatigue life of unidirectional CFRP specimens by strand testing. *Mechanics of Time-Dependent Materials*, 4:127–137, 2000.

[144] M. Nakada, Y. Miyano, M. Kinoshita, R. Koga, T. Okuya, and R. Muki. Time-temperature dependence of tensile strength of unidirectional CFRP. *Journal of Composite Materials*, 36:2567–2581, 2002.

[145] A.P. Vassilopoulos and T. Keller. *Experimental characterization of fiber-reinforced composite materials*, pages 25–67. Springer, London, UK, 2011.

[146] R.A. Grove and B.W. Smith. Compendium of post-failure analysis techniques for composite materials. Technical report, BOEING Military Airplane Co., Seattle, USA, 1987.

[147] E. Belmonte, M. De Monte, C.J. Hoffmann, and M. Quaresimin. Damage mechanisms in a short glass fiber reinforced polyamide under fatigue loading. *International Journal of Fatigue*, 94:145–157, 2017.

[148] S.J.W. Bass. AG14: Fractography of composites. Technical report, Group for Aeronautical Research and Technology in Europe GARTEUR, 1994.

[149] M.R. Kharrazi and S. Sarkani. Frequency-dependent fatigue damage accumulation in fiber-reinforced plastics. *Journal of Composite Materials*, 35:1924–1953, 2001.

[150] H. Zhang, E. Bilotti, and T. Peijs. The use of carbon nanotubes for damage sensing and structural health monitoring in laminated composites: A review. *Nanocomposites*, 1:167–184, 2015.

[151] A. Plumtree and L. Shi. Fatigue damage evolution in off-axis unidirectional CFRP. *International Journal of Fatigue*, 24:155–159, 2002.

[152] S. Gara, S. M'hamed, and O. Tsoumarev. Temperature measurement and machining damage in slotting of multidirectional CFRP laminate. *Machining Science and Technology*, 22:320–337, 2018.

[153] O. Pecat, R. Rentsch, and E. Brinksmeier. Influence of milling process parameters on the surface integrity of CFRP. *Procedia CIRP*, 1:466–470, 2012. Fifth CIRP Conference on High Performance Cutting 2012, Zurich, Switzerland.

[154] S. Ghafarizadeh, J.F. Chatelain, and G. Lebrun. Finite element analysis of surface milling of carbon fiber-reinforced composites. *The International Journal of Advanced Manufacturing Technology*, 87:399–409, 2016.

[155] A. Caggiano. Machining of fibre reinforced plastic composite materials. *Materials*, 11:442, 2018.

[156] A.I. Azmi, R.J.T. Lin, and D. Bhattacharyya. Machinability study of glass fibre-reinforced polymer composites during end milling. *The International Journal of Advanced Manufacturing Technology*, 64:247–261, 2013.

[157] N.A. Fleck, D. Liu, and J.Y. Shu. Microbuckle initiation from a hole and from the free edge of a fibre composite. *International Journal of Solids and Structures*, 37:2757–2775, 2000.

[158] C.R. Schultheisz and A.M. Waas. Compressive failure of composites, Part I: Testing and micromechanical theories. *Progress in Aerospace Sciences*, 32:1–42, 1996.